A L I C E

Addendum

to the

Technical Design Report

of the

Dimuon Forward Spectrometer

ALICE Collaboration

Alessandria, Italy, Facoltà di Scienze dell'Università:
G. Dellacasa, P. Ottria, L. Ramello, E. Scalas and M. Sitta.

Aligarh, India, Physics Department, Aligarh Muslim University:
N. Ahmad, S. Ahmad, T. Ahmad, W. Bari, M. Irfan and M. Zafar.

Athens, Greece, Nuclear and Particle Physics Division, University of Athens:
A.L.S. Angelis[1], G. Mavromanolakis and A.D. Panagiotou.

Athens, Greece, Institute of Nuclear Physics, NRC Demokritos:
K. Kalfas.

Bari, Italy, Dipartimento di Fisica dell'Università and Sezione INFN:
R. Caliandro, D. Cozza, G. De Cataldo, D. Di Bari, D. Elia, R.A. Fini, B. Ghidini, V. Lenti, V. Manzari,
E. Nappi, F. Navach and F. Posa.

Bari, Italy, Politecnico and Sezione INFN:
F. Corsi, D. De Venuto, R. Dinapoli, A. Grimaldi, G. Lisco, C. Marzocca and E. Monno.

Beijing, China, China Institute of Atomic Energy:
X. Li, S. Lu, Z. Lu, B. Sa, J. Yuan, J. Zhou, S. Zhou and X. Zhu.

Bergen, Norway, Faculty of Engineering, Bergen College:
H. Helstrup and J.A. Lien.

Bergen, Norway, Department of Physics, University of Bergen:
K. Fanebust, A. Klovning, O.A. Mæland, O.H. Odland, D. Röhrich, R. Rongved, K. Ullaland and
A.S. Vestbø.

Bhubaneswar, India, Institute of Physics:
S.N. Behera, A.K. Dubey, D.P. Mahapatra, B. Mohanty and S.C. Phatak.

Birmingham, United Kingdom, School of Physics and Space Research, University of Birmingham:
I.J. Bloodworth, D. Evans, G.T. Jones, P. Jovanović, J.B. Kinson, P.I. Norman, O. Villalobos Baillie and
M.F. Votruba.

Bologna, Italy, University/INFN:
F. Anselmo, P. Antonioli, G. Bari, M. Basile, L. Bellagamba, D. Boscherini, A. Bruni, G. Bruni,
G. Cara Romeo, E. Cerron-Zeballos, F. Cindolo, N. Coppola, M. Corradi, S. De Pasquale, D. Falchieri,
A. Gabrielli, E. Gandolfi, P. Giusti, D. Hatzifotiadou, N.Y. Kim, G. Laurenti, M.L. Luvisetto,
A. Margotti, M. Masetti, R. Nania, F. Palmonari, A. Pesci, F. Pierella, A. Polini, G. Sartorelli,
A. Semak, G. Valenti, M.C.S. Williams and A. Zichichi.

Bratislava, Slovakia, Faculty of Mathematics and Physics, Comenius University:
J. Bracinìk, V. Černý, J. Ftáčnik, V. Hlinka, R. Janik, R. Lietava, M. Pikna, J. Pišút, N. Pišútová,
P. Rosinsky, B. Sitar, P. Strmeň, I. Szarka and M. Zagiba.

Bucharest, Romania, National Institute for Physics and Nuclear Engineering:
A. Andronic, V. Catanescu, M. Ciobanu, M. Duma, C.I. Legrand, D. Moisa, M. Petrovici, V. Simion and G. Stoicea.

Budapest, Hungary, KFKI Research Institute for Particle and Nuclear Physics, Hungarian Academy of Sciences:
E. Denes, B. Eged, Z. Fodor, T. Kiss, G. Palla, G. Rubin[1], C. Soos, J. Sulyan, J. Sziklai, B.N. Vissy and J. Zimanyi.

Cagliari, Italy, Dipartimento di Fisica dell'Università and Sezione INFN:
C. Cicalo, A. De Falco, M.P. Macciotta-Serpi, A. Masoni, A. Pataki, G. Puddu, P. Randaccio, S. Serci, E. Siddi and G. Usai.

Calcutta, India, Saha Institute of Nuclear Physics:
P. Bhattacharya, S. Bose, Sukalyan Chattopadhyay, N. Majumdar, S. Mukhopadhyay, A. Sanyal, S. Sarkar, P. Sen, S.K. Sen, B.C. Sinha and T. Sinha.

Calcutta, India, Variable Energy Cyclotron Centre:
Subhasis Chattopadhyay, M.R. Dutta Majumdar, M.S. Ganti, T.K. Nayak, S. Pal, R.N. Singaraju, Bikash Sinha, M.D. Trivedi and Y.P. Viyogi.

Catania, Italy, Dipartimento di Fisica dell'Università and Sezione INFN:
A. Badalà, R. Barbera, M. Gulino, S. Ingrassia, A. Insolia, L. Lo Nigro, D. Lo Presti, G. Lo Re, A. Palmeri, G.S. Pappalardo, L. Pappalardo, C. Petta, N. Randazzo, S. Reito, F. Riggi, G.V. Russo and S. Vanadia.

CERN, Switzerland, European Laboratory for Particle Physics:
Y. Andres, J. Bächler, J.A. Belikov[2], J.-C.Berset, R. Brun, P. Buddin, M. Burns, M. Campbell, W. Carena, F. Carminati, L. Casagrande, S. Chapeland, P. Chochula[3], V. Colin de Verdière, J. Cruz de Sousa Barbosa, M. Davenport, J. de Groot, A. Di Mauro, R. Divià, C. Eisenberg, C. Engster, R. Esteve Bosch, F. Formenti, D. Fraissard, I. Gonzalez Caballero, B. Goret, T. Grassi, C. Gregory, M. Hoch, P. Ijzermans, A. Jimenez de Parga, P.G. Innocenti, W. Klempt, A. Kluge, X. Lagrue, G. Lecoeur, J.C. Legrand, L. Leistam, B. Lenkeit, P. Lenoir, Y. Lesenechal, C. Lourenço, P. Martinengo, M. Mast, F. Meddi, T. Meyer, A. Morsch, M. Mota, L. Musa, F. Piuz, J. Raynaud, J.P. Revol, A. Rivetti, K. Šafařík, J.-C. Santiard, K. Schossmaier, J. Schukraft, E. Schyns, W. Snoeys, P. Sonderegger, G. Stefanini, D. Swoboda, P. Szymanski, J. Van Beelen, P. Vande Vyvre, A. Vascotto, S. Wenig, P. Wertelaers, T. Williams and J. Zalipska.

Chandigarh, India, Physics Department, Panjab University:
M.M. Aggarwal, A.K. Bhatia, V.S. Bhatia and G. Sood.

Clermont-Ferrand, France, Laboratoire de Physique Corpusculaire (LPC), IN2P3-CNRS and Université Blaise Pascal:
IN2P3: A. Baldit, V. Barret, N. Bastid, G. Blanchard, J. Castor, T. Chambon, P. Crochet, F. Daudon, A. Devaux, P. Dupieux, B. Espagnon, P. Force, B. Forestier, A. Genoux-Lubain, C. Insa, F. Jouve, L. Lamoine, J. Lecoq, F. Manso, L. Royer, P. Saturnini, G. Savinel and P. Rosnet.

Coimbra, Portugal, Departamento de Física, Faculdade de Ciências e Tecnologia:
R. Ferreira Marques, P. Fonte, J. Pinhao and A. Policarpo.

Columbus, U.S.A., Department of Physics, Ohio State University:
H.L. Caines, H.M. Dyke, T.J. Humanic, M. Lisa, B.S. Nilsen, G. Paić[1] and E. Sugarbaker.

Copenhagen, Denmark, Niels Bohr Institute:
I. Bearden, H. Bøggild, P. Christiansen, J.J. Gaardhøje, O. Hansen, A. Holm, B.S. Nielsen and
D. Ouerdane.

Cracow, Poland, Henryk Niewodniczanski Institute of Nuclear Physics, High Energy Physics
Department:
J. Bartke, E. Gładysz-Dziaduś, E. Górnicki, M. Kowalski, A. Rybicki, P. Stefański and Z. Wlodarczyk[5].

Darmstadt, Germany, Gesellschaft für Schwerionenforschung (GSI):
R. Averbeck, E. Badura, C. Blume, P. Braun-Munzinger, H.W. Daues, A. Deusser, A. Devismes,
C. Finck, P. Foka, U. Frankenfeld, C. Garabatos, G. Hering, M. Ivanov[4], J. Lühning, P. Malzacher,
C. Markert, A. Mischke, D. Miśkowiec, W.F.J. Müller, F. Rademakers, H. Sako, A. Sandoval, H. Sann,
H.R. Schmidt, S. Sedykh, H. Stelzer, R. Veenhof and D. Vranic.

Darmstadt, Germany, Institut für Kernphysik, Technische Universität:
A. Förster, H. Oeschler and F. Uhlig.

Frankfurt, Germany, Institut für Kernphysik, Johann Wolfgang Goethe-Universität:
C. Adler, W. Amend, J. Berger, J. Berschin, A. Billmeier, P. Buncic, D. Flierl, M. Gaździcki, J. Hehner,
S. Lange, R. Renfordt, H. Rheinfels-Immans, C. Roland, G. Roland, R. Stock, H. Ströbele and
C. Struck.

Gatchina, Russia, St. Petersburg Nuclear Physics Institute:
B. Komkov, V. Kozlov, D. Markushin, N. Miftakhov, V. Nikouline, G. Rybakov, V. Samsonov,
O. Tarasenkova, S. Volkov and A. Vorobiev.

Heidelberg, Germany, Kirchhoff Institute for Physics:
R. Achenbach, O. Braun, M. Keller, F.O. Lesser, V. Lindenstruth, R. Schneider, M. Schulz, T. Steinbeck
and L. Voerg.

Heidelberg, Germany, Physikalisches Institut, Ruprecht-Karls Universität:
H. Appelshäuser, S. Damjanovic, T. Dietel, S.I. Esumi, K. Filimonov, P. Glässel, N. Herrmann,
A. Marin, V. Petráček, J. Rak, A. Reischl, M.J. Richter, E. Schäfer, W. Schmitz, W. Seipp, J. Slivova,
H.K. Soltveit, H.J. Specht, J. Stachel, H. Tilsner, J.P. Wessels, T. Wienold, B. Windelband and
S. Yurevich.

Ioannina, Greece, University of Ioannina, Department of Physics:
X. Aslanoglou and N.G. Nicolis.

Jaipur, India, Physics Department, University of Rajasthan:
A. Bharti, S.K. Gupta, R. Raniwala and S. Raniwala.

Jammu, India, Physics Department, Jammu University:
S.K. Badyal, A. Bhasin, A. Gupta, V.K. Gupta, S. Mahajan, L.K. Mangotra, B.V.K.S. Potukuchi,
N.K. Rao and S.S. Sambyal.

JINR, Russia, Joint Institute for Nuclear Research:
P.G. Akichine, V.A. Arefiev, V.I. Astakhov, A.A. Baldine, A.M. Baldine, V.D. Bartenev, B.V. Batiounia,
I.V. Boguslavsky, Z.V. Borissovskaia, P. Bylinkine, A.V. Chabounov, G.S. Chabratova, I.A. Chichov,
V. Danilov, V.I. Datskov, V.K. Dodokhov, L.G. Efimov, A.G. Fedounov, O.A. Golubitsky,
B.N. Guouskov, O.I. Iouldachev, V.G. Kadychevsky, I.E. Karpunina, E.K. Koshurnikov,
A.D. Kovalenko, A. Lioubimtsev, V.L. Lioubochits, V.I. Lobanov, G.I. Lykasov, E.A. Matiouchevski,
K.V. Mikhailov, I. Minaev, P.V. Nomokonov, I.V. Pouzynin, I. Roufanov, I.A. Shelaev, A.V. Sidorov,
M.K. Suleimanov, G.P. Tsvineva and A.S. Vodopianov.

V. Kuznetsov[6] and V. Shestakov[6].

Ts. Baatar[7], B. Khurelbaatar[7] and R. Togoo[7].

K.G. Akhobadze[8], A.K. Djavrishvili[8], T. Grigalashvili[8], E.S. Ioramashvili[8], A.V. Kharadze[8], L. Khizanishvili[8], T.V. Khuskivadze[8], L.V. Shalamberidze[8] and N. Shubitidze[8].

N. Grigalashvili[9], M. Nioradze[9], M. Tabidze[9] and Y. Tevzadze[9].

D. Felea[10], A. Gheata[10], M. Gheata[10], M. Haiduc[10], D. Hasegan[10], R. Marginean[10], R.I. Nanciu[10] and S.I. Zgura[10].

Jyväskylä, Finland, Department of Physics, University of Jyväskylä and Helsinki Institute of Physics:
J. Aysto, M. Bondila, M. Komogorov, V. Lyapin, V. Ruuskanen and W. Trzaska.

Kangnung, South Korea, Kangnung National University:
H. Chae, C. Choi, Y. Jung, K.S. Kang, D.W. Kim, D. Kim, J. Kim, K. Lee and S. Lee.

Kharkov, Ukraine, National Scientific Centre 'Kharkov Institute of Physics and Technology':
G.L. Bochek, V.F. Boldyshev, A.N. Dovbnya, V.I. Kulibaba, N.I. Maslov, S.V. Naumov, S.M. Potin, I.M. Prokhorets and A.F. Starodubtsev.

Kharkov, Ukraine, Scientific and Technological Research Institute of Instrument Engineering:
V.N. Borshchov, S.K. Kiprich, O.M. Listratenko, G. Protsay, A.N. Reznik, A.N. Ryabukhin and V.E. Starkov.

Kiev, Ukraine, Department of High Energy Density Physics, Bogolyubov Institute for Theoretical Physics, National Academy of Sciences of Ukraine:
T. Hryn'ova, D.E. Kharzeev, E.S. Martynov, O.P. Pavlenko and G. Zinovjev.

Košice, Slovakia, Institute of Experimental Physics, Slovak Academy of Sciences and Faculty of Science P.J. Šafárik University:
J. Bán, J. Fedorišin, M. Hnatič, A. Jusko, I. Králik, A. Kravčáková, F. Kriváň, M. Krivda, M. Lupták, G. Martinská, B. Pastirčák[1], L. Šándor, J. Urbán, S. Vokál and J. Vrláková.

Lausanne, Switzerland, Integrated System Laboratory (ISL), Ecole Polytechnique Fédérale de Lausanne (EPFL):
A. Aizza, F.A. Cherigui, M. Mattavelli and D. Mlynek.

Legnaro, Italy, Laboratori Nazionali di Legnaro:
A. Bologna, M. Lombardi, R.A. Ricci and L. Vannucci.

Lisbon, Portugal, Departamento de Física, Instituto Superior Técnico:
P. Branco, R. Carvalho, J. Seixas and R. Vilela Mendes.

Lund, Sweden, Division of Cosmic and Subatomic Physics, University of Lund:
L. Carlen, S.I.A. Garpman, H.-A. Gustafsson, P. Nilsson, A. Oskarsson, L. Osterman, I. Otterlund, D. Silvermyr and E.A. Stenlund.

Lyon, France, Institut de Physique Nucléaire de Lyon (IPNL), IN2P3-CNRS and Université Claude Bernard Lyon-I:
M.Y. Chartoire, B. Cheynis, L. Ducroux, D. Essertaize, E. Gangler, M. Goyot, J.Y. Grossiord, R. Guernane, A. Guichard, G. Jacquet, M. Miguet, S. Tissot and S. Vanzetto.

Marburg, Germany, Fachbereich Physik, Philipps Universität:
V. Friese, C. Höhne and F. Pühlhofer.

Mexico City, Mexico, Centro de Investigación y de Estudios Avanzados:
A. Ayala, G. Contreras, J.C. D'Olivo, G. Herrera Corral A. Menchaca, L.M. Montaño and L. Nellen.

Moscow, Russia, Institute for Nuclear Research, Academy of Science:
K.A. Chileev, M.B. Goloubeva, F.F. Gouber, T.L. Karavitcheva, A.B. Kourepin, A.I. Maevskaia,
V.I. Razine, A.I. Rechetine and N.S. Topilskaia.

Moscow, Russia, Institute for Theoretical and Experimental Physics:
A.N. Akindinov, V. Golovine, A.B. Kaidalov, M.M. Kats, I.T. Kiselev, S.M. Kisselev, E. Lioublev,
M. Martemianov, A.N. Martemiyanov, P.A. Polozov, V.S. Serov, A.V. Smirnitski, M.M. Tchoumakov,
I.A. Vetlitski, K.G. Volochine, L.S. Vorobiev and B.V. Zagreev.

Moscow, Russia, Russian Research Center 'Kurchatov Institute':
V. Antonenko, S. Beliaev, I. Doubovik, S. Fokine, M. Ippolitov, K. Karadjev, A.L. Lebedev, V. Lebedev,
V.I. Manko, T. Moukhanova, A. Nianine, S. Nikolaev, S. Nikouline, O. Patarakine, D. Peressounko,
I. Sibiriak, A. Vasiliev, A. Vinogradov and M. Volkov.

Moscow, Russia, Moscow Engineering Physics Institute:
V.A. Grigoriev, V.A. Kapline and V.A. Loguinov.

Münster, Germany, Institut für Kernphysik, Westfälische Wilhelms Universität:
D. Bucher, R. Glasow, N. Heine, T. Peitzmann, K. Reygers, R. Santo, H. Schlagheck, W. Verhoeven,
M. Wahn and A. Walte.

Nantes, France, Laboratoire de Physique Subatomique et des Technologies Associées (SUBATECH),
Ecole des Mines de Nantes, IN2P3-CNRS and Université de Nantes:
L. Aphecetche, A. Boucham, S. Bouvier, J. Castillo, L. Conin, J.P. Cussonneau, H. Delagrange,
D. D'Enterria, M. Dialinas, C. Drancourt, B. Erazmus, L. Gaudichet, G. Guilloux, H.H. Gutbrod,
P. Lautridou, F. Lefèvre, M. Le Guay, X. Li, L. Luquin, L. Martin, G. Martinez, M.J. Mora, G. Puil,
O. Ravel, C.S. Roy, D. Roy, Y. Schutz and A. Tournaire.

NIKHEF, The Netherlands, National Institute for Nuclear and High Energy Physics:
M. Botje[11], A. Buijs[12], J.J.F. Buskop[11], A.P. De Haas[12], P.K.A. De Witt Huberts[11,12],
R. Kamermans[11,12], P.G. Kuijer[11,12], D. Muigg[12], G. Nooren[11], C.J. Oskamp[12], A. Van Den Brink[12]
and N. Van Eijndhoven[12].

Novosibirsk, Russia, Budker Institute for Nuclear Physics:
A.R. Frolov and I.N. Pestov.

Oak Ridge, U.S.A., Instrumentation and Controls Division, Oak Ridge National Laboratory:
T. Awes, C.L. Britton, W.L. Bryan and A.L. Wintenberg.

Orsay, France, Institut de Physique Nucléaire (IPNO), IN2P3-CNRS and Université de Paris-Sud:
L. Bimbot, P.F. Courtat, R. Douet, P. Edelbruck, D. Jouan, Y. Le Bornec, M. Mac Cormick, J. Peyré,
J. Pouthas and N. Willis.

Oslo, Norway, Department of Physics, University of Oslo:
A.K. Holme, G. Løvhøiden, B. Skaali, T.S. Tveter and D. Wormald.

Padua, Italy, Dipartimento di Fisica dell'Università and Sezione INFN:
F. Antinori[1], N. Carrer, M. Morando, A. Pepato, E. Quercigh, F. Scarlassara, G. Segato, F. Soramel and R. Turrisi.

Pohang, South Korea, Pohang Accelerator Laboratory:
J. Choi, M.G. Kim, T.Y. Lee and E.S. Park.

Prague, Czech Republic, Institute of Physics, Academy of Science:
A. Beitlerova, J. Mareš, E. Mihoková, M. Nikl, K. Píška, K. Polák and P. Závada.

Protvino, Russia, Institute for High Energy Physics:
V. Berejnoi, A.M. Blik, M. Bogolyubsky, G. Britvitch, S. Erine, G.V. Khaoustov, I.V. Kharlov, V. Lichine, M. Lobanov, N. Minaev, S.A. Sadovski, V.D. Samoilenko, P.A. Semenov, V.I. Suzdalev and V. Tikhonov.

Řež u Prahy, Czech Republic, Academy of Sciences of Czech Republic, Nuclear Physics Institute:
D. Adamova, V. Hanzal, J. Hošek, I. Hřivnáčová[1], S. Kouchpil, V. Kouchpil, A. Kugler, M. Šumbera, P. Tlustý, V. Wagner and D. Zákoucký.

Rome, Italy, Dipartimento di Fisica, Università di Roma 'La Sapienza' and Sezione INFN:
S. Di Liberto, M.A. Mazzoni, F. Meddi[1], D. Prosperi and G. Rosa.

Saclay, France, Centre d'Etudes Nucléaires, DAPNIA:
P. Ageron, A. Baldisseri, J.C. Barrière, H. Borel, D. Cacaut, I. Chevrot, P. De Girolamo, J. Gosset, L. Gosset, P. Hardi, D. Jourde, J.C. Lugol, S. Salasca and F.M. Staley.

Salerno, Italy, Dipartimento di Scienze Fisiche 'E.R.Caianiello' dell'Universitá and INFN:
L. Cifarelli, G. Grella, M. Guida, J. Quartieri, G. Romano, A. Seganti, D. Vicinanza and T. Virgili.

Sarov, Russia, Russian Federal Nuclear Center (VNIIEF):
V. Basmanov, D. Budnikov, V. Ianowski, R. Ilkaev, L. Ilkaeva, A. Ivanov, A. Khlebnikov, E. Kolokolnikov, S. Nazarenko, V. Punin, S. Poutevskoi, I. Selin, I. Vinogradov, S. Zhelezov and A. Zhitnik.

Shanghai, China, Shanghai Institute of Ceramics (SICCAS):
Q. Deng, P. Li, J. Liao and D. Yan.

St. Petersburg, Russia, Institute for Physics of St. Petersburg State University, Mendeleev Institute for Metrology and Meson Scientific Association:
L.Y. Abramova, V.S. Alexandrov, P. Bolokhov, A.A. Bolonine, M.A. Braun, V.M. Dobulevitch, G.A. Feofilov, S. Guerassimov, S.N. Igolkine, A.A. Kolojvari, V. Kondratiev, I.A. Novikov, S.V. Potapov, O.I. Stolyarov, A.M. Switchev, T.A. Toulina, F.A. Tsimbal, F.F. Valiev, V.V. Vetchernine and L.I. Vinogradov.

Strasbourg, France, Institut de Recherches Subatomiques (IReS), IN2P3-CNRS and Université Louis Pasteur:
L. Arnold, J. Baudot, D. Bonnet, J.P. Coffin, M. Germain, C. Gojak, M. Guedon, B. Hippolyte, C. Kuhn, J. Lutz, C. Suire and A. Tarchini.

Trieste, Italy, Dipartimento di Fisica dell'Università and Sezione INFN:
V. Bonvicini, L. Bosisio, P. Camerini, E. Fragiacomo, N. Grion, G. Margagliotti, C. Piemonte, A. Rachevski, R. Rui and A. Vacchi.

Turin, Italy, Dipartimenti di Fisica dell'Università and INFN:
G. Alberici, B. Alessandro, R. Arnaldi, P. Barberis, S. Beolé, E. Botta, P.G. Cerello, E. Chiavassa,
P. Cortese, E. Crescio, F. Daudo, N. De Marco, A. Ferretti, L. Gaido, M. Gallio, G. Giraudo,
P. Giubellino[1], P.G. Innocenti, D. Margherita, A. Marzari-Chiesa, M. Masera, G. Mazza, P. Mereu,
B. Minetti, M. Monteno, O. Morra, A. Musso, D. Nouais, C. Oppedisano, A. Piccotti, G. Piragino,
L. Riccati, E. Scomparin, F. Tosello, E. Vercellin, A. Werbrouck and R. Wheadon.

Warsaw, Poland, Soltan Institute for Nuclear Studies:
D. Czerwinski, A. Deloff, K. Karpio, S. Kozak, M. Kozlowski, H. Malinowski, K. Redlich,
T. Siemiarczuk, G. Stefanek, L. Tykarski and G. Wilk.

Warsaw, Poland, University of Technology, Institute of Physics:
J. Grabski, M. Janik, A. Kisiel, P. Leszczynski, T.J. Pawlak, W.S. Peryt, J. Pluta, M.Przewlocki
P. Skowronski and P. Szarwas

Wuhan, China, Institute of Particle Physics, Huazhong Normal University:
X. Cai, S.Q. Feng, Y. Hu, W. Li, F. Liu, F.M. Liu, H. Liu, L.S. Liu, Y. Liu, W.Y. Qian, X.R. Wang,
S.Q. Wu, T. Wu, C.C. Xu, C.B. Yang, Z.B. Yin, D.C. Zhou and D.M. Zhou.

Yerevan, Armenia, Yerevan Physics Institute:
M. Atayan, V. Danielyan, A. Grigorian, S. Grigoryan, H. Gulkanyan, V. Kakoyan, Yu. Margaryan,
L. Parlakyan, G. Sargsyan, R. Shahoyan and H. Vardanyan.

Zagreb, Croatia, Ruder Bošković Institute:
T. Anticic, K. Kadija and T. Susa.

[1] Also at CERN, Geneva, Switzerland.
[2] On leave from JINR, Dubna, Russia.
[3] On leave from Comenius University, Bratislava, Slovakia.
[4] Institut Universitaire de Technologie de Monluçon, Allier, France.
[5] Institute of Physics, Pedagogical University, Kielce, Poland.
[6] Research Centre for Applied Nuclear Physics (RCANP), Dubna, Russia.
[7] Institute of Physics and Technology, Mongolian Academy of Sciences, Ulaanbaatar, Mongolia.
[8] Institute of Physics, Georgian Academy of Sciences, Tbilisi, Georgia.
[9] High Energy Physics Institute, Tbilisi State University, Tbilisi, Georgia.
[10] Institute of Space Sciences, Bucharest, Romania.
[11] Foundation of Fundamental Research of Matter in The Netherlands.
[12] Utrecht University, Utrecht, The Netherlands.
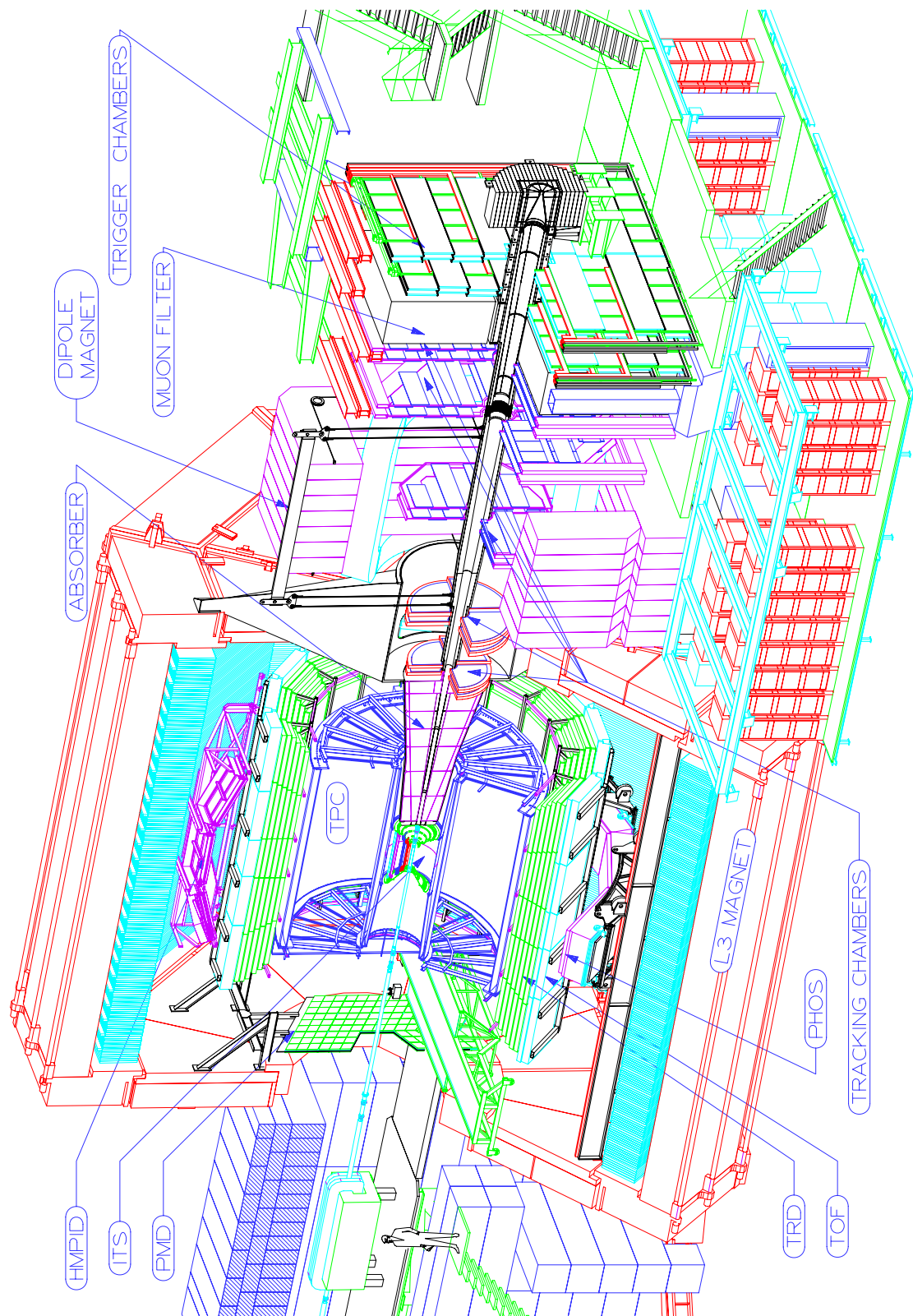[13] University of Wroclaw, Poland.

viii

Acknowledgements

Contents

Figure 1: General layout of the Dimuon spectrometer.

1   Introduction

The dimuon spectrometer, as presented in the ALICE TDR n°5 in 1999 ([1]), has to respond to the challenge of detecting a small number of muon pairs with high efficiency and high resolution in a forward geometry on top of a large event related background. The occupation rate in the tracking chambers depends strongly upon the art of shielding the chambers from the hadronic showers in the front absorber and the beam shield. In early 2000, several proposed solutions were not fully satisfactory, e.g. the absorber, the beam shield and the chamber design. Last but not least, the then published efficiency and resolution were not fully in agreement with what was wanted for the Dimuon spectrometer. Since then, discrepancies in the background calculations in two different codes have been solved. This has led to a better understanding of the background in the chambers and the performances of the detectors. In response to that, we optimized the design of the absorber and the beam shield. Based on that, tracking chambers were modified, and prototypes built and tested in beam at CERN in order to validate the changes. Furthermore, easier integration and easier access to the chambers for maintenance, as well as more efficient and cost-effective production, resulted from these changes.

All the details of the vacuum chamber (flanges, bellows, etc) were integrated in the simulations of the front absorber and the beam shield since their effect on the background is non-negligible. A large amount of tungsten was replaced by lead, which decreased dramatically the price of the beam shield without increasing the amount of background. The last plate of lead in the front absorber will be replaced by copper or stainless steel, which, owing to its lower atomic charge, will reduce radiative losses of muons at hight momenta, while at the same time providing the required interaction length.

An optimization of the chambers as a function of the background led to the following design.

- All the chambers are still based on a cathode pad technology but the materials and shapes have been changed.

- The two first stations are now made of light materials and have no aluminium frame in the acceptance. The weight of one quadrant is about 15 kg instead of 64, which is very convenient for integration and manipulation in such a packed space.

- To decrease the occupation rate in Stations 1, the pad size has been reduced, and the gap between the cathode and the anode, together with the corresponding pitch between the wires, has been decreased to 2 mm. This of course increased the number of electronic channels.

- Station 3 is now of the same slat technology as Stations 4 and 5, reducing the amount of R&D.

The slat design has seen a lot of prototype tests. For the inner slats, a circular end shape was chosen in order to improve the coverage of the system. Meanwhile, work on the electronics for the tracking readout was going on. The first MANAS engineering chips were released and tested in India.

The dipole magnet was not redesigned but the responsibilities and the manufacturing were totally reorganized. The yoke will be built in Dubna but the coil will be made in the industry. Owing to a different integration scenario, the magnet and the muon filter now sit on a simple concrete base instead of a movable platform. This lowered the costs substantially.

On the trigger side nothing was changed but a lot of tests and fine tunings were performed especially for the electronics which is now better adapted to the signals of the resistive plate chambers. Nevertheless, a 'V0' detector was added to give a better vertex determination and fewer accidental events during p–p runs. A full status report is given in this document as well as all the relevant results from the laboratory and beam tests.

Since the TDR a lot of progress has been made on the integration. This part is quite challenging because of the very packed space between the inner tracking system and the exit of the dipole magnet, and

of course because of the size of some elements. Installation problems have been solved, as have accesses for Stations 1, 2 and 3 during short shutdowns. With a better knowledge of the dimuon spectrometer the full work schedule updated and the costs of the different elements have been updated. A new set of milestones and costs are then proposed at the end of the addendum.

The present document describes only the differences with respect to the TDR and the present status of the detectors. The TDR is therefore still the reference for all the remaining information.

2 Tracking chambers

2.1 Introduction

Since the writing of the TDR (see Ref. [1]), new features have induced some changes in the tracking set-up of the dimuon arm. In this chapter these features will be presented, together with the modifications they have prompted. These are principally the following.

- For Stations 1 and 2:

  - change of the internal geometry,
  - modification of the mechanical structure.

- Station 3, which was designed with a quadrant structure, is now transformed into a 'slat' architecture.

- The electronics equipment has been upgraded to take account of these changes.

Besides these new aspects, progress made in the different domains will be described: slat conception and validation, cooling, low-voltage supplies, etc.

2.2 Modifications to Stations 1 and 2

2.2.1 Motivations

Following the performance results of the dimuon arm calculated in the TDR and an increase of the particle flux on the first two stations coming from Monte Carlo calculations including all the mechanical details, it has been decided to modify the structures of these two stations with the following aims:

- to reduce the occupation rate,
- to suppress the dead zones due to the aluminium frames,
- to reduce the weight for easier handling.

2.2.2 Internal geometry

In order to achieve these improvements, modifications have been made to the internal geometry by decreasing the pad sizes from 5×7.5 mm^2 down to 4×6 mm^2 for the smallest pads of Station 1. This modification is useful only if the anode–cathode gap is decreased in the same ratio, i.e. from 2.5 mm down to 2 mm. Thanks to these modifications the occupation factor (defined as the ratio between the number of fired pads and the total number of pads in a given area) is reduced by about 36% for the same particle flux and the same chamber gain. Moreover, the pads of the opposite cathodes have been staggered in both x and y directions giving the following advantages.

- There is always on one cathode, a charge configuration which corresponds to three hit pads, even with a lower high voltage (HV).

- In the case of overlapping events it helps to disentangle these two hits.

Table 2.1: Pad size and layout for each cathode plane of Station 1.

Station 1- first cathode plane			
Radius (mm)	Width (mm)	Length (mm)	Channels
175-552	4.0	6.0	35888
552-713	4.0	12.0	13195
713-915	4.0	24.0	10901
Total/chamber			59684
Station 1- second cathode plane			
Radius (mm)	Width (mm)	Length (mm)	Channels
175-552	4.0	6.0	35888
552-713	6.0	8.0	13195
713-915	6.0	16.0	10901
Total/chamber			59684
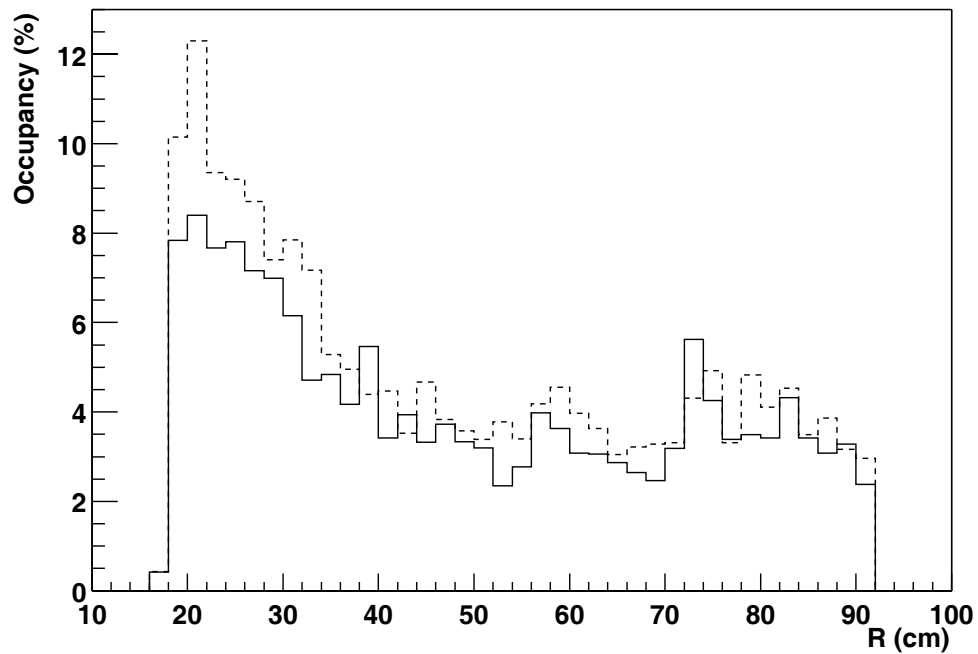
Figure 2.1: Occupancy in per cent as a function of the radius for Station 1. Full line corresponds to Chamber 1 and dashed line to Chamber 2.

Table 2.2: Pad size and layout for each cathode plane of the Station 2.

Station 2 - first cathode plane			
Radius (mm)	Width (mm)	Length (mm)	Channels
235-471	5.0	7.5	13950
471-877	5.0	15.0	22912
877-1225	5.0	30.0	15180
Total/chamber			52042
Station 2 - second cathode plane			
Radius (mm)	Width (mm)	Length (mm)	Channels
235-471	7.5	5.0	13950
471-877	7.5	10.0	22912
877-1225	7.5	20.0	15180
Total/chamber			52042

With these new pad sizes and the spatial layout shown in Table 2.1, the occupancy of Station 1 is shown as a function of the radius in Fig. 2.1.

The pad sizes and the corresponding occupancies for Station 2 are shown in Table 2.2 and in Fig. 2.2.

2.3 Test results

2.3.1 In-beam test results

To test the new internal geometrical configuration of the chamber (pad sizes, staggering and smaller gap), two new cathode planes were built with 256 active pads on each plane and mounted on the prototype referred to as ALICE 1 in the TDR. For reasons of time and amount of work, the anode wire pitch remained unchanged with a 2.5 mm value. The new 0.7 μm GASSIPLEX were still not available, so measurements were performed with a reduced dynamical range compared to the final version.

Extensive studies were performed in June 2000 on the SPS with a 350 GeV/c π^- beam and with an experimental set-up as described in Fig. 2.25 of the TDR. The goal of these tests was to check the influence of these modifications on the chamber efficiency, the plateau width, the spatial resolution and the number of hit pads for each particle.

The electronics noise is quite low, as can be seen in Fig. 2.3 where the mean value corresponds to about 800 e$^-$. No calibration of the electronics for measuring the linearity has been made during these tests.

Because of the high electronic gain of the 1.5 μm GASSIPLEX, the measurements were performed at anode voltages lower than 1500 V where saturation effects remain reasonable. As shown later, around 20% of the events correspond to a charge configuration on one cathode plane with a saturation on one pad and 9% to a configuration with a saturation on at least two pads, when operating at 1500 V. Nevertheless, this value is far below the voltage limitation of 1765 V corresponding to the stability condition for the detector itself.

This saturation effect is illustrated in Fig. 2.4 on a charge distribution measured on the pad collecting the maximum charge at 1500 V. The mean total charge on each cathode plane plotted against the anode HV is shown in Fig. 2.5. The slight nonlinearity for HV > 1480 V corresponds to the saturation effect discussed before.

The charge correlation between the two cathodes is clearly seen in Figs. 2.6 and 2.7 with a standard deviation of 7% and a maximum difference of ±20% respective to the total anode charge. Finally the average number of hit pads is plotted for each plane as a function of the anode HV (Fig. 2.8).
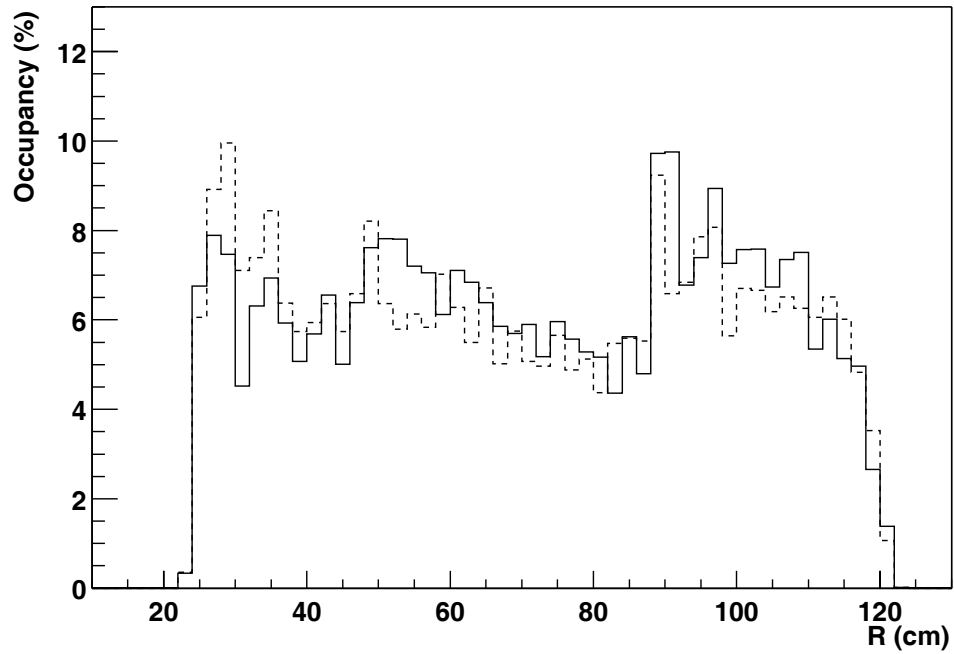
Figure 2.2: Occupancy in per cent as a function of the radius for Station 2. Full line corresponds to Chamber 1 and dashed line to Chamber 2.
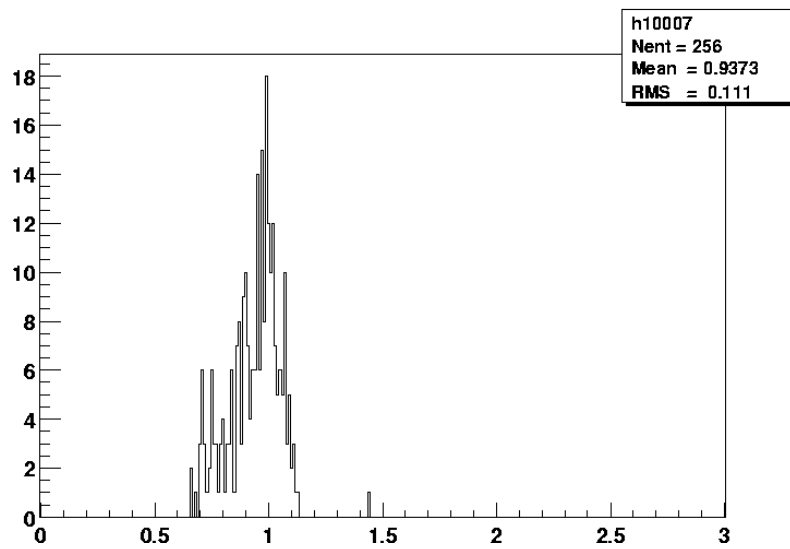
Figure 2.3: Histogram of the noise values in ADC channels.
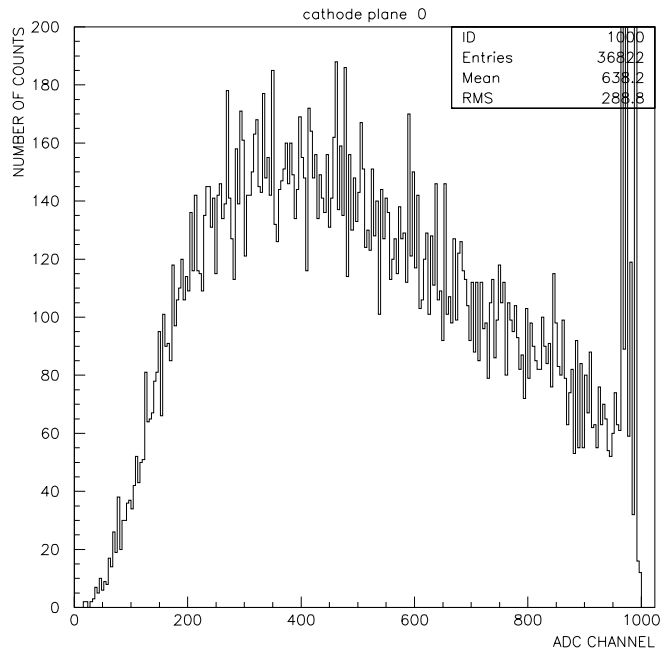
Figure 2.4: Histogram of the maximum charges measured for V = 1500 V.
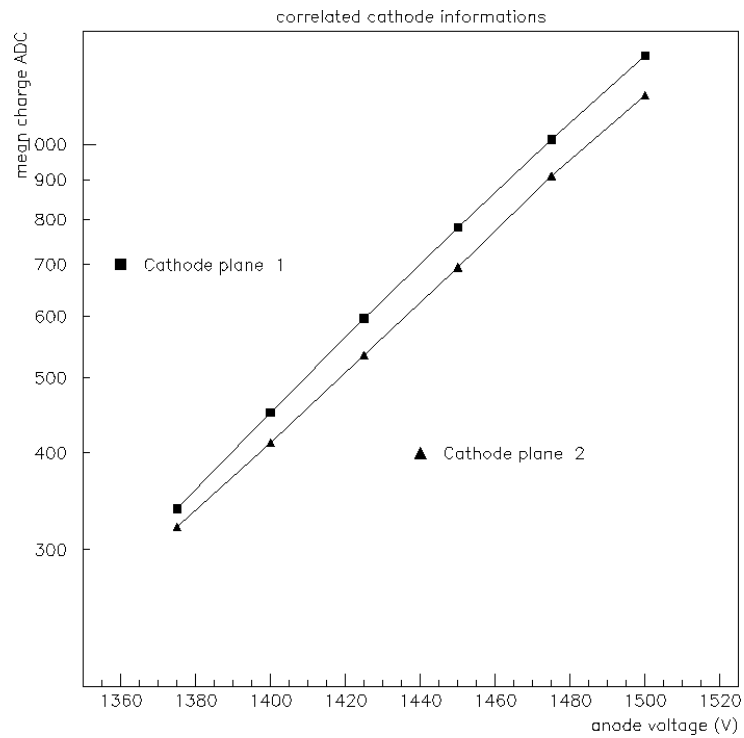
Figure 2.5: Total charge measured on the cathode planes vs. anode high voltage.
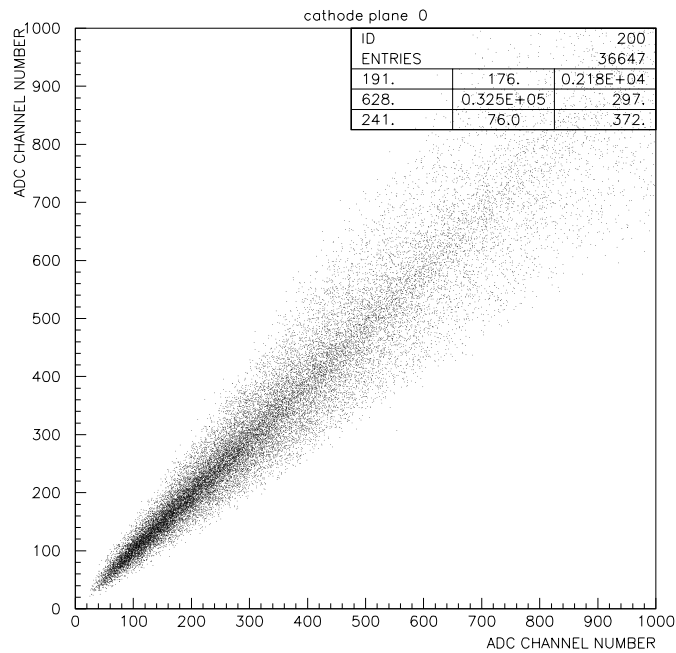
Figure 2.6: Correlation between the charges measured on the two cathode planes for V = 1400 V.
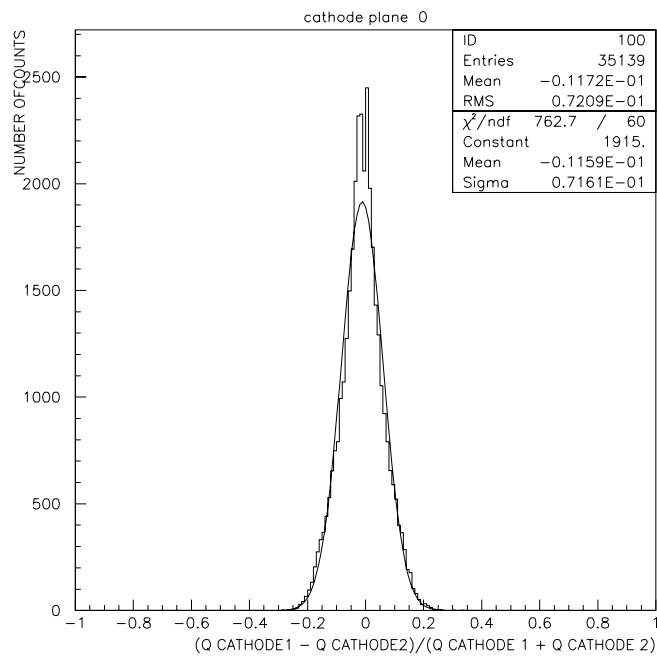
Figure 2.7: Difference between the charges measured on the two cathode planes normalized by the anode charge for V = 1400 V.
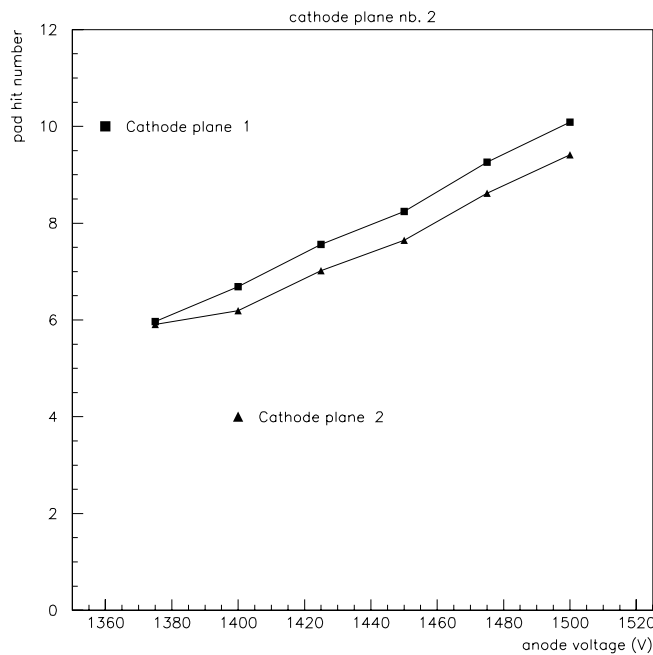
Figure 2.8: For the smallest pads, number of hit pads for each cathode plane as a function of anode high voltage.

At 1375 V, the usual nine hit pads configuration will not be fulfilled for some of the events, nor will the three pads configuration in the high-resolution direction. At the higher edge of the range (1500 V) a large fraction of the events will have a hit pad configuration with a saturated central pad. These different configurations in the high-resolution direction have been studied and the relative importance of each configuration is plotted for each plane in Figs. 2.9 and 2.10 as a function of the HV.

As quoted previously, 20% of saturations are observed at 1500 V. The reconstruction of the position of the hit has been performed on each plane using the usual fit procedure for the three cases:

- two adjacent pads only,

- three adjacent pads (at least) corresponding to the standard configuration,

- one central saturated pad.

  Reconstruction efficiency for each case is plotted in Figs. 2.11 and 2.12 for each plane, together with the corresponding spatial resolution. As foreseen, the efficiency is worst for the third case at low HVs where the charge collected by the adjacent pads (only used in the calculation) is low. The corresponding resolution values have the same trend. Resolution values are better for one plane compared to the second one. This can be explained by a geometrical effect: because of the staggering of the pads (by half a pad width) on the two planes and because of the beam size (one pad width) most of the particles hit the first plane in the central region of a pad and the second one at the edges of two pads. It is well known from simulations that the resolution is better in this last case, and this effect is illustrated with the experimental values in Fig. 2.13.

Then a global efficiency for the two planes has been deduced . The global spatial resolution has been studied. These results are plotted in Figs. 2.14 and 2.15 against the anode voltage. In Fig. 2.14, the reconstructed hits are those of Plane 1; the information from the second plane is used only in case of inefficiency in the first plane. The situation is symmetrical for Fig. 2.15.
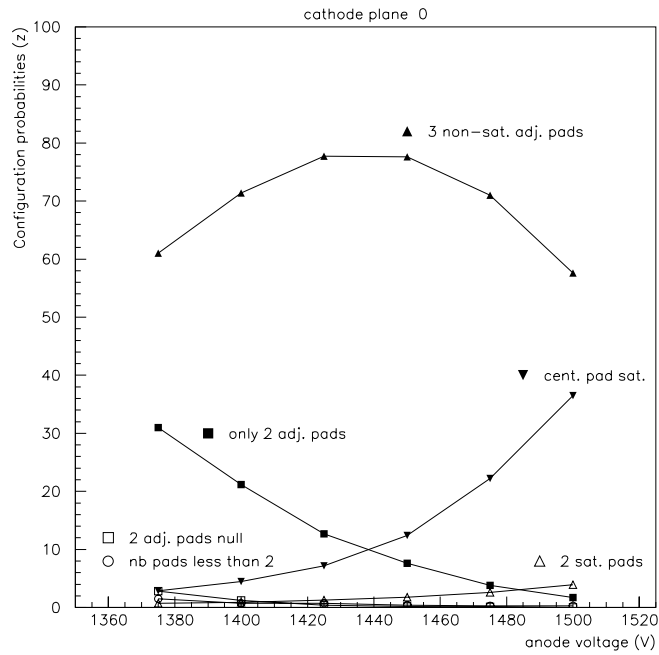
Figure 2.9: Different pad configurations for the first cathode plane.
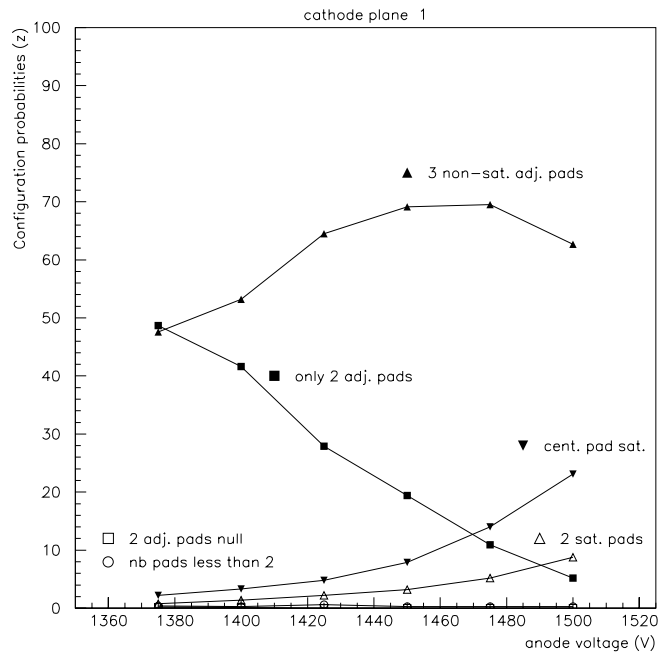
Figure 2.10: Different pad configurations for the second cathode plane.
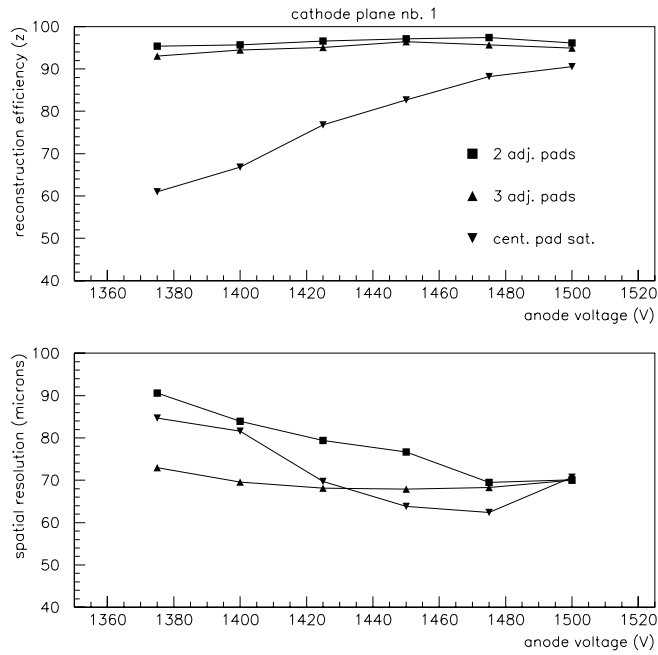
Figure 2.11: Reconstruction efficiencies and spatial resolutions for the different pad configurations in the first cathode plane.
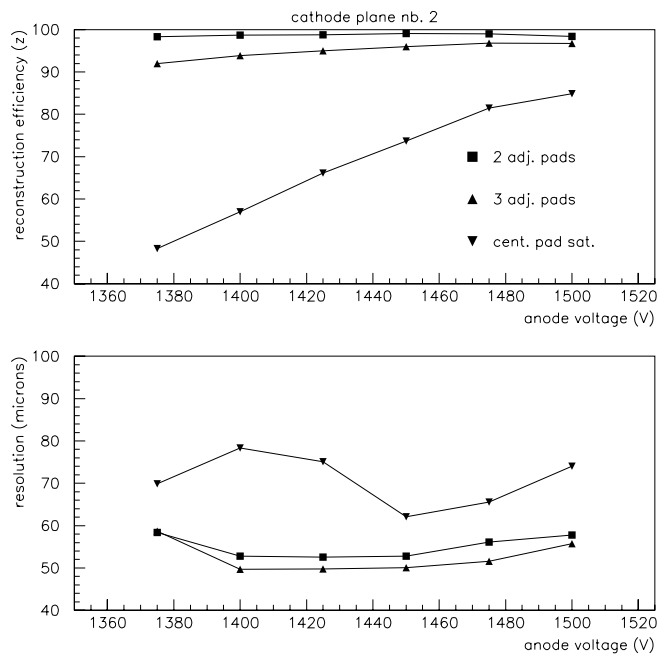
Figure 2.12: Reconstruction efficiencies and spatial resolutions for the different pad configurations in the second cathode plane.
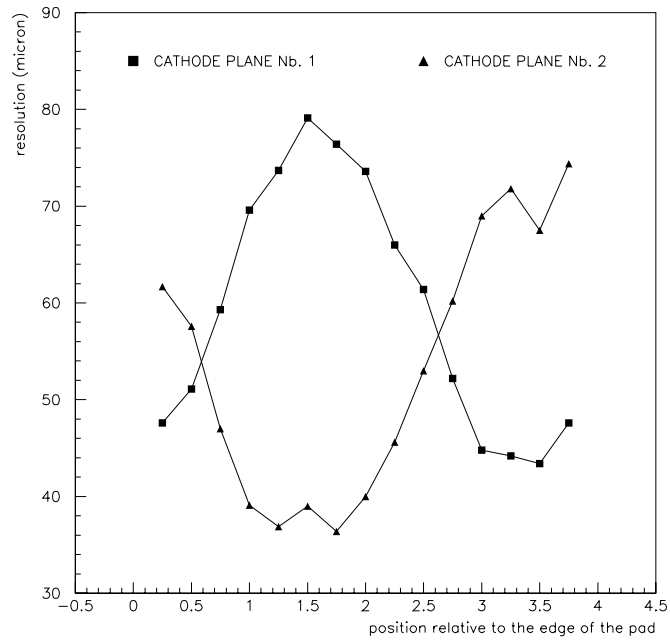
Figure 2.13: Spatial resolution versus the location of the hit on the pad of the first cathode plane, for the standard configuration (at least three adjacent pads).
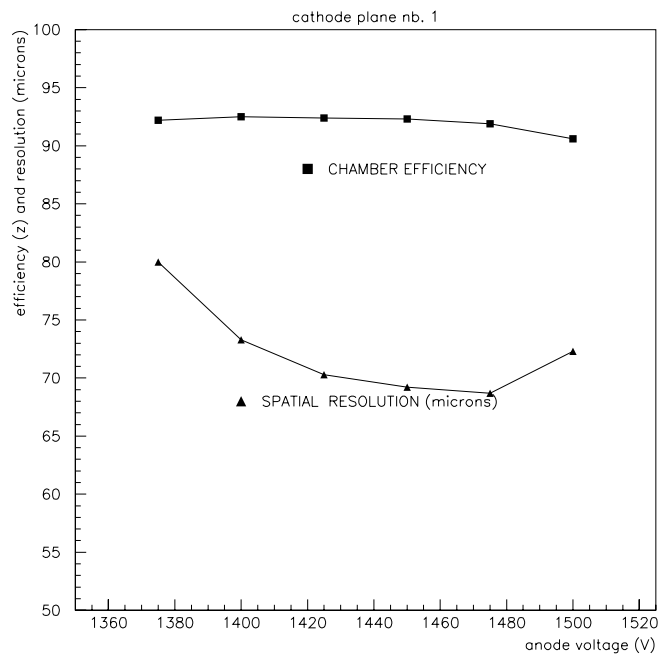
Figure 2.14: Global efficiency and resolution of the two correlated cathode planes, priority being given to the first plane.
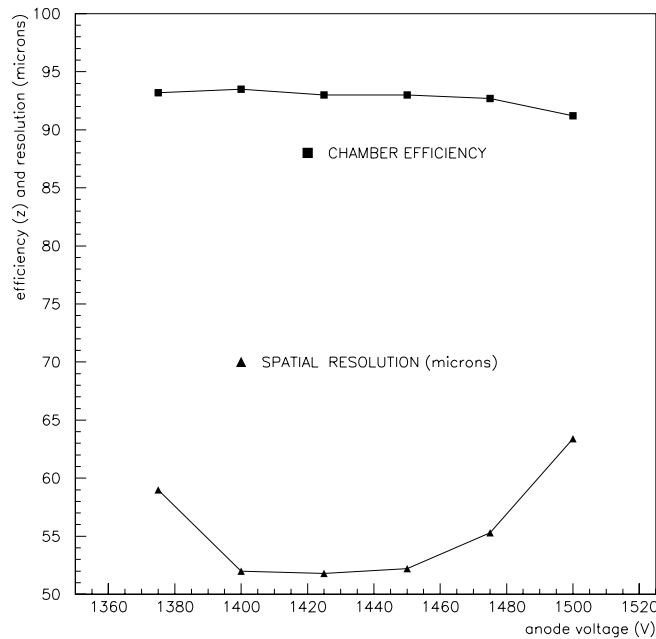
Figure 2.15: Global efficiency and resolution of the 2 correlated cathode planes, priority being given to the second plane.

The decrease of the efficiency versus the HV is mainly due to an increase in the number of rejected events corresponding to two saturated pads configurations.

Finally the corrected COG procedure was used to deduce resolution values. In the standard configuration at least three adjacent pads fired.

In order to summarize, the in-beam tests have shown that, with this new geometrical structure, the nominal performances (resolution better than 100 μm and efficiency better than 90%) can be achieved even with the 'old' GASSIPLEX chips. The use of MANAS will allow a much larger operational plateau.

2.3.2   Mechanical structure of Stations 1 and 2

In order to suppress the dead zones due to the frames, new designs have been adopted in which the sensitive areas of the four quadrants of the same chamber overlap. This new architecture is represented in Fig. 2.16. Figure 2.17 also illustrates the overlapping of the quadrants and the suppression of the dead area.

Figures 2.16 and 2.17 show that the decrease of the pad size and the dead zone suppression have some unfavourable consequences:

- they increase the electronics density at small radius and, consequently, worsen the cooling problem;

- they increase the radiation length in the overlapping region, which is nevertheless negligible for Station 1 located just behind the front absorber.

Removal of the aluminium frames, which has permitted a reduction in the weight of each quadrant (e.g. from 64 kg down to 15 kg for one quadrant of Station 1), has also suppressed the grounding reference which is now replaced by an external aluminium structure. For the main part, the internal mechanical
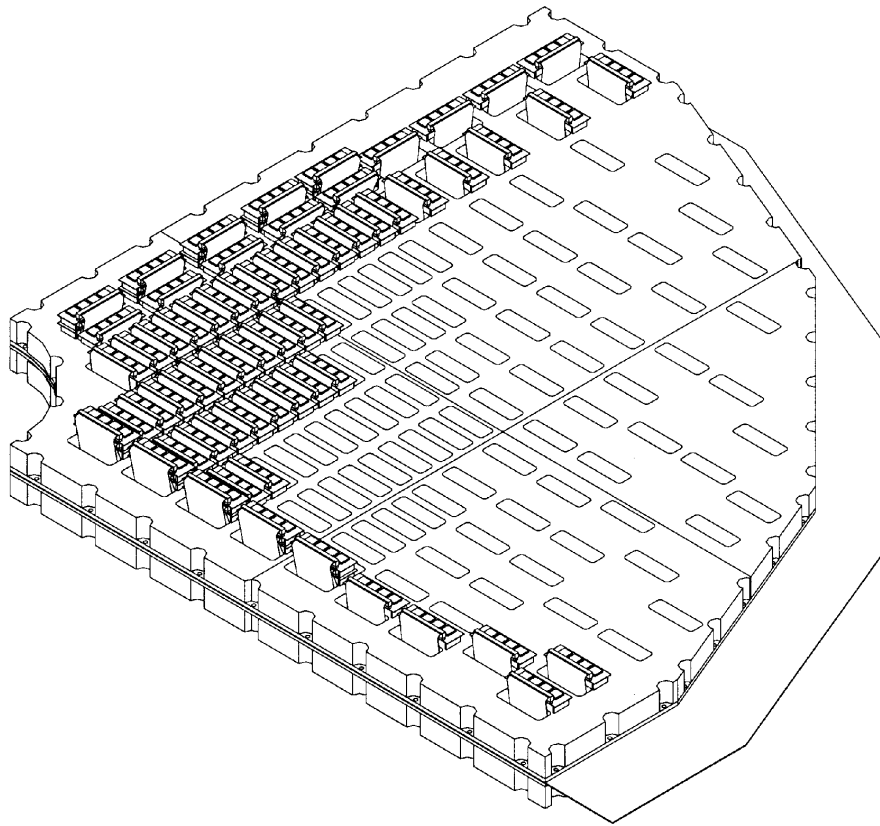
Figure 2.16: Overall view of the frameless chambers.
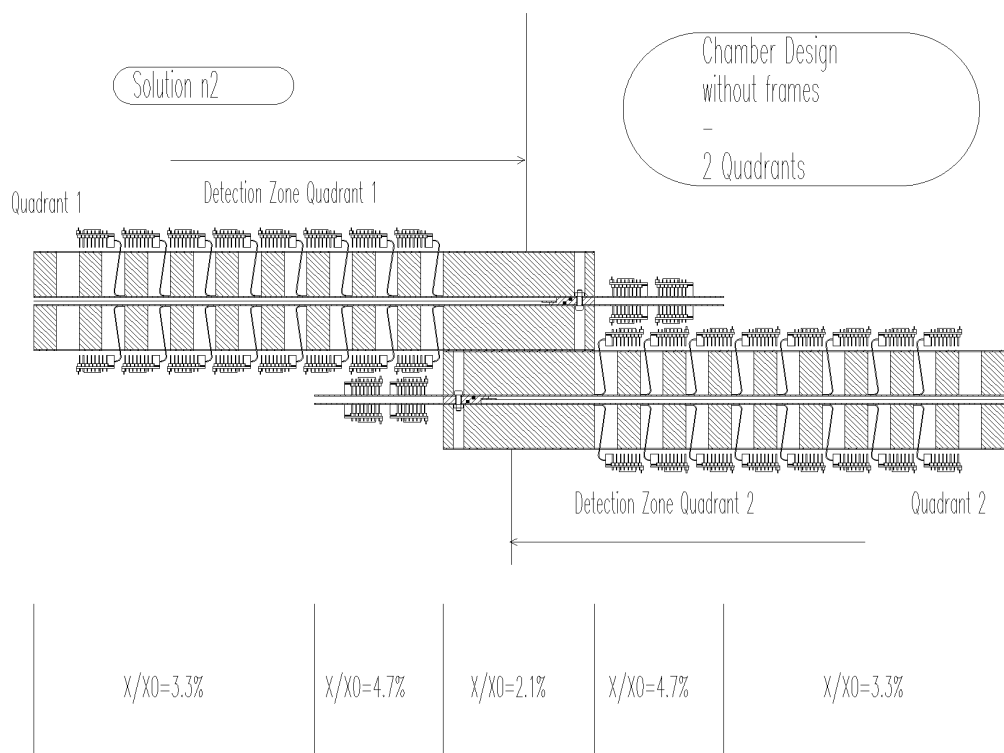
Figure 2.17: Detailed view of the overlapping sensitive area.
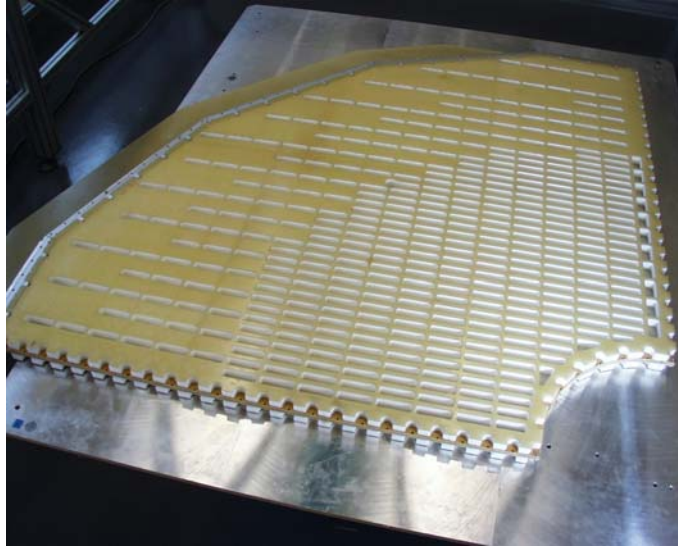
Figure 2.18: View of the mechanical prototype of one quarter of a station chamber.

structures remain the same as before, except for the addition of a small FR4 pin located approximately in the middle of the chambers. The role of this pin is to reduce both the gap variation due to the gas overpressure and the foam layer thickness. Extensive calculations concerning these aspects are described in detail in an internal report [2].

In order to validate the new mechanical architecture of Stations 1 and 2, it has been decided to build, in parallel, two mechanical prototypes in the two laboratories in charge of the construction of the definitive chambers. These prototypes are only mechanical for obvious reasons of cost, manpower and time. The two similar prototypes will ensure that the same processes and technologies are used in both laboratories.

These prototypes were completed at the end of October (see Figs. 2.18 and 2.19) and will be used for deformation measurements which will be compared to extensive calculations.

As already described in the TP, the quadrants will be assembled in pairs on external rigid structures which will hold the monitoring sensors.

With this new mechanical structure, the distance between two similar planes of a station is 130 mm for Station 1 and 150 mm for Station 2, and the overall thickness is 260 mm for Station 1 and 300 mm for Station 2.

2.3.3   Cooling

The challenge for Stations 1 and 2 cooling is to remove 4 kW of heat dissipated by the electronics. A full-size model of a quarter of the cylinder in which Stations 1 and 2 will be enclosed has been built. The four chambers of these two stations have been modelled by FR4 planes on which resistors were soldered with the same spatial density as the final electronics. The temperature measurements were performed with temperature sensors located over the whole surface of the modelled chambers. Figure 2.20 shows one quarter of Station 1 inside the cylinder.

To account for the quarter chamber which will be located below this quadrant, a ramp of resistors has been put in the bottom of the quadrant.

The upper part of the cylinder was equipped with pipes for water circulation, and fans were added on the external side of the chambers and in the bottom. Figure 2.21 reports the experimental results, which are commented upon below:

At time t = 0 the resistor supplies were switched on, and up to t = 1.2 h the fans were off with no water circulating in the pipes. It can be seen that the temperature increased strongly, up to more than
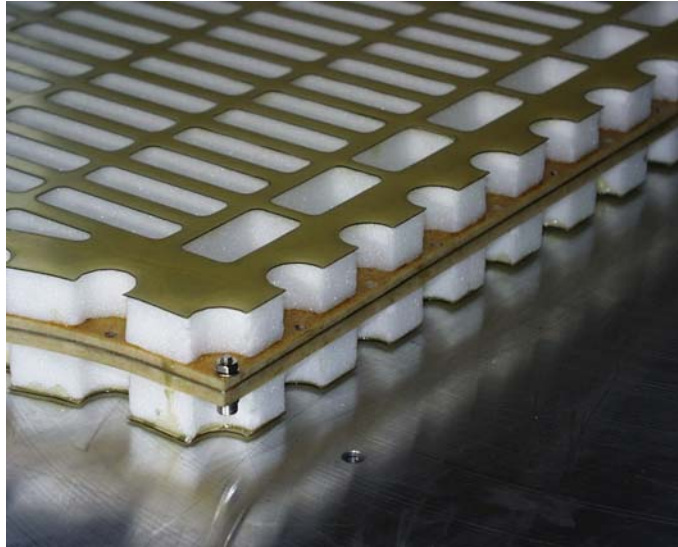
Figure 2.19: Detail of the frameless chambers.
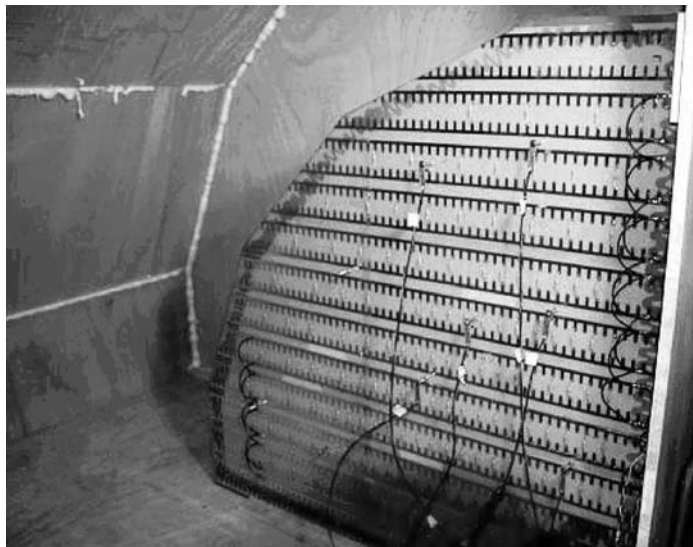
Figure 2.20: Quarters of Station 1 inside the cylinder. The cables are used for the temperature read-out.
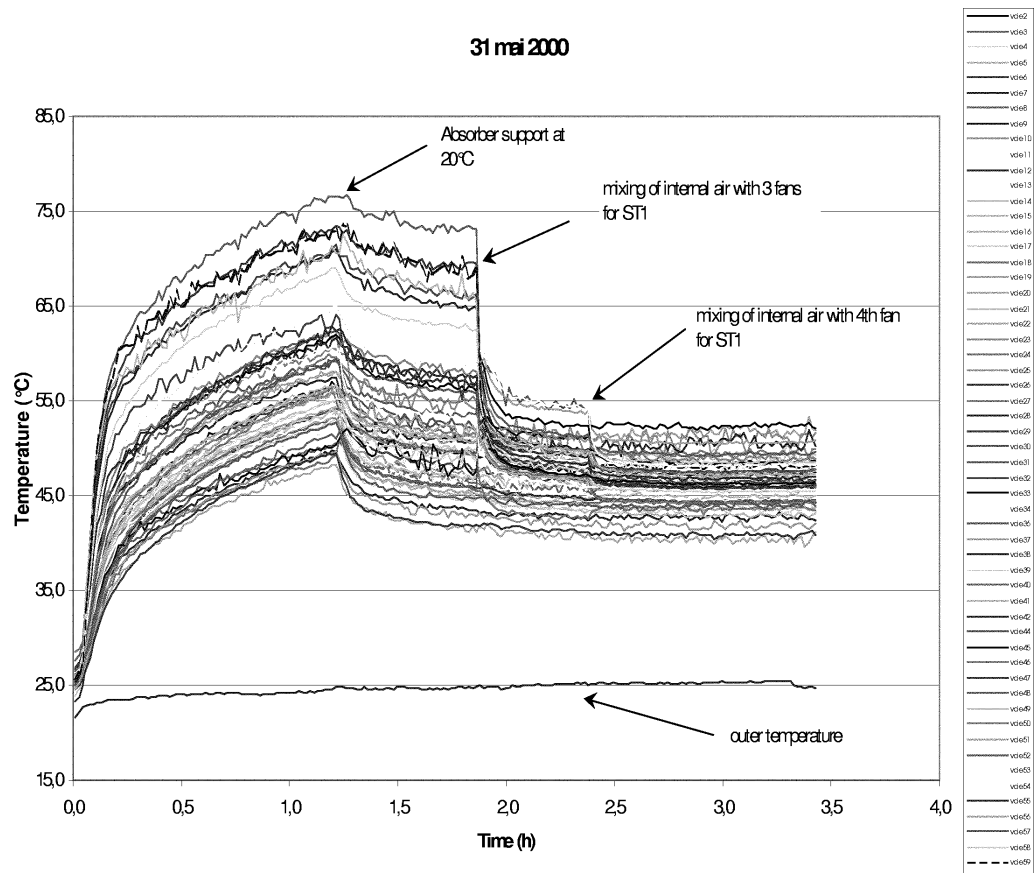
Figure 2.21: Measurements of the cooling set-up efficiency for different air-circulation arrangements.

75°C (depending on where the sensors were located), without achieving an equilibrium. At time t = 1.2 h, water was circulated in the pipes: the temperature slightly decreased and achieved an equilibrium at a time of about t = 1.8 h. When three of the 4 fans were started the temperature went down to less than 55°C. Switching on the fourth fan equilibrated the temperature under 52°C in the worst case. It can also be seen that, for a given chamber, the difference between the extrema does not exceed 14.5°C for the worst case (planes of Station 2 in front of the dipole) and that the ambient air in the final phase of the measurements was 5 to 7°C higher than the expected temperature in the cavern. The consequences on the operation of the chamber should be negligible for the following reasons.

- The temperature coefficient of the amplifiers is very small (0.03 mV/°C) and the temperature does not exceed what is commonly found in a crate.

- The inside of the chambers is thermally well insulated from the outside thanks to a thick layer of foam (25 mm in the case of Station 2).

- The hot areas, if any, inside the chamber, where the gain will be higher, are located in front of small pads which individually collect less charge than the larger ones.

In parallel, extensive simulations have been performed. They reproduce experimental results with good precision and will be useful for looking for further possible improvements of the cooling system.

2.4 Modifications to Stations 3, 4 and 5

In the TDR, Station 3 had a mechanical architecture different from that of the group of Stations 1 and 2 on one hand and that of the group of Stations 4 and 5 on the other. In order to avoid these three different station types, it has been decided to adopt a 'slat' architecture for Station 3. The main reason for this was the possibility to use the same technology as for the Stations 4 and 5.

Nevertheless, considering the specificity of Station 3 (free room, cooling, mounting, etc.) due to its location inside the dipole magnet, a direct extrapolation from Stations 4 and 5 cannot be applied. Moreover, Station 4 will not be a simple copy of Station 5: the number and length of the slats will be different to better cover the acceptance and to reduce the price. In that case, the chambers of Station 4 will have fewer PCBs in smaller slats.

Since the TDR, the arrangement of the slats inside a chamber has been optimized. In particular, a slat has been included in the middle of a half-chamber. For the same reason and because of space constraints inside the magnet, some PCBs in the outer part of the first chamber of Station 3 will have to be cut. The two chambers of Stations 4 and 5 remain identical .

The following sections will present prototype test results, changes in the segmentation, in the structure of the slats, in the frames and in the cooling.

2.4.1 Prototype in-beam test results

Several cathode pad chamber (CPC) prototypes have been developed and tested in-beam at CERN PS by different groups. The main goal was to determine the basic characteristics of the chamber (noise, gain, resolution, efficiency, etc.), in order to validate the choice of the pad segmentation. The mechanical aspects were the subject of an R&D programme in laboratories, concerning the structure and closure of the chamber, and the machining and gluing of the PCBs. The CERN tests have also validated parts of these aspects using 40×40 cm^2 active area prototypes.

All the tested prototypes give similar results, so the longest one (1.2 m) will be described in more detail.

2.4.1.1 Experimental set-up

Tests were performed with negative pions of 7 GeV/*c* at the PS (one week in May 2000). An 'ultimate' resolution cannot be achieved at the PS, because of non-negligible multiple scattering.

As described in the TDR (Section 2.3.1), prototypes were mounted on a test bench which allowed vertical and horizontal displacements by hand. The prototype was located between a set of ten silicon strip detectors, located along the beam axis, that defined the telescope for the tracking system. Five planes were used to measure the *x* coordinate (two upstream and three downstream of the prototype), while the other five measured the *y* coordinate (again two upstream and three downstream). Each silicon detector was 300 μm thick with 192 strips of 50 μm pitch ($\simeq$ 15 μm resolution). The trigger system was defined by the coincidence between two pairs of crossed plastic scintillator blades, located upstream (overlapping surface = 2×2 cm^2) and downstream (overlapping surface = 1×1 cm^2) of the prototype.

2.4.1.2 Description of the prototype

Mechanical description   The prototype is very similar to a slat module described in the TDR (Section 2.4.5.3). The main differences in the design are the following.

- The sandwich panel of carbon–Rohacell-carbon is replaced by one of carbon–Nomex honeycomb– carbon.

- A Nomex foil (high permittivity) is glued between the carbon skin and the PCB in order to reduce the capacitive noise.

The prototype is 1.2 m long with an active size of 40 × 120 cm^2 (three PCBs per cathode plane). The anode wires (W-Re: 20 μm diameter gold plated) are soldered. The gas sealing is obtained by a silicon joint which allows quite easy opening of the chamber.

Electronics   The read-out electronics for the tracking system and prototype used the same method of multiplexed charge measurements. The prototypes used the 1.5 μm GASSIPLEX chips, whose basic characteristics are described in more detail in Section 2.3.10.2 of the TDR. These chips were mounted on-board, and performed the charge preamplification, filtering, shaping and 16-channel multiplexing. The single analog outputs were then transmitted to a 10-bit C-RAMS ADC (CAEN) for coding.

Gas   The gas mixture used was the standard 80% Ar + 20% CO$_2$.

Pad segmentation   The bending cathode had only one segmentation type of 2.5 × 0.5 cm^2, corresponding to the standard high density, while the non-bending cathode had three different pad sizes, (0.7143, 0.5, 1) × 2.5 cm^2.

The aim was to study the electronic noise, to determine the resolution and the efficiency for the different pad sizes, and to study the charge correlation between the two cathodes. Unfortunately, owing to cabling connection problems, only a few configurations have been studied.

2.4.1.3 Results

Electronic noise   The sigma of the pedestals are presented in Fig. 2.22. In the bending plane, the zones with different sigmas correspond to different GAS64 cards (4 × 16-channels GASSIPLEX). The following results correspond to the area with a sigma $\simeq$ 1.6 ADC channels. The non-bending plane, with larger pad sizes, has a larger noise, with an oscillating structure reflecting the mapping of the read-out strips of different lengths.
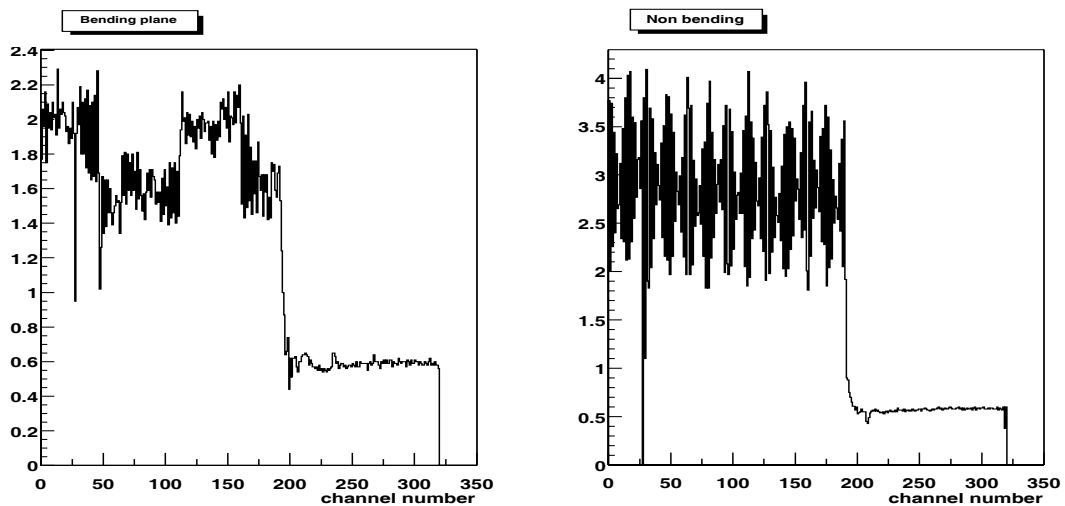
Figure 2.22: Sigma of the pedestals (in ADC channels) for the bending and non-bending planes.
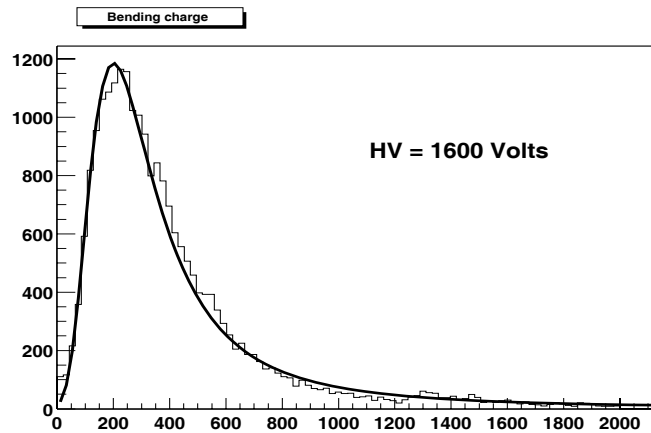
Figure 2.23: Typical charge distribution at 1600 V, fitted by a Landau function.

Gain An example of a charge distribution is shown in Fig. 2.23 for a HV of 1600 V. Figure 2.24 displays the relation between the peak of the Landau function, fitted to the distribution of the charge measured on the pads, and the anode-wire HV. As expected, it follows a linear behaviour on a logarithmic scale.

The absolute gain at 1650 V is around 3×10^4.

Data analysis To define a track from the silicon detectors, a 4σ pedestal subtraction has been applied online and only one hit per y plane has been required. A simple linear extrapolation to CPC is done without multiple-scattering correction.

Two cluster-finding algorithms have been used for the CPC: one searches for the pad with the maximum charge and adds to the cluster the two adjacent pads in the y direction, the other is a more general algorithm which connects all the adjacent hit pads in the y and x directions. The position of the cluster is obtained by a centre of gravity (COG) method.

The spatial resolution of the chamber is defined as the standard deviation of a Gaussian fit to the residual distribution of the expected track position on the CPC and the CPC impact point determined from a COG evaluation. Owing to the use of the COG method, the residual must be corrected for well-
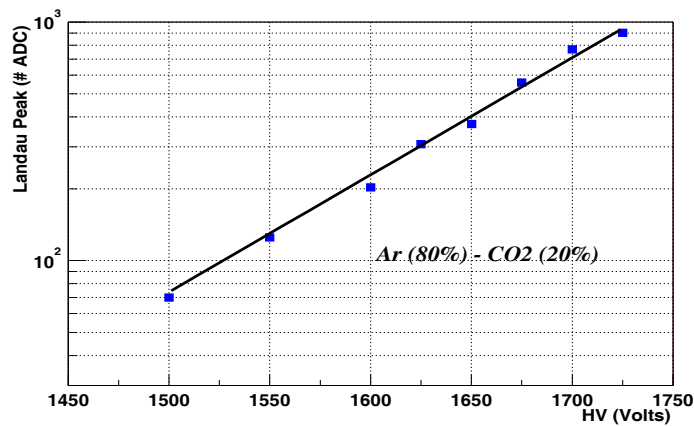
Figure 2.24: Relative gain as a function of the high voltage.
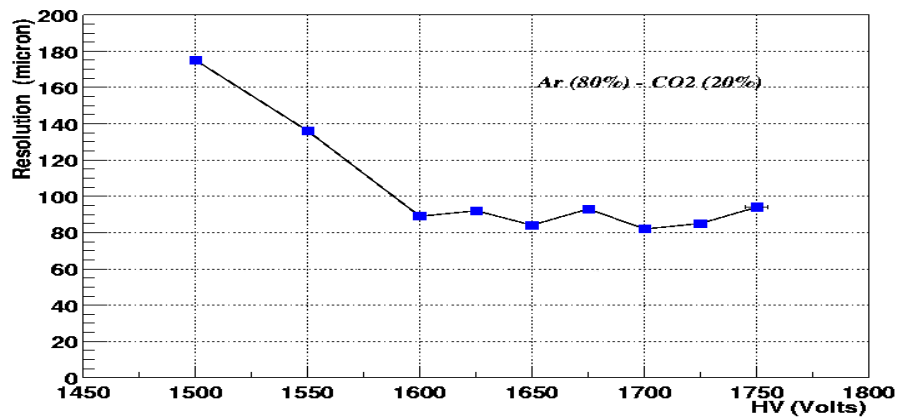
Figure 2.25: Evolution of the resolution with the operating high voltage (bending plane).

known geometrical effects (see TDR, Section 2.3.5.2).

Bending plane resolution and efficiency   The resolution and efficiency are plotted in Figs. 2.25 and 2.26 as a function of the HV. A cluster with a charge saturated pad is eliminated. A plateau begins at around 1600 V, where are reached a resolution $\simeq$ 80–85μm (without multiple-scattering correction, estimated to $\simeq 50\,\mu$m) and an efficiency $\simeq$ 93% for a cut at 3σ on the residual and $\simeq$ 97% for a $\pm$1 mm cut. This resolution and this efficiency are obtained with a cluster-finding algorithm using the maximum charge pad and the two adjacent ones; the more global algorithm gives slightly lower efficiency ($\simeq$ 90%) because of a worse resolution due to small charges on peripheral pads. The average number of pads per cluster is $\simeq$ 3.5 at 1625 V.

A typical residual plot is shown in Fig. 2.27 for 1650 V.

Non-bending plane resolution   The residuals from a COG calculation are shown in Fig. 2.27. A $\sigma = 713\,\mu$m is obtained, which is close to the expected value (anode pitch)/$\sqrt{12}$.

Charge correlation and ghost-hit rejection   As explained in Section 2.3.8.3 of the TDR, it seems natural to use the correlation of the charges induced on opposite cathode planes for the rejection of ghost hits. The observed correlation (see Fig. 2.28) follows roughly a straight line and the ratio (non-bending
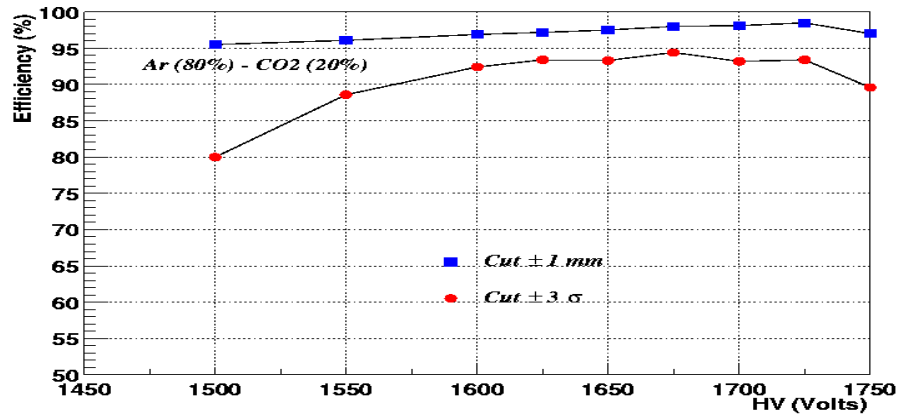
Figure 2.26: Reconstruction efficiency as a function of the high voltage (bending plane).
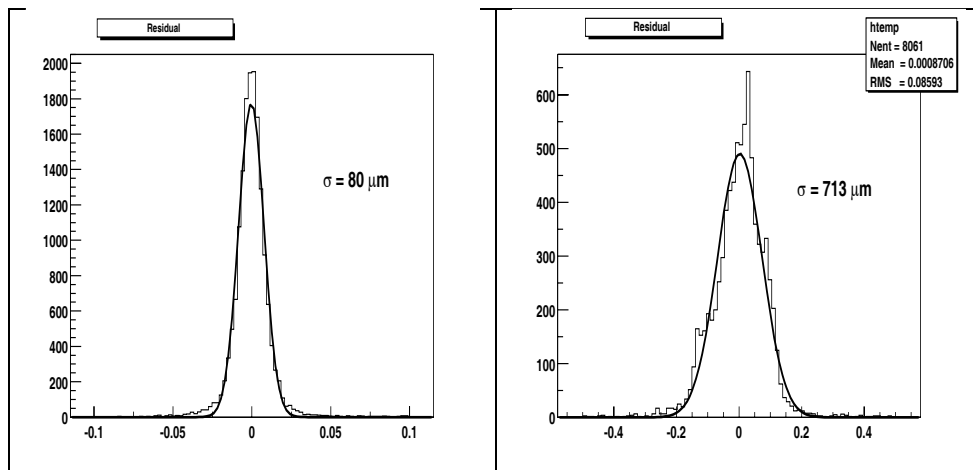
Figure 2.27: Resolution in the bending plane (left) and in the non-bending plane for a pad width of 7.143 mm (right).
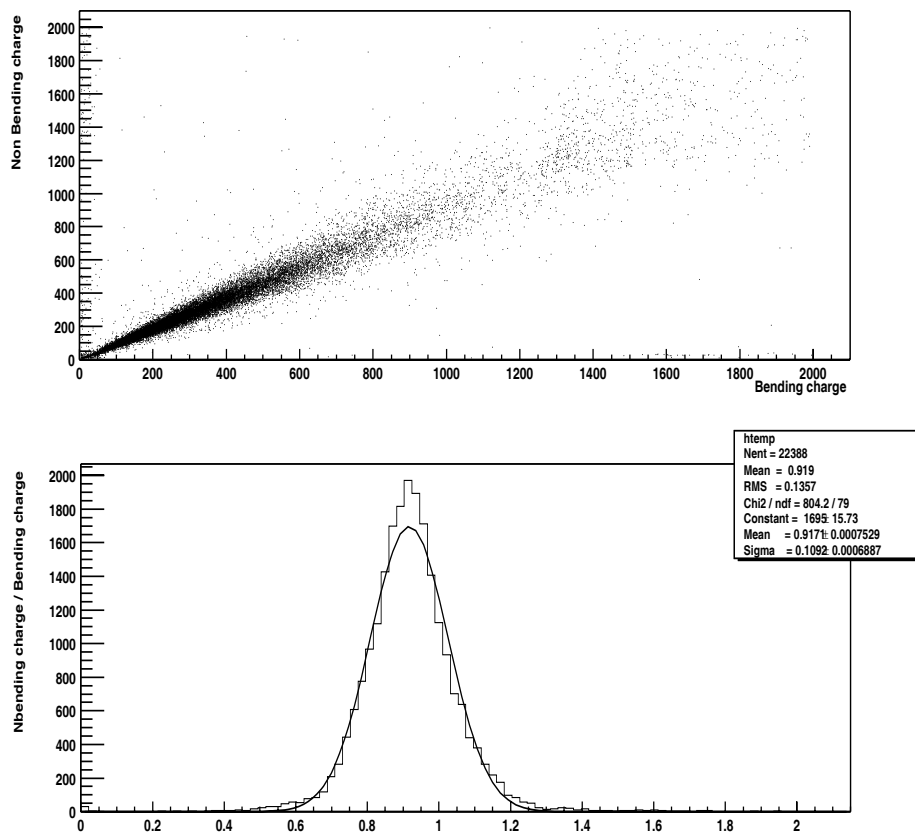
Figure 2.28: The correlation between charges induced on opposite cathode planes (top picture) and the ratio of these charges without electronic calibration (bottom picture).

charge)/(bending charge) has a dispersion of $\sigma \simeq 0.11$. The shift of the mean value of this ratio is due to a non-calibration of the electronic channels between the two cathodes.

From the 11% dispersion on the charge ratio, the number of misidentified hits has been simulated: In the case of two particles in a same area (meaning two possible ghost hits), which is by far the most probable case, 5% of the hits are misidentified.

The ghost problem will arise mainly in the zones of the large stations where the pad length is 10 cm, both in the bending and the non-bending planes. Considering the foreseen density in this region, the probability of having two background hits in a 10×10 cm^2 area is small, between 0.5% and 3%. Nevertheless, the number of times that a muon hit from an upsilon is accompanied by a background hit lays between 13% and 20%. These are the events for which the charge correlation will be useful to reject ghost hits. From these events, 5% will be misidentified, leading to a number of misidentified upsilon hits of $\approx 1\%$.

2.4.2   PCB configuration and occupancy

More precise simulations have become available since the TDR concerning the particle distributions coming from the interaction. In particular, the beam absorber has been optimized (see Section 6.2) and simulated in a more realistic way, leading to a new set of hit densities in the chambers (see Fig. 6.2). On the other hand, some progress has been made also on the side of chamber response modelling and the

Table 2.3: Pad segmentation for each PCB type in the bending plane (*y*).

PCB type	Δx (cm) $\times \Delta y$ (cm)	Number of MCMs	Number of channels
1	2.5×0.5	20	1280
2	5×0.5	10	640
3	10×0.5	5	320

Table 2.4: Pad segmentation for each PCB type in the non-bending plane (*x*).

PCB type	Δx (cm) $\times \Delta y$ (cm)	Number of MCMs	Number of channels
1	0.7143×2.5	14	896
2	0.7143×5	7	448
3	0.7143×10	4 (3.5)	256

results presented here come from a full simulation including the pad response.

2.4.2.1   Pad sizes

The active area of each PCB (40×40 cm^2) remains as in the TDR. The pad sizes in the bending plane are the same as in the TDR (Table 2.3), but for the non-bending plane, pads with a width of 7.143 mm are used now after validation in test beam (see previous section). In particular, the resolution achieved in the non-bending plane is of the order of 2.5 mm $/\sqrt{12} \simeq 720 \ \mu$m, fullfilling the tracking requirements (~ 1 mm). The new pad sizes for the non-bending plane are given in Table 2.4.

2.4.2.2   Chamber segmentation

The distribution of each PCB type in the chamber is done to keep the maximum occupancy at the level of 5–6%, which is required by the tracking algorithm. Figure 2.29 shows the PCB configuration for each of Stations 3, 4 and 5 and the corresponding occupancy is shown as a function of the radius in Fig. 2.30.

The number of PCBs of each type and the corresponding number of channels for each station are given in Table 2.5. The total number of PCBs needed is 1160 and the total number of channels is 640,256. The number of channels has been reduced by 25% in Station 3 and by 18% in Stations 4 and 5 compared to the TDR.

2.4.3   Slat structure

The basic design of one slat is the same as that described in the TDR (Section 2.4.5.3), but differences appear in some of the materials and dimensions of its components.

PCBs are aligned and glued on a lightweight, all-in-one-block carbon–Nomex honeycomb–carbon sandwich (Fig. 2.31). The Nomex honeycomb core has replaced Rohacell and becomes 8 mm thick. The thickness of each carbon skin remains $2 \times 100 \ \mu$m. The 20 μm diameter anode wires are expected to be

Table 2.5: Number of PCBs of each type for the bending (*y*) and non-bending (*x*) planes and the corresponding number of channels for Stations 3, 4 and 5.

Station	Type 1 ($x + y$)	Type 2 ($x + y$)	Type 3 ($x + y$)	Number of channels
3	32 +32	88 + 88	0	165,376
4	40 + 40	80 + 80	76 + 76	217,856
5	40 + 40	80 + 80	144 + 144	257,024
Total	224	496	440	640,256
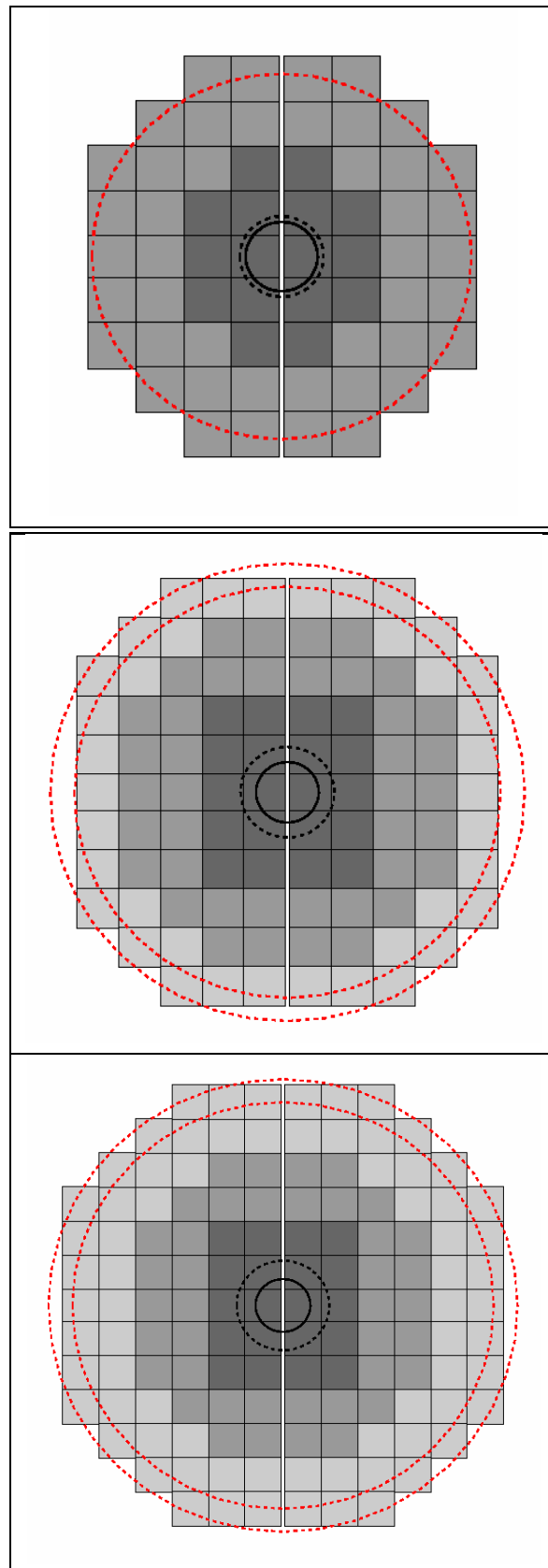
Figure 2.29: PCB distribution in the chamber for Station 3 (top), 4 (centre) and 5 (bottom). PCBs of type 1 (dark grey), type 2 (mid-grey) and type 3 (light grey) are shown. The 9° and 10° limits are also shown (dotted lines).
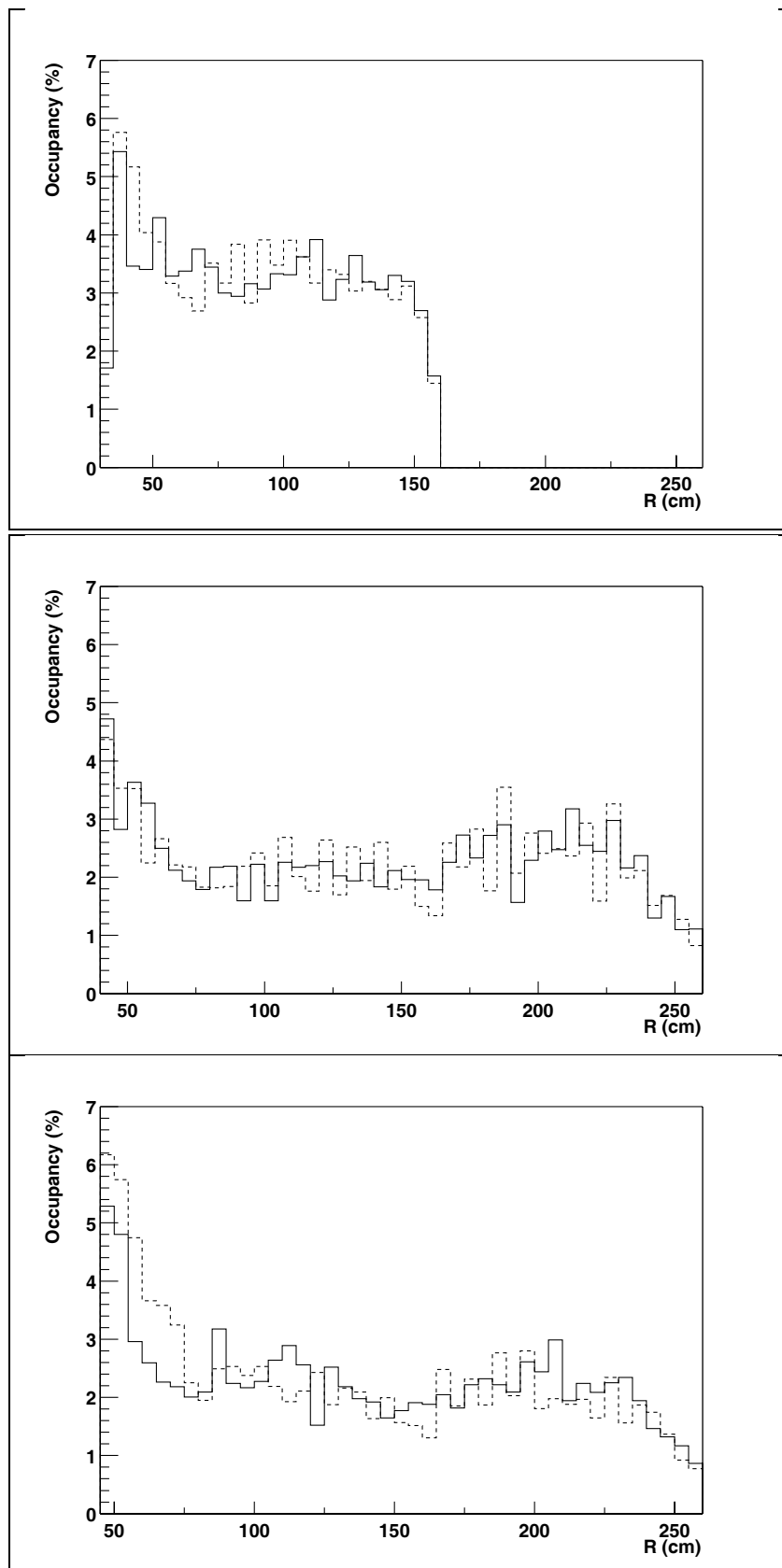
Figure 2.30: Occupancy in per cent as a function of the radius for Stations 3 (top), 4 (middle) and 5 (bottom). Solid line is for the first chamber of a station, dotted line for the second.
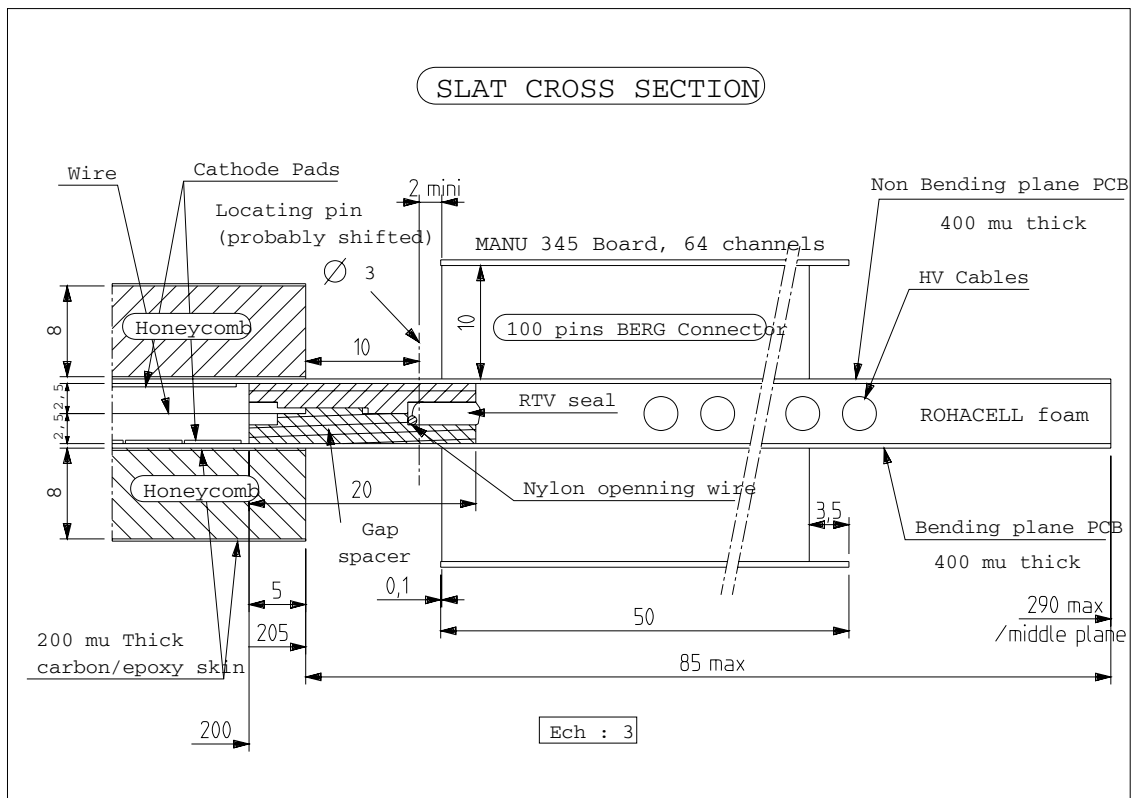
Figure 2.31: Slat cross section.

glued with epoxy resin directly on the gap spacer (see Fig. 2.32). The epoxy resin is Araldite 2011 from Ciba-Geigy. Electrical connection between wires and HV supply is achieved by conducting tape. This type of gluing has been validated by several tests. Three guard wires are foreseen on each slat side.

The dimension of one PCB becomes 400×580 mm^2 (instead of 400×600 mm^2), while the active area remains 400×400 mm^2. The PCBs could be made from 400 μm thick glass/epoxy FR4 HTG, under investigation, which performs better in terms of dimensional stability than standard FR4, even if the latter remains a good candidate. The PCB thickness has partly been chosen for impedance matching with a digital data bus. The pads will still be etched on the internal skin of a sandwich cathode, with readout strips on the other side, the two connected to each other by vias. The etching on PCB will use a 9 μm Cu coating or a standard 17 μm as base copper thickness, which increases the thickness by only 0.11% of X$_0$. The final Cu thickness becomes 20–25 μm, taking into account the recharging of the Cu. The inter-pad distance is 500 μm in the x direction and 250 μm in the y direction. The read-out strips are 180 μm wide with a 625 μm pitch.

Following machining tests, the positioning of the PCBs no longer uses survey marks, but is done with respect to the central pad. Once positioned, two holes are punched (better than drilled) through the PCB (with a ± 10 μm precision) with the same distance as the one on the sandwich panel. The PCB is then cut using a tooling (under study) giving the same precision as the punching. The following assembly on the panel is then much easier, requiring only a good planarity of the assembly table (± 20 μm/m).

The low voltage needed for the electronics cards is supplied by a 15 mm^2 cross-section Cu bus soldered on the PCBs. For the HV, one HV channel per slat is foreseen. To limit the effects of failed wire or leakage current, a system allowing smaller HV segmentation (20 or 40 cm) is under study.

In order to avoid mechanical parts like screws and bolts, and to minimize the amount of matter and manpower, modules will be sealed with RTV resin. It will therefore be possible to open modules after
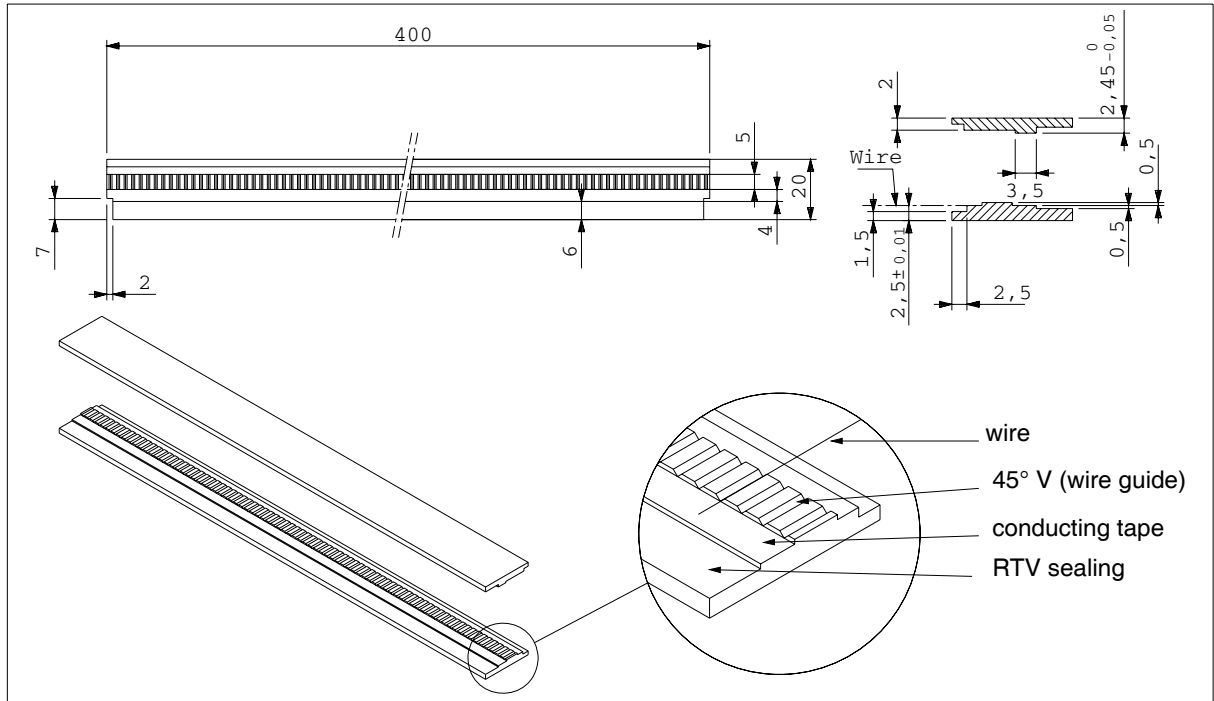
Figure 2.32: Slat spacer.

assembly, even if this operation needs more time than with the O-ring design.

Not foreseen at the time of the TDR, some of the slats, close to the beam pipe, will have a circular shape to minimize hit losses. This kind of slat is under study in laboratories and will be tested in-beam in spring 2001.

The average thickness of a chamber, including electronics but without cables, remains below 2% of X_0 with a 'peak' at 2.4% covering 3% of the sensitive area.

Dead area between the last sensitive wire and the end side of the slat has been reduced by about 7 mm compared to TDR drawings. The main consequences of this improvement are a smaller recess and reduced hit losses.

A spare is expected for each kind of slat, the total number of spares amounting to 15%.
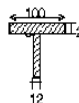
2.4.4 Mechanical support of the slats

2.4.4.1 Frame description
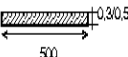
As described in Section 2.4.5.4 of the TDR, each half-chamber has its own frame. The frames are made of high modulus (Young modulus E = 120 GPa, density $\rho = 1.65$ g/cm^3) carbon/epoxy fibres in order to reduce their expansion due to temperature changes (this material has a very good thermal stability of 0.5×10^{-6} m.K^{-1}).

Each frame consists of three parts: the external C-shaped part, the vertical part and the central circular part, close to the beam. The four chambers of Stations 4 and 5 have the same frame design while chambers 5 and 6 of Station 3 have a slightly different design, owing to the loading and free room. Figure 2.33 describes the shape and the dimensions of the frame components.

The dimensions and the weight of the frames are displayed in Table 2.6 for Stations 3, 4 and 5. These frames have to support the slats with their associated cables (high and low voltages) and the incoming gas supplies. The total weight supported by the frame, including cables, is around 100, 180 and 230 kg for Station 3, 4 and 5, respectively.

Figure 2.33: Frame characteristics of Station 3 (top) and Stations 4 and 5 (bottom).

Table 2.6: Dimensions and weight of the frames of the last three stations.

Station	Height (m)	Width (m)	Weight (kg)
3	3.6	1.8	50
4	5.6	2.4	140
5	6.3	2.75	170

Considering this loading, a deformation of the frame is expected, mainly in the central circular part, leading to maximum horizontal and vertical displacements of 1.35 mm and 1.10 mm respectively on Station 3, and 3.4 mm and 1.7 mm on Stations 4 and 5. To reduce these latter values, a 500 μm thick carbon foil (less than 0.2% X_0) is stretched on the frames over the whole height and a width of 500 mm (see 'net' cell of Fig. 2.33). The achieved horizontal and vertical displacements become therefore 0.6 mm and 0.4 mm, respectively.

2.4.4.2 Assembly procedure

The assembly of the slats on the frames will be carried out vertically in an external assembly hall at CERN. The positioning of each slat is done with respect to survey marks both on the modules and the frames. Because of the pit access, the transportation to the working position will be done horizontally using an appropriate supporting tooling.

Measurement of the position of each slat is done by photogrammetry techniques. The final alignment will be done with particles.

Each module will be interchangeable without the need to mechanically realign. The realignment will be done, in this case, by the software analysis of physics events.

The frames will also be equipped with sight marks that will be used to measure and monitor the displacement of the whole chamber (see Chapter 4).

2.4.4.3 Support structure of the frames

The frames of Stations 4 and 5 are fixed on rails parallel to the x direction, to give the possibility to open a chamber. In order to minimize the hit losses due to the vertical part of the frames, the two half-chambers must overlap in the middle, by a distance corresponding to the width of this vertical frame (38 mm for Stations 4 and 5, 30 mm for Station 3). Therefore, each half-chamber hangs on a different rail. Figure 2.34 displays a view of Station 5, in running position and also with a half-chamber in an open position. The rails are also shown along with the cable supports on the side, where the cables arrive on a patch panel.

2.4.4.4 Hit losses

Three contributions to the hit losses can be distinguished: from the central circular part, close to the beam; from the outer part; and from the vertical frame.

Based on simulated Υ, the layout and the shape of the slats have been optimized to reduce the hit losses both in the central and outer parts of the chambers. In particular, close to the beam pipe the slats will have a circular shape, as already mentioned.

The main contribution to the losses comes from the vertical frames. Owing to the large sizes of the last two stations and their loading, the width of the vertical frame cannot be less than 38 mm for a thickness of 15 mm, as described in Fig. 2.33. In any case, the large slats need a read-out at both ends, because of the large number of electronic channels to be read. Therefore, cables will run along the vertical frame, making this area a dead zone. As already quoted in the previous section, the two frames of a chamber will overlap in the x direction in order not to increase this dead zone. Consequently, the projection of this dead-zone size to Station 3 leads to a dead area of 30 mm on this station. A width of 30 mm is then appropriate for the vertical frame of Station 3. The hit losses coming from these vertical frames, taking into account the inefficiency due to the guard wires, amount to 3.5%. The total hit losses from Stations 3, 4 and 5 stay at the level of 5%.
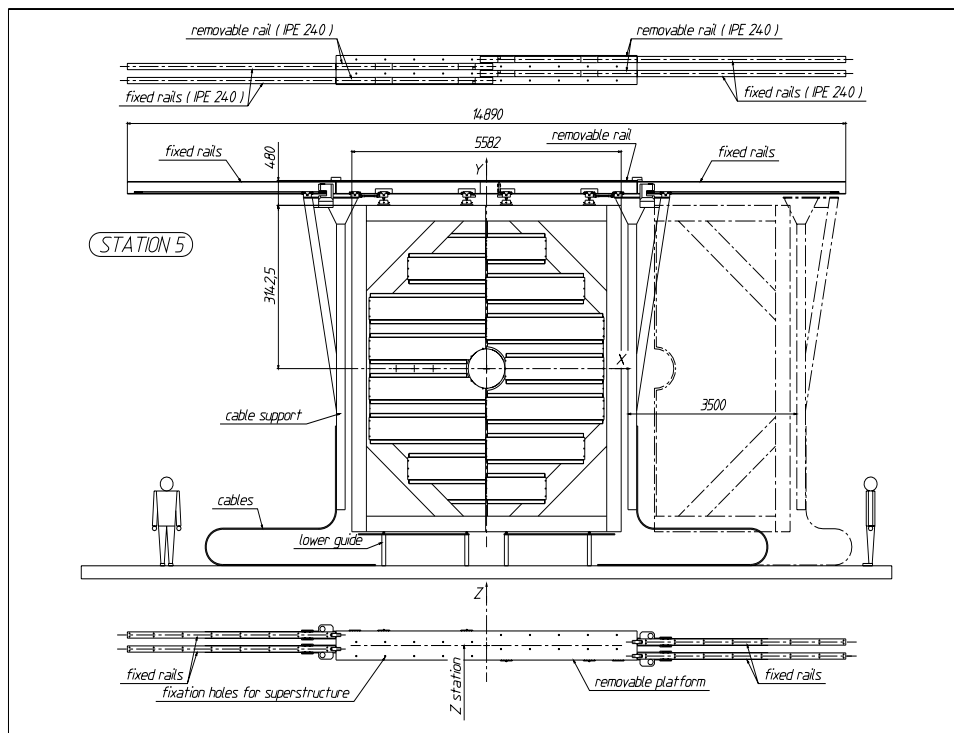
Figure 2.34: Station 5: slats are supported by the frames which are able to move along the rails upon which they are fixed. The cable supports are also shown on the side.

2.4.5   Cooling

Considering the present version of GASSIPLEX, the heat dissipation of the electronics amounts to 2.6 kW in Station 5, 2.2 kW in Station 4 and 1.6 kW in Station 3. The aim is to keep the electronics at a good working temperature and to not warm the experimental area.

Direct cooling by conductive exchange between component and water circulating in tubes is very efficient but inadequate because of the amount of matter in the sensitive area. A cooling based on circulating air has therefore been investigated.

Simulations with PROSTAR of a cover surrounding one station, with blowing air at $20°$C at the bottom of the station and with an extraction at its top, have shown a difference of temperature between top and bottom of $20°$C with a peak temperature at $45°$C in the centre. The flow was 600 m^3/h with a velocity always below 1 m/s (laminar flux). The drawback of this design is the difficulties of the integration. The cover has to be thin but resistant, must be able to open, with several apertures for cables and tubes, and needs a support. Moreover, such a design is not suited for Station 3 because of the lack of space.

In collaboration with the CERN integration team, a simpler solution is under study which considers a natural convection with an extraction of the air at the top of the station, without cover, for Stations 4 and 5. Simulations with an air temperature at the bottom of $20°$C give an average output temperature at the top of $29°$C for a 300 m^3/h flux and $26°$C for 600 m^3/h. The peak temperatures in a very small region in the centre are $40°$C and $31°$C respectively. For Station 3, a fresh air circulation from the bottom with a heat exchanger at the top is under evaluation: With an entrance temperature at the bottom of $14°$C, the output temperature at the top becomes $31°$C (peak temperature is $37°$C) for a 525 m^3/h flux.

Table 2.7: Comparison of MANAS and GASSIPLEX 0.7 μm characteristics.

	MANAS	GASSIPLEX 0.7 μm
Technology	SCL 1.2 μm	Alcatel-Mietec-0.7μm
Peaking time	1.2 μs	1.2 μs
Noise at 0 pF	640 e$^-$rms	530 e$^-$rms
Noise slope	11.58 e$^-$rms/pF	11.2 e$^-$rms/pF
Dynamic range (+)	500 fC	560 fC (0 to 2 V)
Dynamic range (-)	275 fC	500 fC (0 to -1.1 V)
Gain (+)	3.5 mV/fC	3.6 mV/fC
Analog read-out speed	10 MHz (max.)	10 MHz (50 pF load)
Power consumption	7 mW/channel	8 mW/channel at 10 MHz
Output temp. coefficient	0.03 mV /$^\circ$C	0.05 mV /$^\circ$C

2.5 Electronics

Compared to the TDR, some changes have been made to account for the new chamber designs.

- Instead of one MCM type for all chambers, it has been decided to study two different types of shape: one for Stations 1 and 2 (MANU12) and one for Stations 3, 4 and 5 (MANU345). Both types will be built in SMC technology instead of bare dies bonding. This choice has been made to simplify the tests of the chips before mounting, to allow the replacement of one defective chip and to reduce the cost because of a better yield. Moreover there will be two ADCs per MCM for optimizing the power consumption. MANU12 has a very tight size constraint because of the pad sizes in the first two stations. With this new design, the overall dimensions are 23 $\times$ 63 mm^2 instead of 27 $\times$ 75 mm^2. These modules have four connectors: for low voltages, for command signal distributions, for the digitized data and for the Kapton foil connecting the pads to the preamplifiers. In the MANU345 configuration, the size constraints are less stringent (32 $\times$ 50 mm^2) and these modules are directly plugged on the slat PCB, thus requiring only one 100 point connector.

- Two new preamplifiers are now available.

  - GASSIPLEX: 0.7 μm (instead of 1.5 μm) with performances better adjusted to the tracking chamber specifications. The difference lays mainly in a smaller gain (3.5 instead of 11 mV/fC) leading correlatively to a larger dynamical range, and to standard voltages for the command signals.
  - MANAS: The first engineering chips (in 1.2 μm technology) of the Indian version of the GASSIPLEX have given encouraging results with performances quite similar to those of the GASSIPLEX. The main characteristics are summarized in Table 2.7. Some results can be seen in Figs. 2.35 and 2.36. The second iteration (foreseen for April 2001) should correct a remaining problem on a Track and Hold leak and on the chip overall sizes.

- The first MARC chip was completed in October and the tests have shown that about 80% of the chip functionalities were working correctly. After correction of the defects, a second iteration has been launched and the new version will be available by the beginning of February 2001.

  To summarize, the MANU cards, which will also be called slave stations in the next paragraph, now have the following functionalities which are schematically represented in Fig. 2.37:
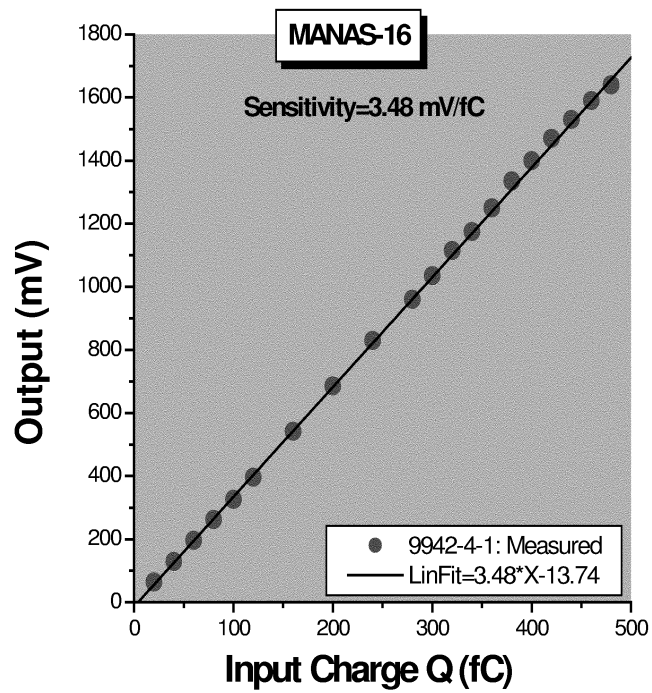
Figure 2.35: Linearity measurement of the MANAS response versus the input charge.
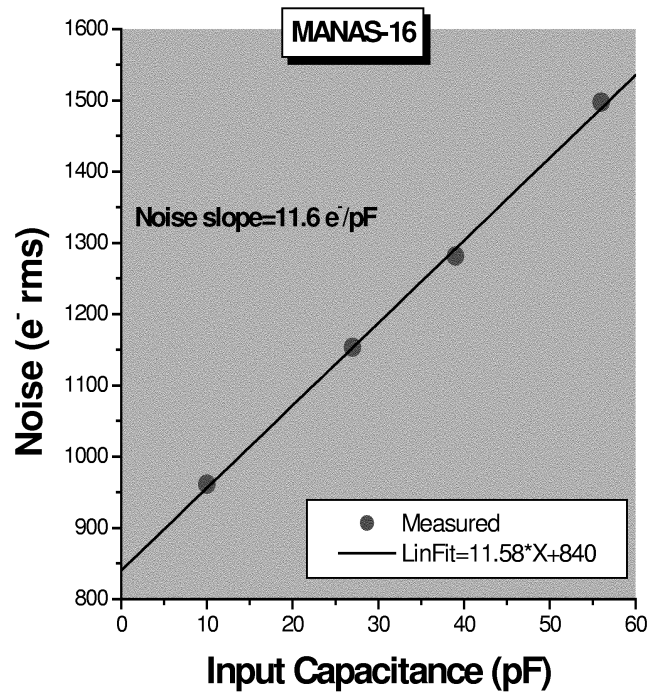
Figure 2.36: Slope of the noise versus the input capacitance.

MANU12 & MANU345
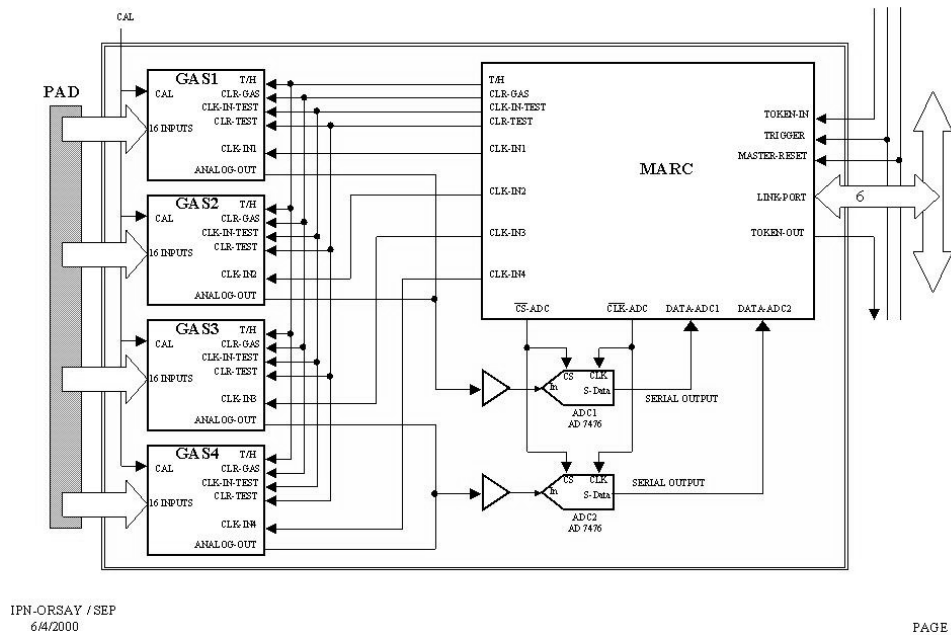
Figure 2.37: Scheme of the MANU architecture.

– amplification and filtering of 64-channel analog signals;

– 12-bit coding of the signals;

– selection of the hit channels after zero suppression, obtained by comparison with a threshold including the individual noise and pedestal of each channel;

– buffering of the data and interface with the read-out bus.

• CROCUS (Cluster Read Out Concentrator Unit System).

All the data of the chambers will be read by a read-out system located on the edge of the chambers. The MANUs (or slave stations) will be connected to DSP clusters (gathered on a board called CROCUS) via data buses named PATCH (Protocol for ALICE Tracking CHambers). Each bus is divided in two parts.

– A bus in LVTTL technology located on the chamber PCBs where up to 24 MANUs can be connected. This number limit is essentially due to the signal attenuation induced by the parasitic capacitance of each slave. Since the length of this bus is limited to about one metre, it is connected via a level translator to the LVDS bus.

– A bus in LVDS technology which does not present any length limitation in the present configuration. This bus is used for the connections between the LVTTL bus and the CROCUS board which can be off by several metres in the case of the largest stations.

These buses are bidirectional and connect N slave stations to one link port of the DSP (Analog Device 21160), which is the master station bus controller. They are used in one direction for downloading parameters towards the MANU (mainly the thresholds and the trigger signals) and in the other direction for the read-out of the data.

Figure 2.38: Schematical view of the read-out architecture.

Each CROCUS board is made of two times four DSPs associated with one concentrator DSP, which will collect the data coming from these eight DSPs before sending them towards the DDLs. This number of 2×4 DSPs per board could be easily extended if necessary.

A schematic view of this architecture is shown in Fig. 2.38. The bandwidth of the different elements is given in Table 2.8. An evaluation of the read-out time necessary for an average size event can be given:

-   t = 0 corresponds to the L0 trigger signal;

-   at t = 38 μs coding and zero suppression in the MANU boards are performed;

-   at t = 68 μs data are stored in the front DSPs;

-   at t = 88 μs data are transferred and built in the concentrator DSPs;

-   at t = 240 μs data transfer towards the DDLs is completed in the case of one DDL/CROCUS board. (If 2 DDLs are associated with each CROCUS board, this time is reduced down to 164 μs.)

A schematic view reported in Fig. 2.39 represents the layout of the different buses and CROCUS boards on the five stations.

Table 2.8: Bandwidth of the different components of the read-out chain

	Patch	21160 Host	DDL
Transfer rate	20 Mbyte/s	400 Mbyte/s	100 Mbyte/s
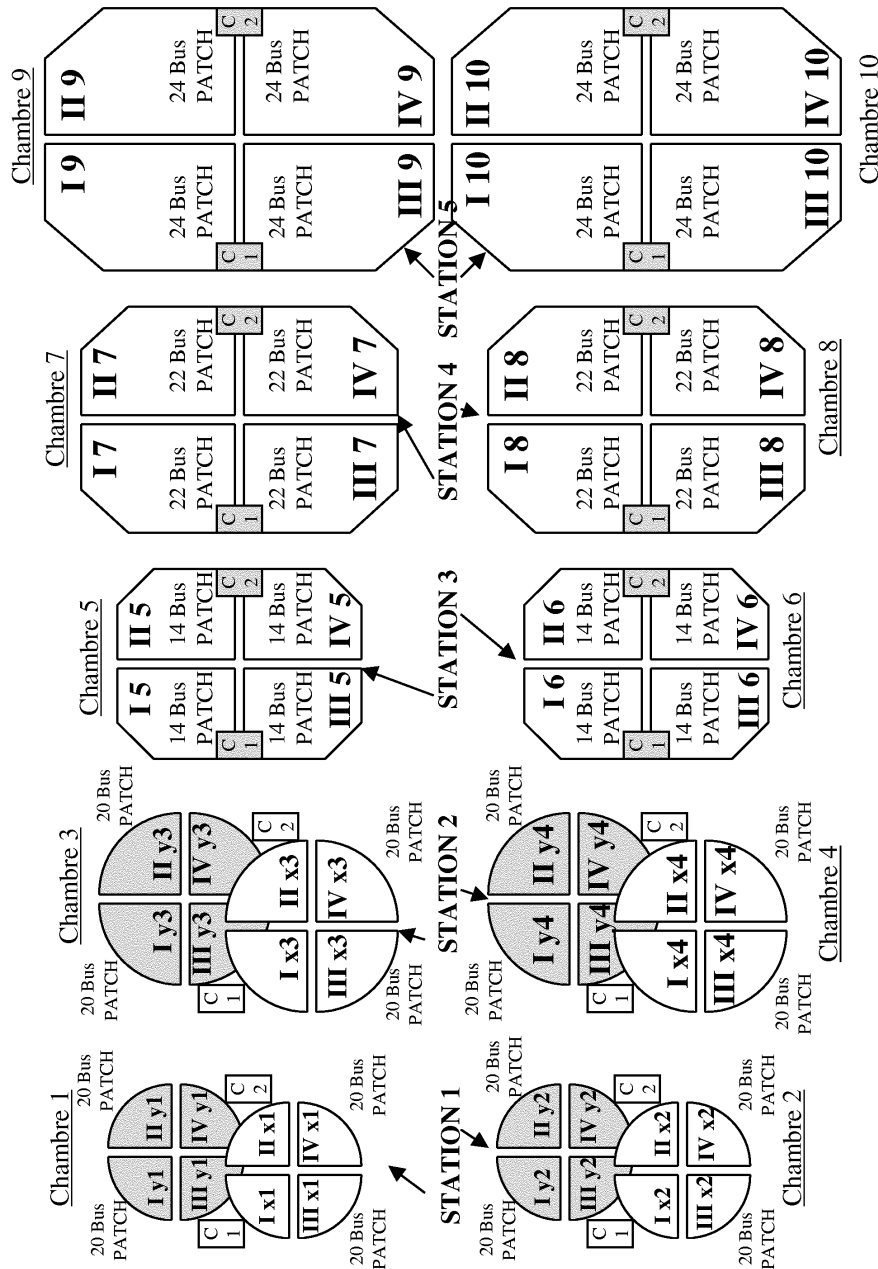
Figure 2.39: Read-out buses and CROCUS layout on the stations

2.6   Low-voltage supplies

In its last version, described above, the read-out electronics for the tracking chambers has an overall power consumption of 12 kW. This power has to be provided by three types of low-voltage supplies:

- for the analog part: V_{dd} = +2.5 V with 3600 W and V_{ss} = -2.5 V with 4700 W;

- for the digital part: V_{num} = +3.3 V with 3700 W.

These requested powers imply high-intensity currents with low voltages and, consequently, the energy efficiency of the electrical connections has to be carefully considered.

In this context, two schemes have been considered: one with the use of DC/DC converters and the other with the direct distribution of the required low voltages. Although for the DC/DC solution the benefit in terms of cable volume is obvious, the disadvantages are quite numerous.

- Because of the yield of these systems, there would be more dissipated power in the most crucial place, i.e. in the cylinder in which Stations 1 and 2 are enclosed.

- The overall dimensions of each of these converters are non-negligible and they need supports and radiators which will cause a lot of infrastructure problems essentially for the first three stations. Furthermore, because of the low power of these systems, about 500 units will be necessary for providing the requested power in the chambers. This large number of components will make all aspects of the slow control difficult.

- The ripple of this system is much higher than for classical solutions and is not compatible with the electronics requirements. Moreover, the operation of these DC/DC converters is noisy in the neighbourhood of analog electronics.

- As the first three stations are located in a high magnetic field, special versions of these set-ups will be necessary; it seems that very few types of such systems are available today.

- For operating DC/DC systems two power supply systems are necessary: one remote system for feeding the requested power and another for feeding the DC/DC converters with all the inherent additional cabling *in situ*. That means that the overall price of such a system will be higher than that of a classical one.

For all these reasons, it has been decided to use a more classical solution with a detector segmentation which allows an energy distribution by 25 A elementary modules. Three power supplies will be gathered in the same module and will be connected to each segment with the following aims.

- To simplify the energy distribution by using optimized cable diameters with regard to the cost, the rigidity and the weight.

- To simplify the supply design with moderate-size modules.

- To make the operation safe, thanks to the segmentation which minimizes the consequences of an electrical problem by inhibiting the given area of the detector. A schematic view of the power distribution is represented in Fig. 2.40.

The module number is fixed by the most demanding voltage (eg. V_{ss}) on the basis of a maximum current of 25 A. This conception, together with the new pad layout, implies 16 modules for Station 1, 16 for Station 2, 16 for Station 3, 20 for Station 4 and 24 for Station 5, which represents a total of 92 modules (without considering the spare modules).

The following characteristics are requested for these modules.
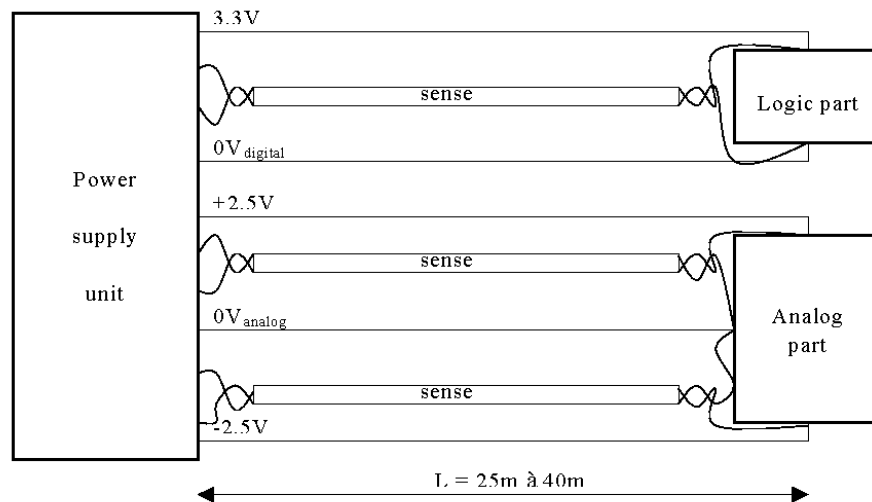
Figure 2.40: Scheme of the low-voltage set-up.

- The three power supplies are identical, totally independent and with floating grounding.

- They are regulated by sensors which are totally independent of each other. This regulation must be better than 10^{-3} with the following constraints:

  - the electronics is from 25 to 40 m apart and is fed by copper cables with sections of 16 or 25 mm^2;

  - voltage values vary between 2 and 5.5 V;

  - current values vary between 10 and 25 A;

  - the delivered voltages should not differ from the requested values by more than $\pm 1\%$;

  - the residual ripple should not exceed 2 mV from 0 up to 100 MHz.

The slow control of these power supplies will be done by a PC with an Ethernet interface which will allow to tune the voltages, to read the current values on each module, to switch on/off any module, to check the correct functionality of each element, etc.

An estimation of the cable weight gives 3300 kg for a 25 mm^2 section and 2200 kg for a 16 mm^2.

2.6.1   HV supplies and distributions

The philosophy adopted for the HV supplies is to divide the different stations in several parts for safety reasons and for operation convenience.

For Stations 1 and 2, it has been decided to power each chamber quadrant by four independent HV power supplies. Thus it is possible to switch off one of them in case of one wire breakdown or of one noisy wire without losing all the quadrant information. That means 32 independent channels per station. For Stations 3, 4 and 5, each slat will be fed by an independent HV channel to be able to optimize the value for each slat. That means 36 channels for Station 3, 52 channels for Station 4 and for Station 5. These 204 channels could be provided by eight CAEN 1833B modules packaged in a CAEN SY 1527 crate, this system being well adapted to the foreseen slow control.

3 Trigger system

3.1 Introduction

The trigger system was described in detail in the Technical Design Report of the dimuon forward spectrometer (TDR) [1]. Since then, the overall design has not changed and the work towards the final prototypes for the detector, the front-end and trigger electronics has progressed.

The mechanical suspension has however been redesigned (as described in Section 3.2) because the access scenario to the elements of the muon arm has changed.

A few items have also been studied further. As described in the TDR, single-gap Resistive Plate Chambers (RPCs), operated in streamer mode, have been chosen for the trigger detector. Some recent R&D results concerning essentially the choice of the electrode material are given in Section 3.3.1. Also, a new discrimination technique has been proposed and implemented in the front-end electronics chip to improve the timing performances of the detector (see Section 3.3.2).

Finally, a new independent detector called 'V0' will complete the existing dimuon set-up and is described in Section 3.4. The V0 detector aims at providing a fast interaction signal which will be used to validate the dimuon trigger decision, as was already foreseen at the time of the TDR (see for instance Section 3.1.4.2 of Ref. [1]). New simulation results confirm that it should help significantly in reducing the trigger rates from beam-gas induced collisions in p–p mode.

3.2 Modifications of the mechanical structure

Some modifications of the mechanical structure supporting the trigger detector are foreseen as a consequence of the new structure of the muon filter (iron wall). The latter is no longer movable (as it was in the TDR, see Sections 3.3.4 and 8.2.4.3 of Ref. [1]), but is fixed and has to be dismounted if, for instance, the last section of the beam shield has to be removed for some reason.

If the trigger detector is fixed to the muon filter (as was foreseen in the TDR) it would have to be disassembled when the muon filter is dismounted. Even if this event has a low probability, a trigger detector structurally independent of the muon filter is preferable. For this reason, the overall mechanical structure described in the TDR has been redesigned: the trigger detector half-planes are now fixed to a 'superstructure' mechanically decoupled from the iron wall.

The superstructure consists of two beams attached to a mechanical support (see also sect. 7). As shown in Fig. 3.1 and Fig. 3.2, the beams are orthogonal to the beam direction. The half-planes of each trigger station are fixed to the same beam, as illustrated in Fig. 3.3.

The structure of the new mechanical support also suggests a different procedure for the access and for the maintenance of the RPCs and of the front-end electronics. In the TDR the half-planes were moved along the z direction (i.e. parallel to the beam axis); now the access to the front sides of the RPCs can be more easily made in this new context by opening each half-plane in the x direction, orthogonal to the beam axis, as shown in Fig. 3.1 and Fig. 3.2. In this last figure the support chains for the cables, which allow the movement of the half-planes along the x direction, are also visible, as is the new position of the racks of the trigger electronics, which are now placed under the floor.

The mechanical structure of the detector half-planes has been slightly modified with respect to the TDR (see Section 3.3.3 of Ref. [1]) as a consequence of the new suspension system. As shown in Fig. 3.4 the sheaves of the read-out cables are at present attached to an independent column placed on the outer side of each half-plane. As can be seen in Fig. 3.3 and Fig. 3.4, the movement of the half-planes along the x direction is made with a chain and is guided by rollers. Finally, it is noted that the half-planes are
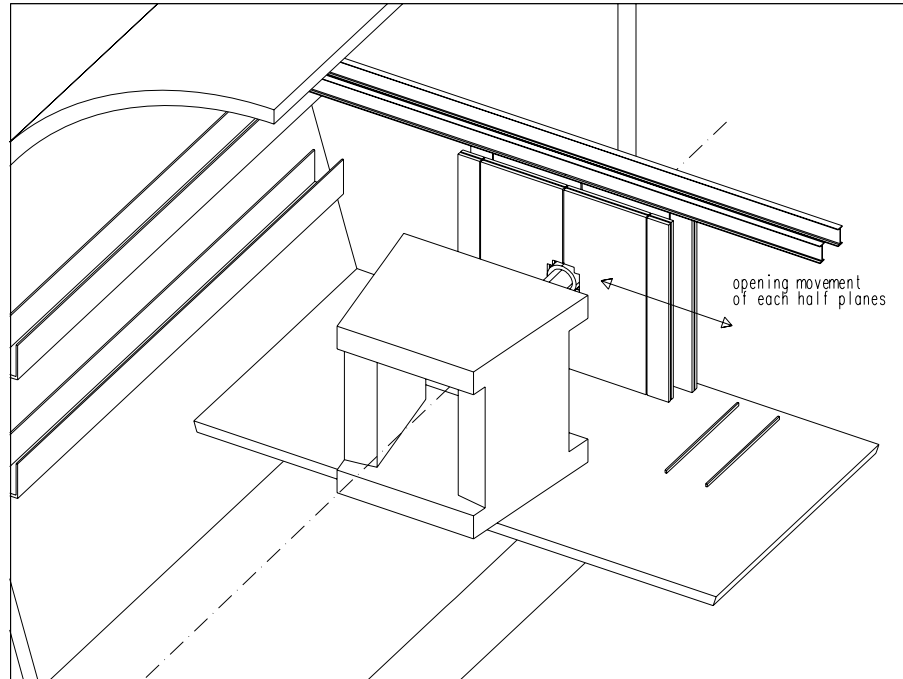
Figure 3.1: Perspective view of the trigger detector with its support beams in the ALICE cavern. For a clear presentation, the iron wall and the mechanical structure supporting the beams are not shown.

now supposed to be vertical even during data-taking. This simplification has been introduced following calculations which indicate that positioning the RPCs vertically (instead of orthogonal to the beam) has little impact on the trigger selectivity.

3.3   Recent developments

3.3.1   RPC detector: choice of the electrode material

The trigger detector is the same as in the TDR (see also Ref. [2]). According to the plans and milestones, tests have been (at the PS, July 2000) and will be (at the GIF, January 2001) carried out to compare RPC prototypes with electrodes made of different kinds of low-resistivity bakelite.

Two kinds of phenolic bakelites, produced by two different companies, have been tested at the PS. Their resistivities are about $3 \cdot 10^9$ Ωcm and $8 \cdot 10^9$ Ωcm. For the GIF test, a third kind of bakelite will be tested. This is a phenolic bakelite with a melamine foil on one side (the one in contact with the gas); its resistivity is about $1.5 \cdot 10^9$ Ωcm.

For the choice of the bakelite for the final RPCs, the long-term stability of the resistivity (for the different bakelites) has been studied in the tests mentioned above. It has been shown from laboratory measurements that the resistivity of bakelite samples kept in standard atmospheric conditions (both temperature and humidity) is stable, but a significant increase of resistivity has been observed [3] when a phenolic plate is kept in a box filled up with dry gas. To investigate this point, the following strategy was adopted for the PS test and is also foreseen in view of the GIF test. For each kind of bakelite, two RPC prototypes were prepared. For a period of about four months before the beam test, one prototype had been fluxed with our standard gas mixture for streamer mode (dry gas); for the other about 1% water vapour (humid gas) was added. Since RPCs are sealed off, it is not possible to measure the resistivity of the electrodes directly. To overcome this problem, 'dummy RPCs' have been built. Their electrodes are made of the same kinds of bakelite used for the RPCs under test and their structure is as close as possible to that of the standard RPCs. The main difference is that High Voltage (HV) cannot be applied
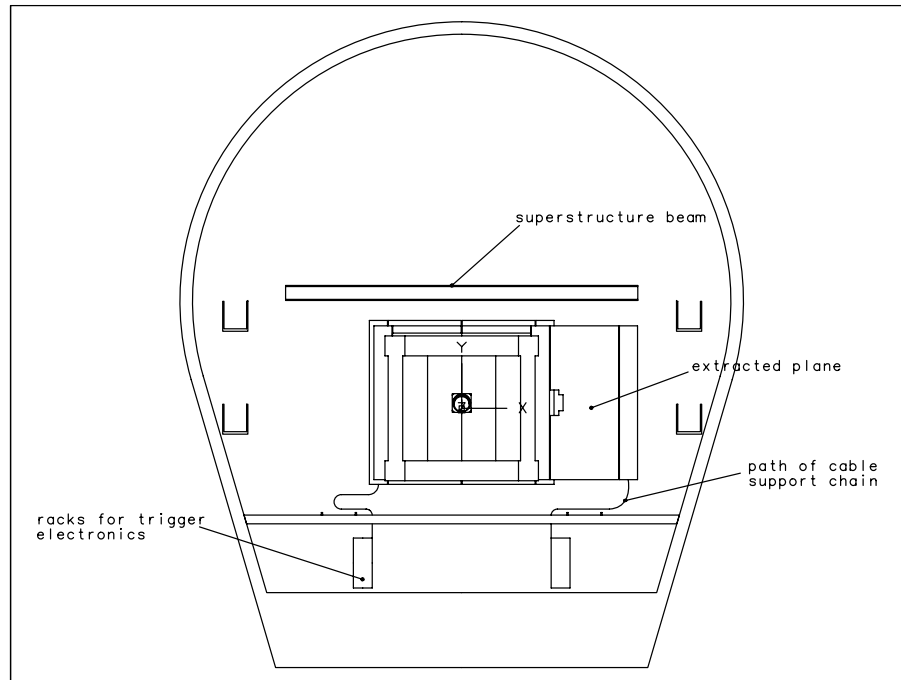
Figure 3.2: Front view of the trigger detector in the ALICE cavern.
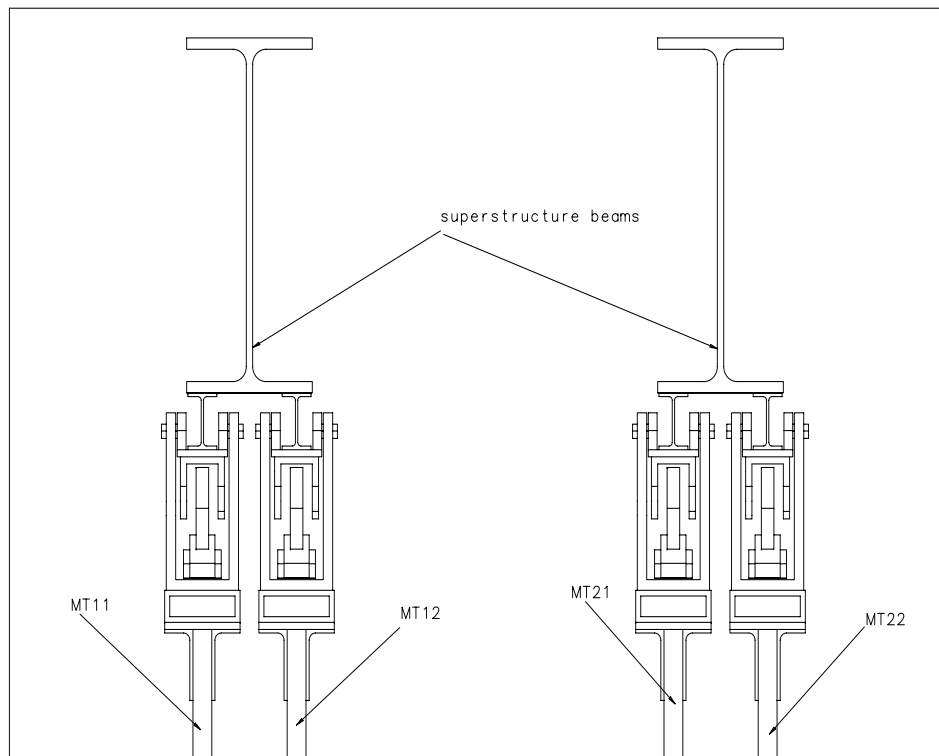
Figure 3.3: Side view of the trigger half-planes fixed to the superstructure.
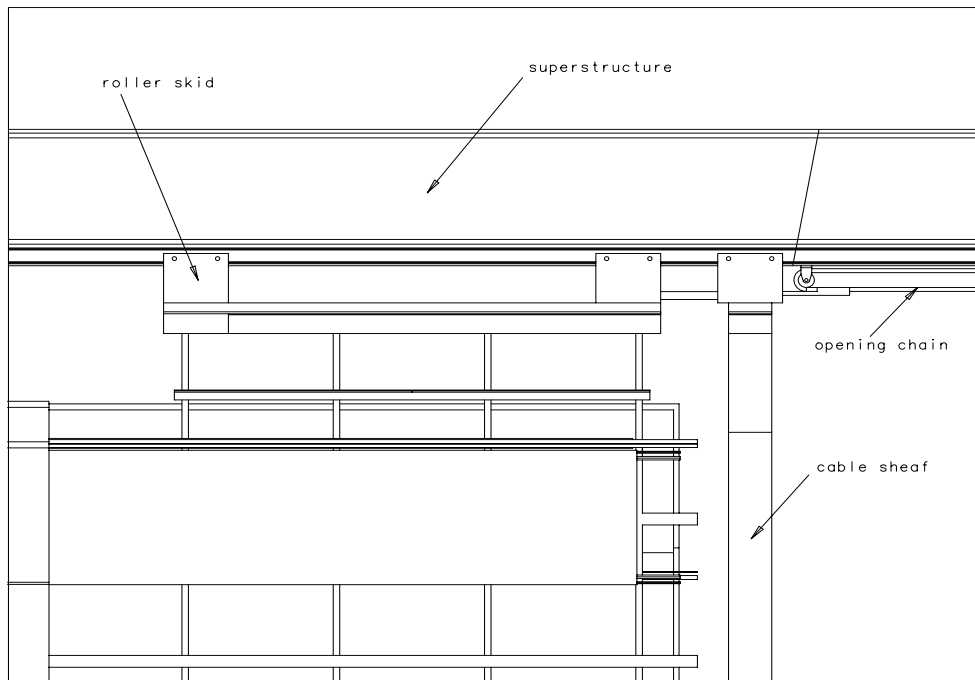
Figure 3.4: Front view of a trigger half-plane fixed to the superstructure.

to the dummy RPCs, although they can be opened to measure the resistivity of the bakelite plates. The dummy RPCs have been fluxed in parallel with the RPCs under test for a period of about four months, either with dry or humid gas mixtures. The results of these tests are rather similar for the two kinds of bakelite tested up to now and can be summarized as follows.

- Dummy RPCs: After four months, the resistivity of the plates fluxed with humid gas mixture is practically unchanged, while that of the plates fluxed with dry gas mixture shows a modest increase (by a factor 2–3), much smaller than that reported in Ref. [3]. These results are shown in Fig. 3.5 for the bakelite of higher resistivity.

- Beam test: The rate capability of the RPCs working in streamer mode and fluxed with dry gas is worse than that for RPCs fluxed with humid gas. The cluster size for humid RPCs is fully acceptable, although slightly higher than that for the dry RPCs.

In conclusion, the results of these tests suggest that, for the streamer mode, better rate capabilities can be reached if a moderate amount of moisture is added to the RPC gas mixture, although this implies a small increase of the cluster size. It is worth noting, however, that the increase of resistivity observed in these tests for the dry RPCs might be larger than in ALICE. In fact, to speed up the ageing effect, during the tests the detector gas volume was exchanged about 30 times per day, a value which is significantly higher than that foreseen during the ALICE data-taking (see Section 3.3.5 of Ref. [1]).

3.3.2 Front-end electronics

As announced in the TDR (see Section 3.4.1 of Ref. [1]), a prototype of the front-end ASIC has been designed and tested. The chip includes a new discrimination technique called ADULT (A DUaL Threshold) developed for improving the timing performances of RPCs in streamer mode. A detailed description of the ADULT method can be found in Ref. [4] and a technical presentation of the chip in Ref. [5].

Four examples of RPC pulses (Fig. 3.6), with quite different shapes, have been recorded at a HV of 9200 V with a digital oscilloscope. The left peak of small amplitude is attributed to an avalanche
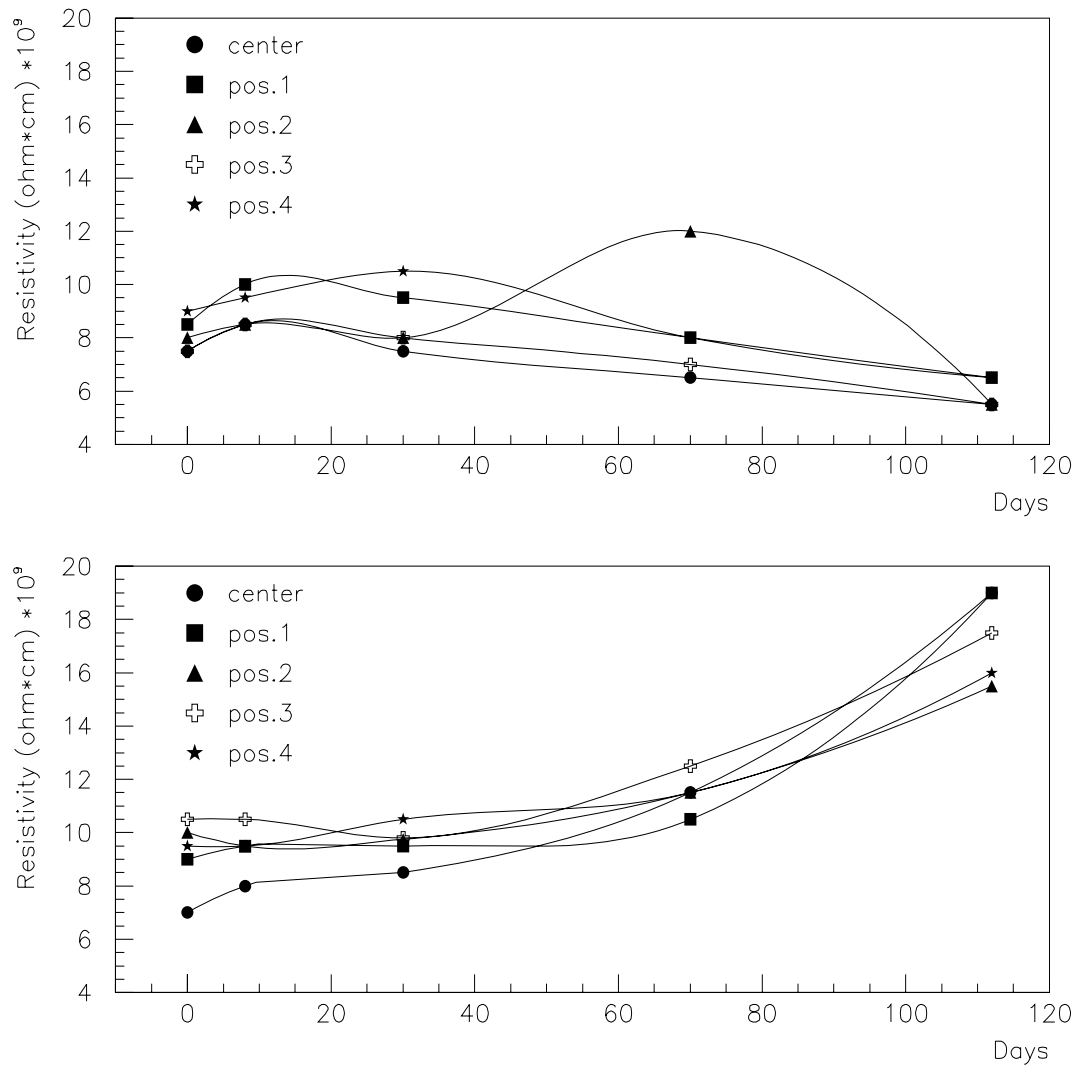
Figure 3.5: Evolution of the electrode resistivity of a 'dummy RPC' as a function of time elapsed from the beginning of the conditioning with humid (top) and dry (bottom) gas mixture. The symbols refer to different positions on the bakelite panel.

Figure 3.6: Samples of RPC pulses in streamer mode (same HV).

precursor while the streamer development creates the larger peak. If the gain is sufficient, the two peaks are almost superimposed. It can be seen that, compared to the streamer signal, the avalanche precursor shows very small time fluctuations.

The ADULT discrimination technique uses two discriminators: the first threshold (typically 10 mV/50Ω) at the level of the avalanche precursor and the second threshold (typically 80 mV/50Ω) at the level of the streamer signal. A coincidence of the two outgoing signals is then performed. The signal corresponding to the first threshold must be delayed (typically 10 ns) in order to give the time reference of the coincidence.

A diagram of one channel of the chip prototype is shown in Fig. 3.7. The technology is AMS BiC-MOS 0.8 μm. In addition to the ADULT stage, the chip includes a 'one-shot' which prevents retriggering within 100 ns and a remote-control delay (up to 50 ns). On the output, the signal is converted to a 20 ns wide ECL level for driving a 20 m twisted-pair cable. The present version of the chip has a power consumption of 140 mW per channel but the final one will include a LVDS driver to reduce it to less than 100 mW per channel. A RPC (50×50 cm^2) with an electrode resistivity of about $8 \cdot 10^9$ Ωcm, equipped with 2 cm wide strips read out by prototype chips, was run at the CERN/PS beam area in July 2000.

An example of time distribution with ADULT is shown in Fig. 3.8, left part, for a HV of 9200 V and the set of thresholds (10, 80) mV. A narrow time peak ($\sigma_t^{peak} < 1$ ns) was observed, followed by a tail containing a small fraction of the events ($< 2\%$, see the insert in vertical logarithmic scale). For comparison, in the right part of Fig. 3.8 is plotted the time distribution normalized to the same number of events when reading out the RPC with a single threshold discriminator (80 mV threshold).

Beyond the time resolution, the most relevant parameter is the efficiency at the sampling frequency of the trigger electronics (40 MHz, 25 ns). The left part of Fig. 3.9 displays the efficiency at 15, 100 and 450 Hz/cm^2 fluxes on the RPC, in a 25 ns gate. The efficiency reaches a plateau at 98% efficiency for all the fluxes.

It is also important to preserve the full efficiency in a narrower time gate in order to account for any possible jitter sources between different front-end channels when operating a large-area detector. For
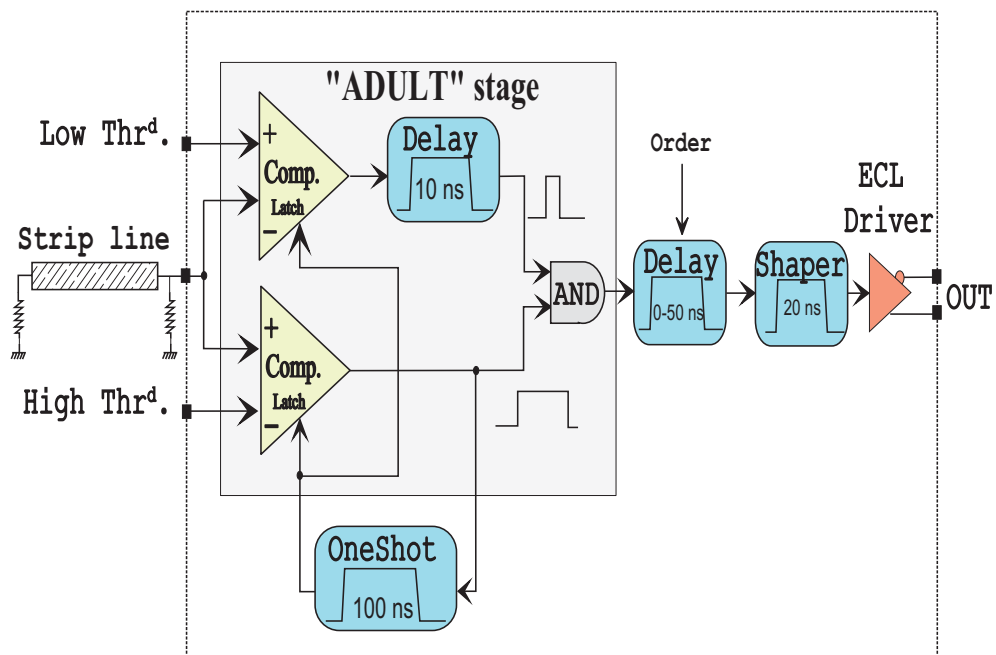
Figure 3.7: Block diagram of a single channel of the ADULT chip.
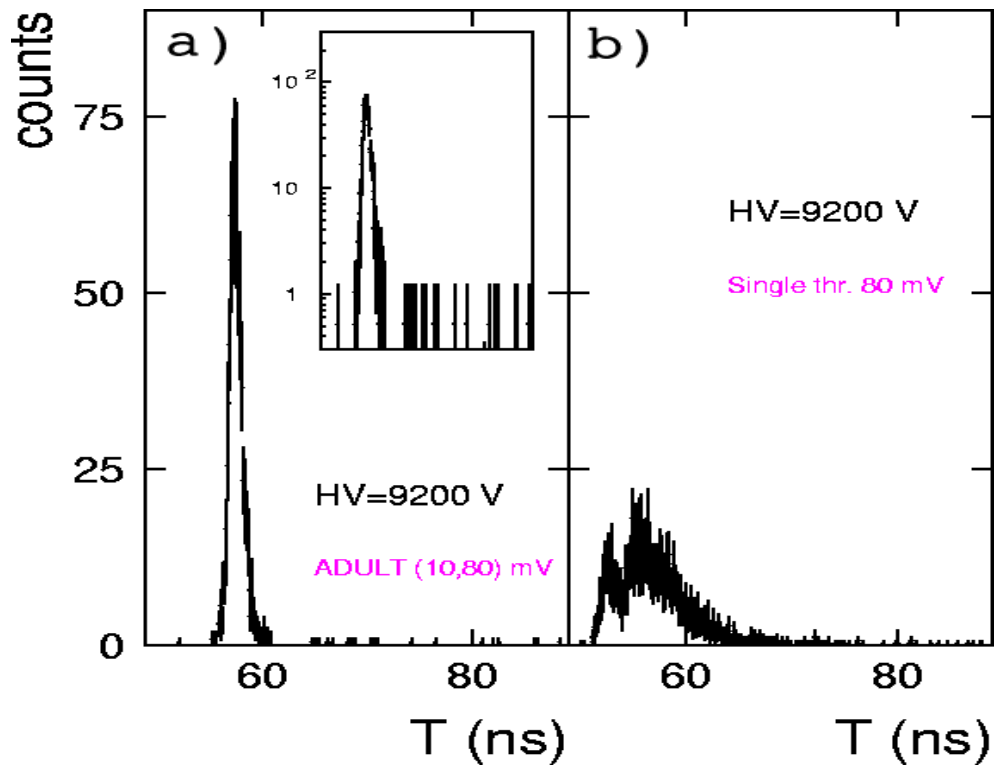
Figure 3.8: Examples of time distributions at 9200 V with ADULT (left part) and with single-threshold discriminators (right part).
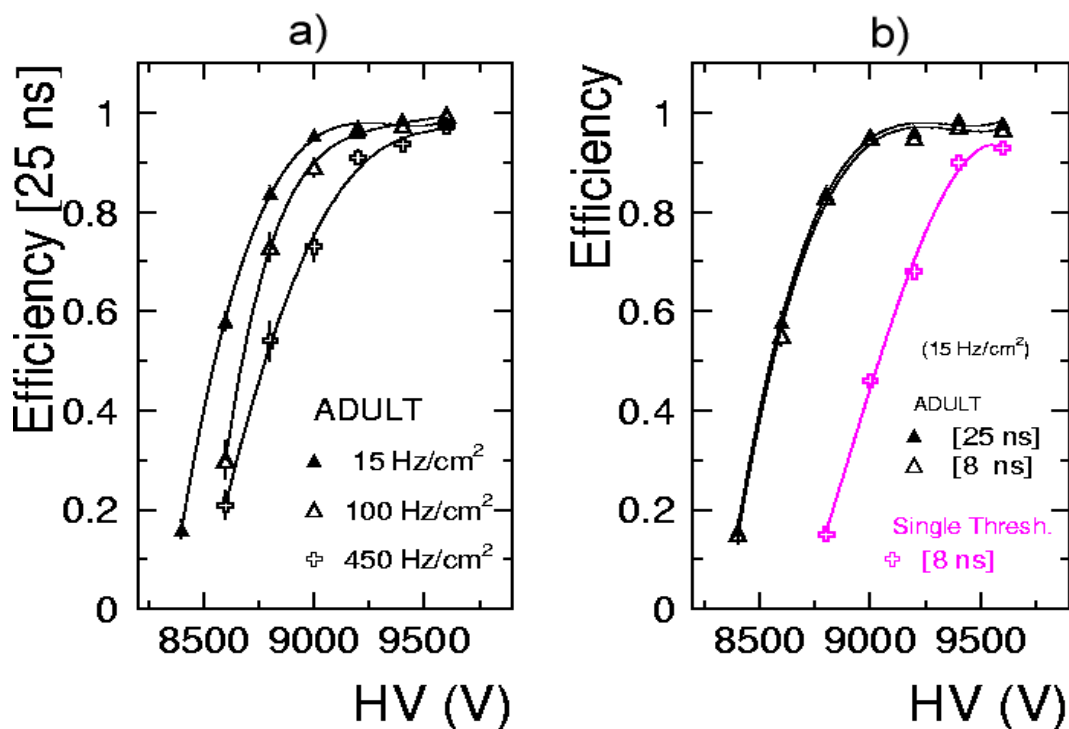
Figure 3.9: Left: efficiency curves in a 25 ns gate with ADULT for three beam fluxes on the RPC. Right: comparisons of the efficiency curves with ADULT in a 25/8 ns gate and in a 8 ns gate with single-threshold discriminators. For the efficiency determination, the position of the time gate (either 25 ns or 8 ns) is optimized for HV = 9600 V and is kept constant for the lower voltages.

this reason, we have analysed in Fig. 3.9, right part, the efficiency curve in a 8 ns gate for the 15 Hz/cm^2 flux. With ADULT, the curve is almost superimposed with the curve in a 25 ns gate. The improvement with ADULT compared to a single-threshold discriminator, for which no efficiency plateau is reached in a 8 ns gate in the voltage range of the picture, is clearly illustrated. The performance achieved with ADULT is due to the fact that this method of discrimination provides a time walk of the TDC peak as a function of the voltage as small as 2 ns/kV.

3.4   The V0 detector

The V0 detector, which was not included in the TDR, has been proposed recently [6] to reject the background events during the p–p data-taking. The design of the detector was guided by simulation results which are presented in this document, together with the geometry of the counter. It is worth noting that no research and development has been done yet and that the design is still quite preliminary; nevertheless the simplicity of the detector should allow p–p physics to start in 2005 (the milestones are given in the last chapter of this addendum).

3.4.1   Background in p–p $\rightarrow 2\mu$+ X reactions

The p–p reactions will be carried out with a maximal luminosity of 10^{31} cm^{-2}s^{-1} (10^6 collisions per second) in the ALICE detector. This luminosity will be obtained with beams at an intensity of $3.5 \cdot 10^{18}$ protons, which corresponds to a p–p nominal luminosity of 10^{34} cm^{-2}s^{-1} in the other LHC experiments. In the case of dimuon physics, the background particles produced by proton–gas interactions far from and close to the ALICE centre [3] will give, in spite of the dimuon trigger algorithm (see Ref. [1]), huge dimuon-like triggers owing to the large 33/38 m^2 planes of the MT1/MT2 trigger chambers. Simulations

Table 3.1: Dimuon-like trigger rates from signal (luminosity of 10^{31} cm^{-2}s^{-1}) and background ($3.5 \cdot 10^{18}$ protons per beam and per second) for two p_t cuts. The background rates are given by any-sign (AS) muons for far and close contributions. The (a), (b), (c), and (d) classes of events correspond to background triggers according to multiplicities and times measured by the V0 counters set at right and left sides of the ALICE vertex.

2μ event type		Rates (Hz) for no cut on p_t		Rates (Hz) for $p_t^{cut} = 1$ GeV/c	
		far	close	far	close
p–gas $\rightarrow 2\mu$ (AS)	any MR	1054	10.0	64	3.0
(a)	MR = 0	1052	0.7	64	0.4
(b)	MR = 1	2	0.7	0	0.4
(c)	MR $\geq$ 2, ML $\neq$ 0	0	8.5	0	2.2
(d)	MR $\geq$ 2, ML = 0	0	0.1	0	0.0
p–p $\rightarrow \mu^+\mu^-$ (OS)	minimum-bias	< 50		< 10	

have been made to evaluate the rates of these background events [6]. The results are given in Table 3.1 and compared with the expected rates from the p–p $\rightarrow 2\mu$ + X reactions for two minimum p_t^{cut} values: 1 GeV/c and 'no cut' (the 'natural' p_t^{cut} of the dimuon trigger).

The contribution of background from any-sign (AS) dimuons is about one or two orders of magnitude larger than the opposite-sign (OS) dimuon triggers given by the physics and according to the p_t^{cut} value. In order to collect more information on these background events and, consequently, to eliminate them from the data acquisition (online action) and from the event analysis (offline action), a V0R device will be set in front of the absorber. This device will hermetically cover the largest possible part of the dimuon spectrometer acceptance (η = 2.5–4) and will be made of several elementary cells. Each of them should allow a separation of the signal given by one MIP (Minimum Ionizing Particle) from the signal given by two or more MIPs and it should provide a time resolution of the order of a few hundred picoseconds. The detector will give the information MR (MR = 0 and MR $\neq$ 0 will be obtained online) and TR, which will represent the number and the time of firing particles, respectively. This device will work in conjunction with a large V0L device set in the opposite direction relative to the vertex. It will similarly measure ML and TL information. Several very useful indicators will be collected to identify the origin of the vertex. The simulated results are given in Table 3.1. They are given under four classes (a), (b), (c), and (d), according to the MR, ML, TR, and TL values.

We observe that the main part of the background can be recognized and eliminated with the help of the V0 device. The class (a) and (b) events do not correspond to physical events for which a MR value is expected to be at least 2. They will be eliminated either online (a) or offline (b). The class (c) events provide the vertex of the collision through the TR–TL measurement. Any vertex outside the vertex diamond will correspond to background. The simulations show that all these background events are effectively originating from that zone. This filter will thus kill all of them. Lastly, the class (d) events give information from the V0R array alone. In this case, when the fired cell localization does not coincide with the cells crossed by the reconstructed muons, this indicates the presence of background. As a consequence of these event selections, the V0 device, which validates the dimuon trigger, will allow events to be recorded without restrictions on the p_t values and on the final state of the reaction symbolized by X. The data will then be collected in the most extended minimum-bias conditions.

3.4.2 Description of the detector

The V0R array is the most important for the dimuon trigger control. We will concentrate our efforts on this device. The V0L array must be large for a good efficiency [6]. It could be similar to the V0R array or it could be supplied by the T0L device [8], although the former presently covers a more limited
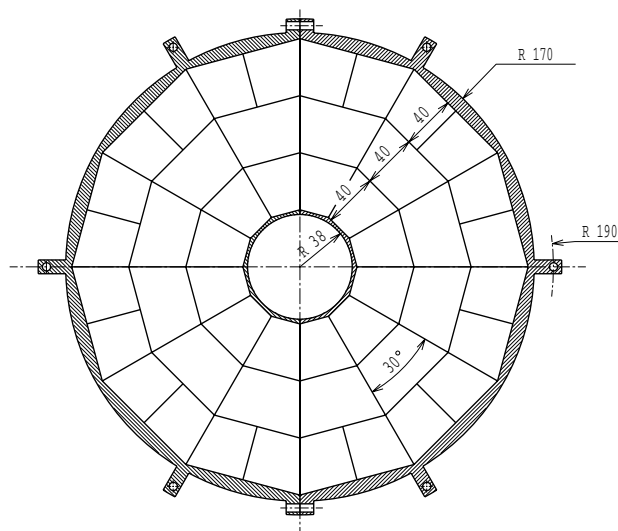
Figure 3.10: V0R detector: front view of the 48 elementary cells inserted in their box.

pseudorapidity range.

A front view of the V0R detector is shown in Fig. 3.10. It is made of 48 elementary counters distributed inside 12 sectors of 30° in aperture for an azimuthal symmetry. They are inserted within two half-boxes bound to each other and fixed on the front absorber. The resulting cylindrical box does not exceed 4 cm in thickness. It covers the carbon section of the absorber from R_{min} = 40 mm to R_{max} = 160 mm. Four cells of scintillator counters (about 40 mm in length, see Fig. 3.10) cover each sector in such a way that similar time resolution and charge 1 and 2 separation would be achieved. These are the main requirements for the background signature in p–p physics. Beside this essential purpose, the V0R array is proposed as a rough charged particle multiplicity detector within the spectrometer acceptance. From this information, which should be provided both in p–p and in ion–ion physics, a minimum-bias trigger could be derived.

The elementary counters will be made of polystyrene scintillator read out by wavelength shifting fibres. The light will be transported a few metres away by one clear fibre. Development of this technique was done in the framework of other experiments (see for example Refs. [9], [10], [11], [12]). It will be a useful starting point for defining our specific system. At the end of the clear fibre the light is converted into a charge signal by a photomultiplier. Such a signal is split in two components according to the ratio 95/5. The 'pp' channel, with 95% of the signal, will be optimized for the p–p physics and the low-multiplicity conditions in A–A reactions. This channel could be adjusted so that each cell would allow to record a signal from one MIP to about 25 MIPs. The 'AA' channel, with 5% of the signal, will be dedicated to the high-multiplicity production in A–A reactions. As an example, the Pb–Pb reactions will produce a maximum of 12 000 charged particles within the η range covered by the V0R array. That corresponds to about 450, 250, and 100 MIPs through each cell of the first, second, and third rings of the array, respectively. If the gain of each AA channel is adjusted so that a dynamics of 25 is obtained, the minimum signal will correspond to 18, 10 and 4 MIPs, respectively. This AA channel, coupled to the pp channel which covers the range 1–25 MIPs, will allow the full dynamics encountered in Pb–Pb collisions to be covered, which can be performed for any other ion–ion reaction.

A very simplified electronic sketch is shown in Fig. 3.11. Each channel will include a voltage divider (PM), a fast amplifier (FA), a fast gate (FG), a constant fraction discriminator (CFD), time (TDC) and charge (ADC) to digital converters. A majority circuit (MLU) on the pp channel will give the information MR to be used for an online V0R validation of the trigger. The electronics signals will be shorter than 25 ns and all the electronics circuits will have a dead time smaller than 20 ns.
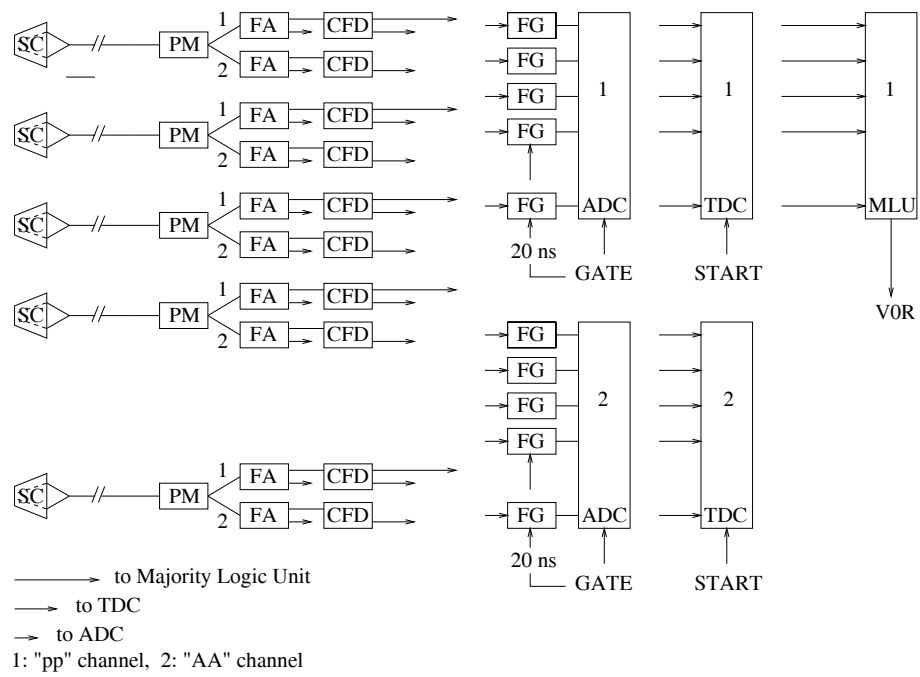
Figure 3.11: Schematic layout of the V0R front-end electronics.

4 Geometry monitoring

4.1 Introduction

The requirements for the monitoring of the muon-arm geometry, i.e., the relative positions of the tracking chambers, are specified in the TP [2] and TDR [1] on the basis of the multipoint optical Geometry Monitoring System (GMS). The GMS performance has been evaluated in Ref. [1] as a function of the positioning tolerances of the chambers and optical elements (laser beam collimators and beam position sensors). The optical method has been shown to be well suited for determining the relative positions of the tracking chamber with the required precision. In this report, we present the conceptual design of the GMS.

4.2 Basic modules to be monitored

The aim of the GMS is to measure the deformations and the relative displacements of Rigid Modules (RM) constituting the Tracking System (TS). A RM moves in space as a rigid body and undergoes only homogeneous (thermal) deformations. It is worth recalling that a chamber (half-chamber) stands for the full detection plane (half detection plane) of a tracking station with its frame and is made of elements which are called detectors. A station is composed of two chambers or four half-chambers. The TS consists of the following RMs, subject to monitoring.

- The chambers of Stations 1 and 2 (TC1 to TC4). They are made of four detectors (quadrants) which are strongly bound to each other by their frame. The four detector planes are parallel. The possible homogeneous deformations of the chambers are supposed to be exclusively along their planes (in-plane deformations). No deformation normal to the chamber planes is foreseen. The monitoring will give information on the in-plane deformations added to the displacements of the chambers in space.

- The half-chambers of the Stations 3, 4 and 5 (TC5 to TC10). These RMs are made of slat detectors maintained parallel within a common frame. The carbon fibre material used for the slats and the frames results in a very weak thermal expansion. The chambers of Station 3 are made of two rigidly tied half-chambers, so there is no relative movement of the half-chambers in any direction. These chambers are thus two RMs. Lastly, the chambers of Stations 4 and 5 are made of two rigid half-chambers which are fixed to each other only along the central vertical direction.

4.3 Multipoint monitoring system

The geometry of the chambers and the surrounding mechanical elements of the TS defines the following monitoring scheme. The positions of the RMs are measured with respect to the laser beams crossing consecutively the semi-transparent 2D sensors fixed on the RMs themselves. The system of laser beams forms the monitoring reference frame. Its position in the overall ALICE coordinate frame will be permanently controlled by monitoring the positions of the laser collimators with respect to the benchmarks placed in the ALICE hall.

The semi-open design of the full system is represented in Fig. 4.1. Beside a part of the TPC volume, the different mechanical elements of the spectrometer are shown. The chambers of Stations 1 and 2 are
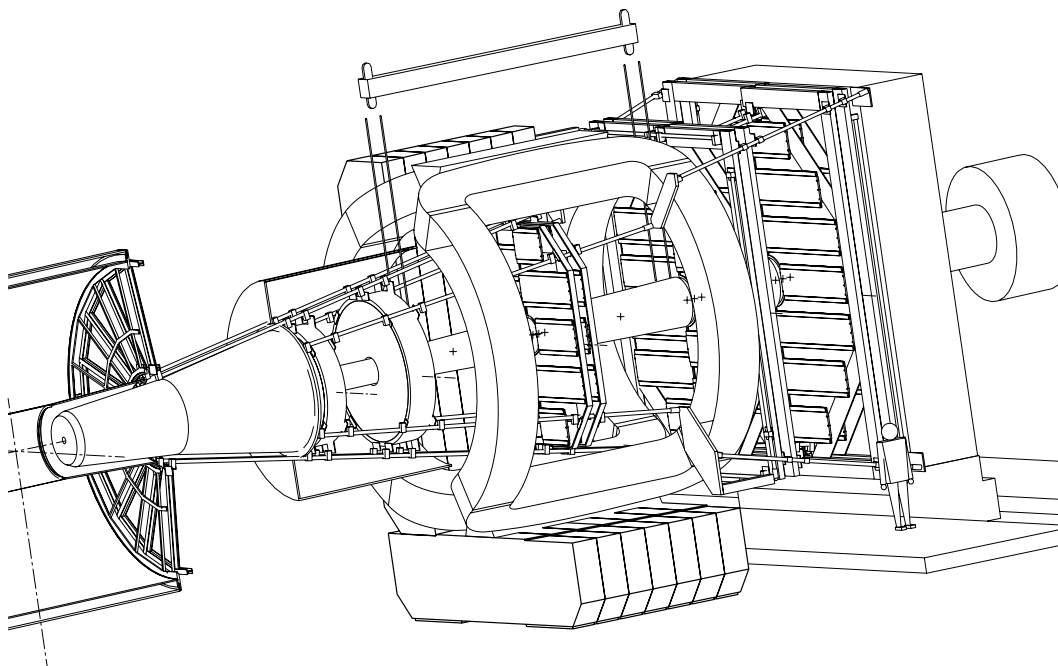
Figure 4.1: Conceptual design of the multipoint projective monitoring system.

perpendicular to the beam direction (tilted by $0.794°$ with respect to the horizontal plane), as are the front absorber and the beam shield. The chambers of Stations 3 to 5 are vertical, like the muon filter.

Except for the vertical and horizontal lines, the laser beams cross optical sensors in the downstream $\rightarrow$ upstream direction relative to the spectrometer. Each laser beam is surrounded by aluminium tubes, up to 60 mm in diameter. These tubes serve as a shield against the air temperature gradient, a barrier for any mechanical obstruction and a physical protection from the invisible laser line. Laser collimated sources have to be set on the most stable elements of the spectrometer. The muon filter and the dipole yoke seems to fulfil this condition. A detailed analysis of their stability (low and high frequency vibrations) is under way. Optical sensors are set on the frames of the chambers. All optical elements and their supports are outside the spectrometer acceptance.

Before describing the GMS in more detail, it is useful to recall that the different coordinates quoted below are in a reference system where the origin corresponds to the interaction point and the axes are defined by the beam direction (z axis) and the two perpendicular directions: horizontal (x axis) and 'vertical' (y axis). The (x ,z) plane is tilted by $0.794°$ with respect to the horizontal plane.

The GMS consists of three parts.

- The first part includes four laser beams passing through the full system. These beams are set in parallel vertical planes on both sides of the vertical median plane. The laser collimators are fixed on the muon filter. Each beam crosses ten sensors up to an eleventh one fixed on the TPC frame. The latter is used as a reference and for relative monitoring with respect to the central ALICE tracking detectors. For instance, the direction of one of these beams is given by the coordinates $x = 200$ mm, $y = 230$ mm at $z = 0$ and $x = 200$ mm, $y = 2749$ mm at $z = 14,660$ mm. Each optical beam forms an angle $\theta_y = 9.75°$ with the (x ,z) plane.

- The second part of the GMS includes four chains of laser beams lying in the planes at $\phi = \pm 45°$ and $\phi = \pm 135°$ in azimuth around the z axis. They cross the TS in two steps. For each chain, the first

step consists of a laser beam crossing four sensors fixed on the chamber frames of Stations 5 and 4 and the second consists of a beam crossing six sensors mounted on the chambers of Stations 3, 2 and 1. The first-step beam is emitted by a laser collimator set on the muon filter. The second-step beam is emitted by a collimator set on a support fixed to the yoke of the dipole. The relative monitoring of these two segments is provided by sensors fixed on the intermediate supports and crossed by the first-step laser beams. For one of these chains, the laser beam is directed along a line coming from the position $x = 0$, $y = 0$ and $z = 2464$ mm at a polar angle $\theta = 19.7°$ for the first step, and along a line coming from the position $x = 0$, $y = 0$ and $z = -739$ mm, with polar angle $\theta = 10°$ for the second step. Each chain can be deduced from the previous one by a rotation of $\pm 90°$ around the z axis.
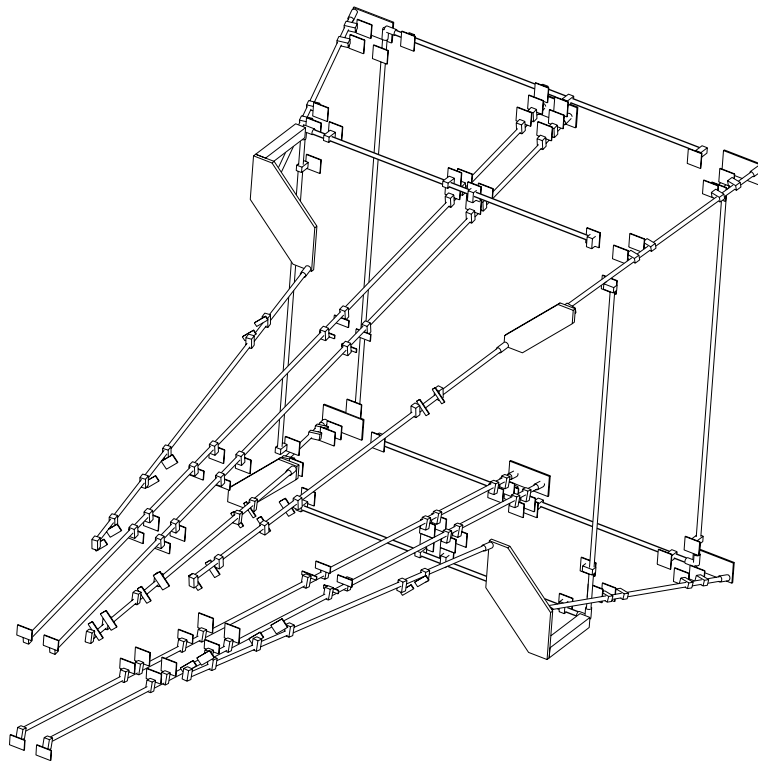
- In addition to the eight laser beam chains described above, the muon filter and two intermediate supports are equipped with laser collimators emitting vertical and horizontal beams. These beams are monitored by sensors set on the vertical and horizontal external frames of half-chambers 10 (Station 5) and 7 (Station 4), half-chambers which are mechanically tied to the half-chambers 9 and 8, respectively. This monitoring will give additional constraints for a better determination of the position of the largest stations.

The laser system alone is shown in Fig. 4.2. The laser collimators and the sensors are clearly shown, as are the pipes shielding the beams. The system for the control of this laser beam network is not shown in this figure. Mechanical support of each optical element will be defined by taking into account their localization in the system. The possibility of (x, y) and (θ, ϕ) adjustments for the laser collimators and (x, y) adjustment for the sensors will be included in their individual supports. At least 20 laser collimators and 100 sensors are necessary for this monitoring system.
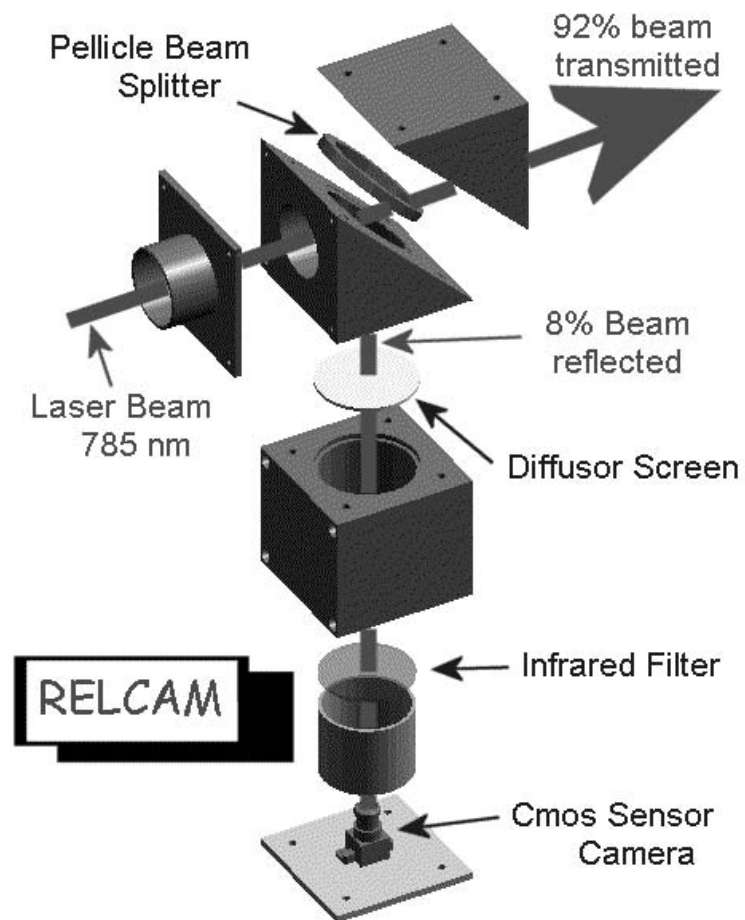
4.4   The optical monitor RELCAM

The ALMY and RASNIK systems described in the TDR [1] will no longer be considered as sensors for the GMS. The RELMY sensor is described in Refs. [1, 5]; we present here the RELCAM sensor which is derived from it. A pellicle beam splitter 2 μm thick is inclined at 45° with respect to the light beam and reflects less than 10% of the light on a screen diffuser where the picture of the spot is formed. This picture is monitored by a miniature camera of dimensions 17 mm x 17 mm x 30 mm, including the lens. This single-chip monochrome camera is equipped with a CMOS (1/3 inch) sensor composed of 628×582 pixels and provides a standard CCIR video signal. The sensor has a dynamic range greater than 72 db, a signal/noise ratio larger than 48 db and, and a sensitivity smaller than 0.5 lux. It provides an efficient spectral response centred at 785 nm, which corresponds to the laser wave-length. A long pass filter with cut at 715 nm (SCHOTT RG715) is set on the reflected beam in front of the camera lens in order to cut the visible spectrum. A sketch of the sensor used for tests is shown in Fig. 4.3. No scale is given for this layout because the final geometry of the device will be defined after the laboratory tests at present under way.

Each beam source consists of a 785 nm laser diode coupled with a single-mode fibre and provides a circular beam cone. Its intensity distribution is Gaussian and has a small coherence length to reduce the speckle contrast. At the end of the single mode fibre, a focusable collimator is used to obtain a beam with a median diameter of 4.5 mm at 10 m and a divergence of 0.12 mrad. The RELCAM sensor is mounted on two–axis motorized translation stages. The video signal is digitized by an industrial frame grabber in an 8-bit (per pixel) matrix and then transferred (in units of four pixels, corresponding to 32-bit words) to the memory of a computer. A simple analysis of the picture is obtained by thresholding the amplitude (to eliminate the residual noise on the whole surface of the sensor) and summing the pixel signals in the x and y directions. The beam coordinates are given by the centres of gravity of the x and y distributions. The two translation stages (100 mm in range) have a resolution of 0.5 μm and a reproducibility of 1.5 μm.

Figure 4.2: Layout of the laser system for the monitoring of the tracking chambers.

Pellicle Beam Splitter

92% beam transmitted

Laser Beam 785 nm

8% Beam reflected

Diffusor Screen

RELCAM

Infrared Filter

Cmos Sensor Camera

Figure 4.3: Schematic design of the RELCAM sensor used for tests.
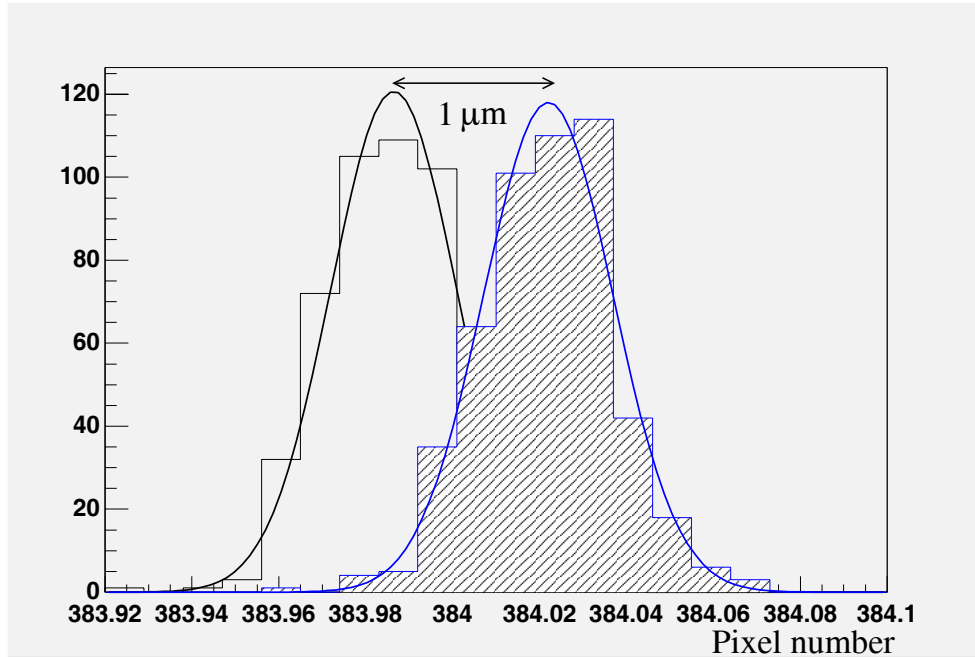
Figure 4.4: Centre-of-gravity distributions of the laser beam measured by the CMOS camera used in RELCAM for two beam positions 1 μm apart.

Their scan movements and the data acquisition are controlled by a computer. Fig. 4.4 shows the centre-of-gravity distributions of the laser beam recorded by the CMOS camera for two beam positions 1 μm apart. The achieved resolution is about 1 μm. Extensive tests (on a test bench) for fully evaluating the performances of this device are in progress. The final choice of the sensor type (RELMY or RELCAM) will be taken after comparative studies.

The specifications of RELCAM can be summarized as follows:

- high transmittance (>90%), no beam deviation, no second surface reflection;

- good space resolution because of the large number of small size pixels (628 × 582);

- large dynamic range and sensitivity;

- good intrinsic radiation resistance of the CMOS sensor;

- no electronics circuit near the sensor;

- simple readout by multiplexing the video outputs of the large number of sensors (of the order of 100) to the frame grabber.

4.5   Conclusions

The monitoring of the tracking chambers of the ALICE dimuon spectrometer is possible by optical methods. A sensor based on the principle of the measurement of reflected light seems to be fully adapted to the requirements for this control.

5 Dipole magnet

5.1 Introduction

Following the publication of the ALICE muon arm TDR [1] in August 1999, a manufacturing design contract [2] was concluded with JINR in November of that year. In July 2000 the deliverables of this contract were submitted for a Production Readiness Review (PRR) [3]. The conclusions of the review panel were summarized in a memorandum [4] addressed to the ALICE Management.

The ALICE Collaboration has subsequently endorsed the request from the Dimuon Arm Collaboration to separate the manufacturing of the dipole magnet coils from the construction of the iron yoke. The decision was therefore taken to proceed with a public call for tender for the excitation coil system of the dipole magnet. The consequences for the organization of the magnet project and the time schedule are explained.

5.1.1 Scope of the project

In order to allow better planning and follow-up the project has been reorganized. The production and supply of the two excitation coils are subject to a public call for tender and will lead to a manufacturing contract with the industry. The remaining items have been separated into smaller sub-projects, which are activity specific. We expect to identify clearly the required resources and competences with this structure. The design completion stage will include the following:

- final manufacturing specification and drawings for the iron yoke,

- final design and manufacturing drawings for the coil supports,

- design of the magnet base frame.

The production stage will then follow the same partitioning.

5.1.2 General description

The conceptual design of the magnet has been presented in the TDR [1]. Whilst the global concept and parameters have not been modified, the design has now been worked out in detail. In this chapter we will describe developments, design improvements and modifications which affect the construction and performance of the magnet. The main characteristics and parameters of the magnet are shown in Table 5.1, which replaces Table 5.1 of the TDR.

5.2 Iron yoke

The design of the flux-return yoke has been finalized. It is still proposed to adapt the existing steel stacks in Dubna to the dimensional requirements for the magnet. In order to decrease the saturation in parts of the yoke and to simplify the geometry, the outer perimeter now has a cubic shape (Fig. 5.1). As a result the inner longitudinal sides of the vertical pole blocks will need to be machined to obtain the $9°$ angle of the acceptance cone. This also requires some additional iron for the upstream modules of the wedge-shaped poles (Fig. 5.2).

Table 5.1: Dipole magnet main characteristics.

	Item	Unit	Value
1	**Magnetic characteristics**		
1.1	Nominal magnetic field	T	0.70
1.2	Field integral ($z = 0$–14.4 m, $\theta = 0°$–$9°$)	Tm	3.0
2	**Electric characteristics**		
2.1	Ampere-turns	MA	1.968
2.2	Operating current	kA	5.856
2.3	Winding resistance ($40°$)	Ohm	0.101
2.4	Power dissipation	MW	3.46
3	**Winding**		
3.1	Aperture diameter	m	4.078
3.2	Overall magnet length	m	4.97
3.3	Coil cross-section	m^2	0.490
3.4	Conductor weight	tons	37.4
3.5	Conductor length	km	6.87
3.6	Number of pancakes per coil		12
3.7	Number of turns per pancake		14
3.8	Number of turns per coil		168
4	**Conductor**		
4.1	Material		E-Al-99.7
4.2	Conductor cross-section	mm^2	50.5×50.5
4.3	Channel diameter	mm	26
4.4	Radius of edges	mm	3
4.5	Al cross-section	mm^2	2011
5	**Cooling**		
5.1	Water temp. rise per cooling circuit	$°$C	30
5.2	Cooling water flow rate	L/s	29.8
5.3	Cooling water pressure drop	Bar	10.9
6	**Magnet yoke**		
6.1	Material		Equiv. EN S235JRG (St. 37-2)
6.2	Free gap between poles	m	2.883–3.870
6.3	Inner height	m	6.020
6.4	Outer dimensions (L$\times$W$\times$H)	m	$3.115 \times 5.977 \times 8.840$
6.5	Weight	tons	785
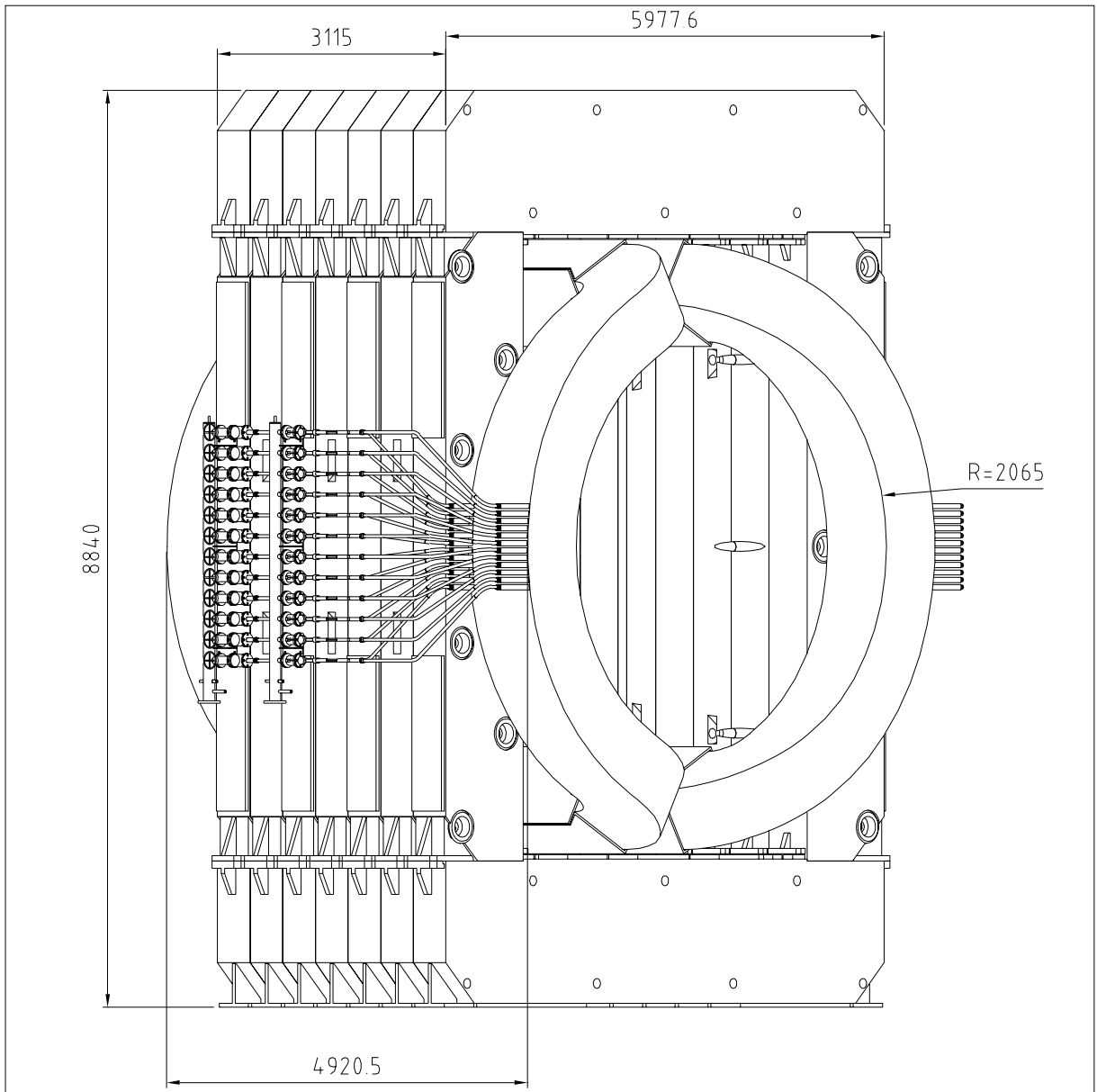
Figure 5.1: Dipole assembly.
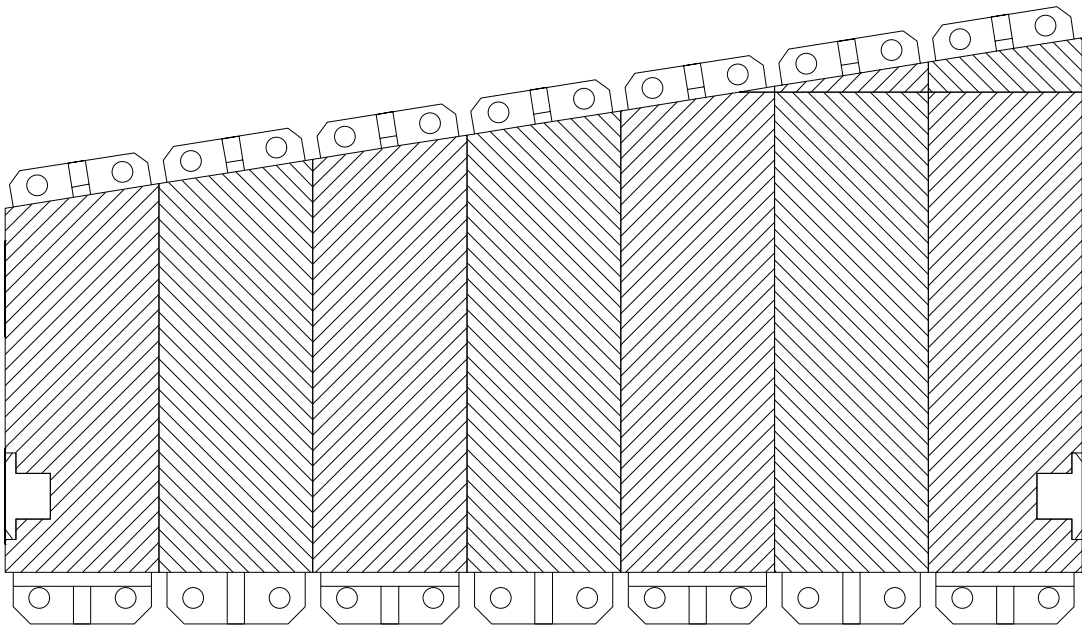
Figure 5.2: Pole structure cross-section.
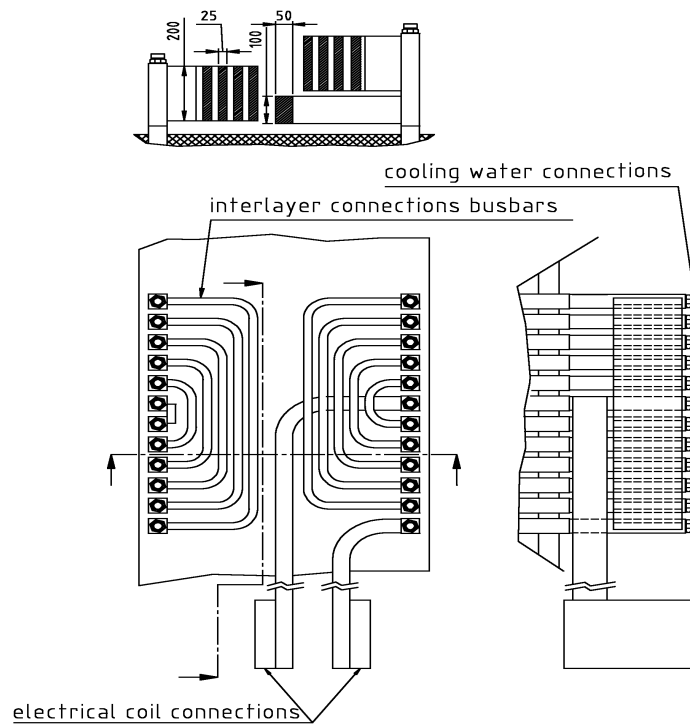
Figure 5.3: Electrical interlayer connection scheme.

5.3   Coil

The concept of the coil construction has been mantained. However, as a result of optimization, the conductor cross-section and number of turns per coil have been adapted. This leads to a lower supply current whilst increasing the total voltage drop. The power dissipation of the magnet is only marginally affected.

A redesign of the electrical and cooling water connections appeared to be necessary in order to limit the power losses in the air-cooled interlayer busbars and to obtain a simple connection scheme (see Fig. 5.3) The new design avoids crossing of busbars and thus allows all the connectors to be placed on a single level. The electrical circuit diagram (Fig. 5.4) required, however, a modification of the pancake winding scheme. The interlayer connections are now alternately situated on the outer and inner perimeter of the coil. Consequently, the pancakes have to be wound alternating clockwise and counterclockwise.

5.3.1   Electrical insulation of the coil

The proposed insulation technique was based on prepreg fibreglass tape. This method was considered adequate and conforms to the technical possibilities of the Dubna team. The technique is, however, still not frequently used for comparable magnets in industry. Following the decision to issue a public call for tender, it has also become necessary to review the insulation method. Current insulation technology is based on fibreglass tape wrapping and subsequent vacuum impregnation. This procedure has been foreseen for the insulation of the LHCb dipole coils [5], which are of similar size and shape to the ALICE dipole coils. The application of this technology to the ALICE dipole coils will depend on the selected coil manufacturer.
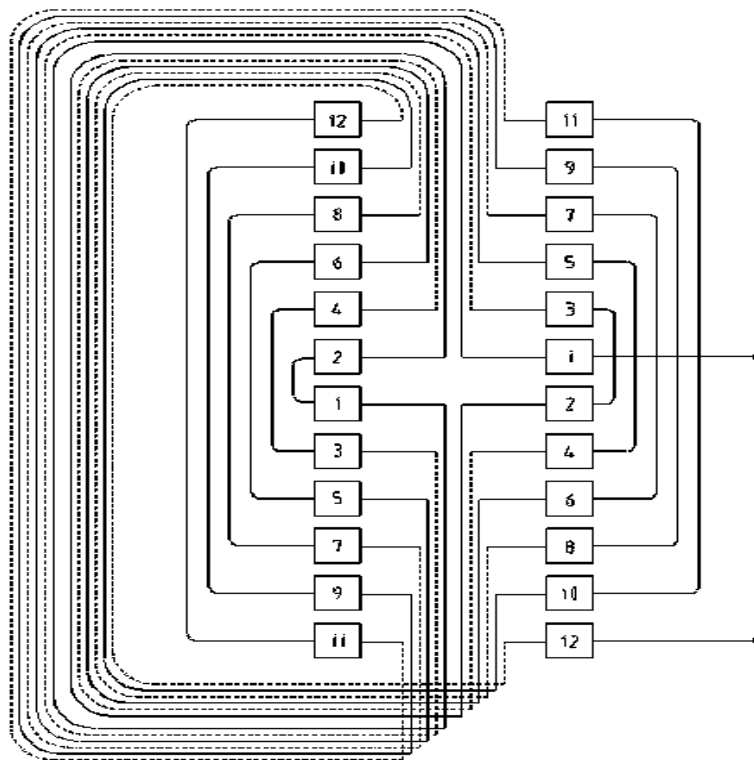
Figure 5.4: Electrical circuit diagram.

5.3.2   Tooling and technology of the coil manufacture

The excitation coils will be assembled from single-layer pancakes. The pancakes will first be wound to racetrack shape on a flat winding mandrel. In the case of vacuum impregnation the conductor insulation can be taped after the flat winding of a pancake. It is therefore possible to trim the conductor cross-section after bending in order to eliminate the deformation caused by the keystone effect. The widths of the flat pancakes will not be identical but will increase from the innermost to the outermost layer. After forming of the saddle-shape coil ends this will result in a rectangular cross-section of the coil. Before the shaping operation the interlayer insulation will already be applied to the pancakes. The greater than 2 m bending radius for the saddle-type coil ends will not cause a noticeable keystone effect. In fact it should be borne in mind that the conductor will be delivered on reels with only half that radius. The rather large cross-section dimensions of the coils make a unique vacuum impregnation of all pancakes in order to obtain a monolithic structure quite complicated and risky. When using this technology it is therefore proposed to partition the coils into several sub-assemblies of three to four pancakes, which will then have to be consolidated by mechanical fixtures.

5.4   Test assembly of the dipole magnet

Following the decision to separate the production of coils and yoke a complete assembly of the magnet at the factory is no longer planned. The first power tests of the magnet will consequently take place in the surface hall SXL2 of the ALICE site where the magnet will be assembled in the frame of the ALICE preassembly programme. However, this does not preclude the foreseen electrical tests of the coils at the production site, nor a preliminary assembly of the yoke at the manufacturer's premises to proceed with all mechanical tests and adjustments.

Table 5.2: Magnet monitoring parameters.

Name	Number	Description
ES	1....n	Emergency stop
MSS-INT	2	Status of MSS output
LS01-LS24; LS101-LS124	48	Status of valves (closed or not closed)
LS201-LS208	8	Status of electrovalves (open/close)
Open V1 - Close V4	8	Manual electrovalves command
Layer temperture, water leak	3	Information on the MSS input
AP201-AP204	4	Pressure of water in the manifold
AT201-AT204	4	Temperature of water in the manifold
DCCT	1	Current on the dipole
Hall probes	1	Hall on the dipole
AT01-AT24	24	Temperature on the different layers
AF01-AF24	24	Flow on each outlet
MCS-Interlock	2	Command of the dipole power supply
I-Setting	1	Setting of the current
Valves-Command	1	Close/open electrovalves

5.5 Magnet base

Several important changes have been adopted for the installation procedure of the barrel detectors. As a consequence, a displacement of the dipole magnet after installation will no longer be required. A reinforced concrete foundation is foreseen instead, on which the magnet will be installed with an intermediate steel base-frame structure to allow the necessary alignment.

5.6 Magnet control

The EP-EOS group has the mandate to propose a control system for each of the spectrometer magnets of the LHC experiments. The control system for the dipole magnet will follow these standards (Fig. 5.5). The Magnet Control System (MCS) will provide the remote control of the operation. All changes of magnet settings will be handled through this system. The safety of the installation will be maintained by the Magnet Safety System (MSS), which is a part of the MCS. The essential functions will be the monitoring of temperatures, pressure and flow in the coil cooling circuits and electrical fault conditions of the magnet and power supply. A list of the monitored parameters is given in Table 5.2.

5.7 Calculations

Substantial effort has been invested in design verification with finite-element computer programs, i.e. ANSYS and TOSCA. The magnetic field values have been updated to include the design changes. The stresses induced by mechanical, magnetic and thermal forces acting on the coils and yoke have been determined.

5.7.1 Magnetic field

The complete magnet system of ALICE including L3, the dipole magnet and the muon filter has been modelled in order to predict the bending field integral and the saturation effects in the steel parts. The mapping of isolines of the flux density integral (see Fig. 5.6) shows a slight asymmetry caused by the
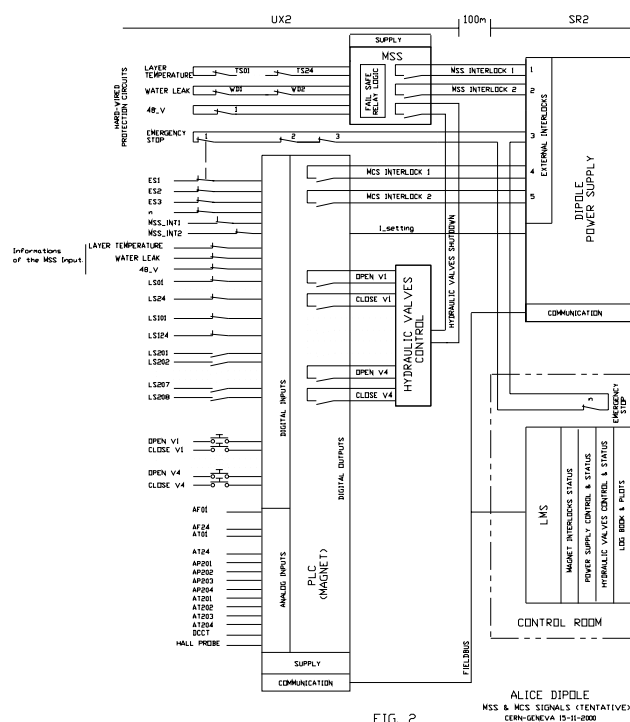
Figure 5.5: Magnet control principles.

Table 5.3: Electromagnetic forces.

	Dipole yoke	Dipole coil	L3 door 1	L3 door 2 (dimuon side)	Muon filter
F_x (kN)	−359	354	58.2	108	2.4
F_y (kN)	9	−3	272	515	0.1
F_z (kN)	−2716	111.2	7118	−4274	−20

contribution of the L3 magnet. This effect is, however, not linear. It will strongly depend on the excitation of each of the magnets. Consequently, it will be mandatory to measure the magnetic field for all planned operation conditions of the two magnets.

5.7.2   Electromagnetic forces

As a consequence of the design modifications of the dipole magnet, but also of the inserts in the L3 doors, it is necessary to review the electromagnetic forces exerted on the mechanical structures of the complete ALICE magnet system. It can be seen from Table 5.3 that the magnitude of the main force vectors remains similar to the values of the TDR, below the mass of the system components.

5.7.3   Stray field

The fringe fields present on either end of the dipole magnet contribute to the integral of the bending field. Figure 5.7 shows a plot of the flux density. The derivative at the upstream side is considerably stronger than at the downstream side of the magnet owing to the proximity of the L3 pole caps, which causes a strong magnetic coupling. The stray-field values calculated for the volume surrounding the dipole magnet are below 30 mT at distances beyond 1 m.
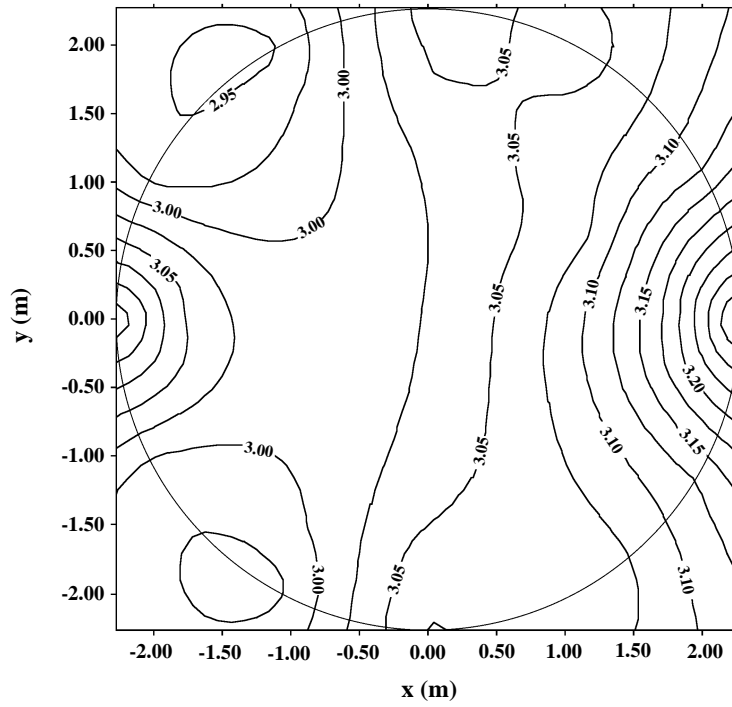
Figure 5.6: Isoline map of the integral (along *z*) of the bending field .
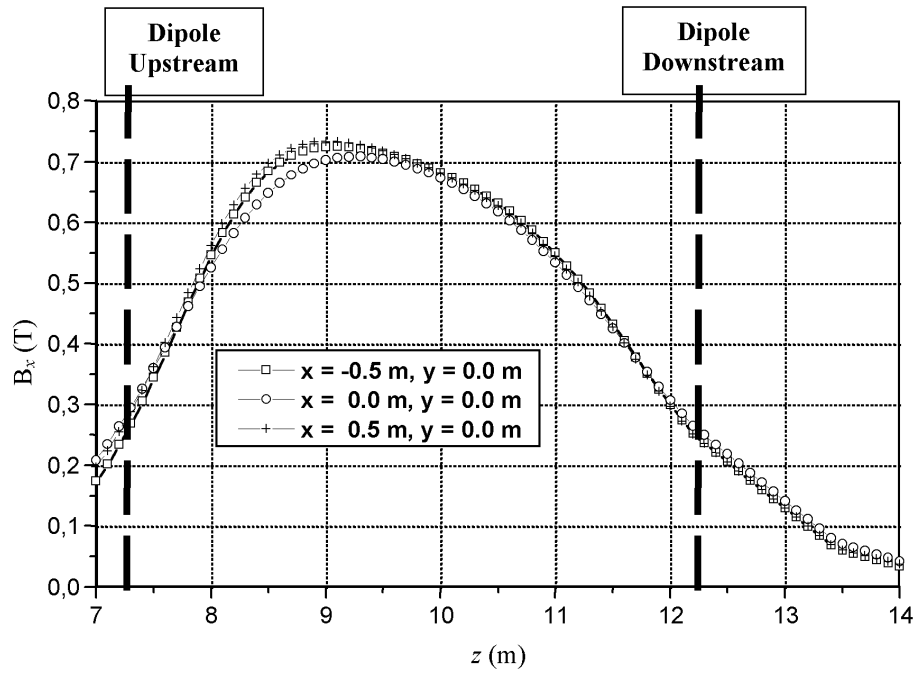
Figure 5.7: Flux density B*x*.

Table 5.4: Mechanical stresses on the conductor.

Location	Stress(Mpa)	Origin
P1(Coil suspension boundary)	18	EMF + gravity
P2(Max. deformation)	31	Thermal expansion
Elsewhere	< 25	EMF + thermal
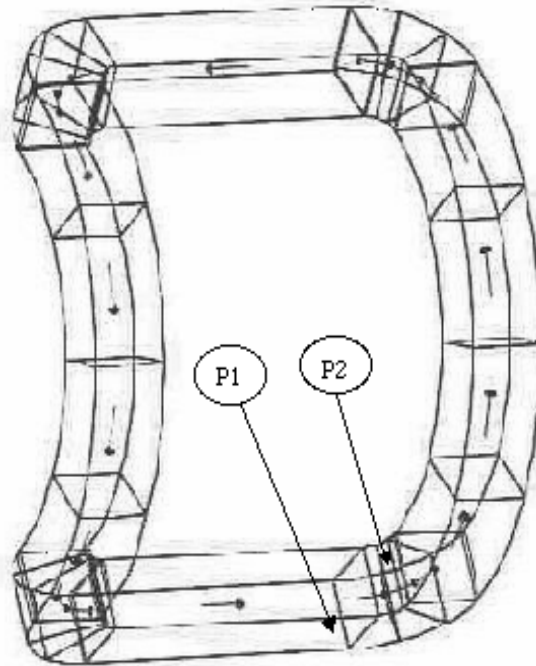
Figure 5.8: Regions of the coil where the peak stresses are located.

5.7.4 Mechanical structure

The mechanical properties of conductor and insulation material have been investigated in a number of experimental studies [6], [7]. Different models have been elaborated in order to predict the temperature-induced stresses, which depend strongly on the selected boundary conditions. The magnetic forces have been extracted from TOSCA calculations. The left / right asymmetry due to the L3 magnet has been taken into account. The stress / strain resulting from the forces acting on the most solicited coil have been calculated with ANSYS. The values for the regions of highest stress are summarized in Table 5.4. Peak stresses are located in very restricted areas (shown in Fig. 5.8), i.e. the boundaries of coil clamping (P1) and the region where the deformation due to thermal expansion is maximum (P2). These singularities are not considered representative in view of their small size. In addition the ANSYS code (used to compute the thermal load) does not allow 2D deformations and can therefore be considered as the worst case. In all other regions the resulting loads are well below the yield strenght of the conductor material. Loads from thermal expansion dominate the combined stress values. The results have been cross-checked with the calculations already performed for the LHCb dipole magnet. It can be concluded that the expected stresses will be within the allowable range for the proposed conductor material. However, the design of the coil clamping system will be refined in order to obtain a more balanced load sharing.

5.8 Organization

No delay in the termination date is foreseen since all subsystems can be produced independently in parallel. However, since the initially planned full assembly and test of the magnet at the manufacturer's site can no longer be maintained, the assembly and precommissioning of the magnet in the SX surface building at Point 2 becomes even more important and has, therefore, been extended in time. As a consequence of the separation between the coil and the yoke manufacture, the organization of the ALICE dipole project has been adapted. CERN has agreed to take on the overall project management. In order to dispose of the necessary resources a closer collaboration between the teams in charge of the LHCb magnet and the ALICE dipole magnet has been organized.

5.9 Prototyping and tests

Considerable prototype and test activities were undertaken in parallel during the production of the manufacturing design documents. At JINR extensive testing of the mechanical and electrical characteristics of conductor and insulation material was carried out. In addition JINR produced a full-scale prototype pancake with a reduced number of turns and length. This winding was produced with 12 m long bars of UA1 conductor previously supplied by CERN. In order to obtain a single conductor length the pieces were welded together before winding the flat layer. The conductor was then insulated with prepreg fibreglass tape from a qualified Russian supplier. A prototype construction was used to shape the saddle-type pancake ends. Subsequently the layer was pressed to the final dimensions and polymerized by feeding a d.c. current through the conductor. The finished pancake was subjected to dimensional checks and electrical tests [8].

A number of different bending tests with short conductor samples were carried out at CERN to assess spring-back effect, compensation of keystone effect and behaviour of insulation material during the bending operation [9]. The largest observed cross-sectional deformation of the conductor lies within $\pm$ 1.8 mm. A mechanical correction will therefore be required in these locations since it exceeds the range of compensation through the insulation material alone. The production of the prototype pancake showed that the conductor insulation tape could be wrapped before winding the flat layer. The concept involving the shaping of the coil ends and the use of direct electrical heating to polymerize the prepreg insulation material could be demonstrated. Additional prototyping work is, however, required to guarantee a better control of the homogeneity of the insulation and the dimensional tolerances. The procedure to shape and assemble individual pancakes into a coil is being reviewed. To this end a 1:10 scale magnet model has been produced at CERN.

6   Physics performance

6.1   Introduction

A lot of work has been done on the simulations and the reconstruction software of the dimuon arm. The simulations of the front absorber and the beam shield, performed with as much detail as possible, led to a very good understanding of the background in the detectors. Furthermore the tracking program has been totally rewritten to include it in the general framework of ALICE. Several optimizations were then possible. The most important one is the replacement of some tungsten by lead. This change does not decrease the quality of the beam shield but some substantial savings are made.

Compared to the TDR (Ref. [1]) the acceptance of the tracking chambers has been improved dramatically, especially close to the beam pipe. This improves of course the total efficiency, but a lot of software work is still to be done for the events close to the beam pipe where the background is the highest.

6.2   Hit densities

The main difference with respect to the background simulations given in the TDR (Section 7.5) is the integration of the vacuum chamber. This chamber is quite complicated and presents a lot of dips and spaces. It is equipped with a 1300 W/m^2 heating jacket for the bake-out which should be done once a year at 300°C.

Figure 6.1 shows a side view of the front absorber and the beam shield. All the flanges, dips, recesses and spaces, as well as all the materials shown in the figure, were included in the simulations. Not shown in this figure is the extra shielding (WNiCu) that will be added to the recesses of Stations 1 and 2 after installation.

In the TDR the carbon in the front absorber had a density of 1.9 g.cm^{-3}. This density was not easy to obtain from industry so the standard one of 1.75 g.cm^{-3} was eventually chosen. To compensate for the difference, iron and copper were added at the end of the front absorber.

The simulation showed that we could replace a part of the tungsten in the second half of the beam shield. To compensate for this a cone of 1.6° of lead had to be added at the level of the big stations. This new set-up does not increase the background, nor change the acceptance, but allows some substantial savings.

The philosophy for having a safety factor has not changed: the central multiplicity is the highest which is foreseen (HIJING: $dN_{charged}/dy \approx 6000$ in the central region) and then it is multiplied by a safety factor of 2. All results presented here include this safety factor. In Table 6.1 we show the total number of hits and the maximum hit density for each of the stations. The indicated ranges show the differences between GEANT and FLUKA simulations. FLUKA results lie at the lower and GEANT results at the higher bound. These results are consistent with those obtained from a combination of GEANT3 for neutron energies down to 20 MeV and C95 for the low energy part (Table 6.2). The C95 simulation shows also the importance of the inclusion of the low energy neutron part in the transport. It contributes up to 30% to the total hit rate.

With respect to the TDR (FLUKA results only), the background increased by about 25% in the first two stations because of the inclusion of the heating jacket insulation and protection of the beam pipe, but also because of the more realistic layout of the recesses for Stations 1 and 2. However, in the third station the background conditions stay constant and in Stations 4 and 5 they decrease due to the extra outer lead shield that over-compensates for the replacement of the inner tungsten shield by lead.
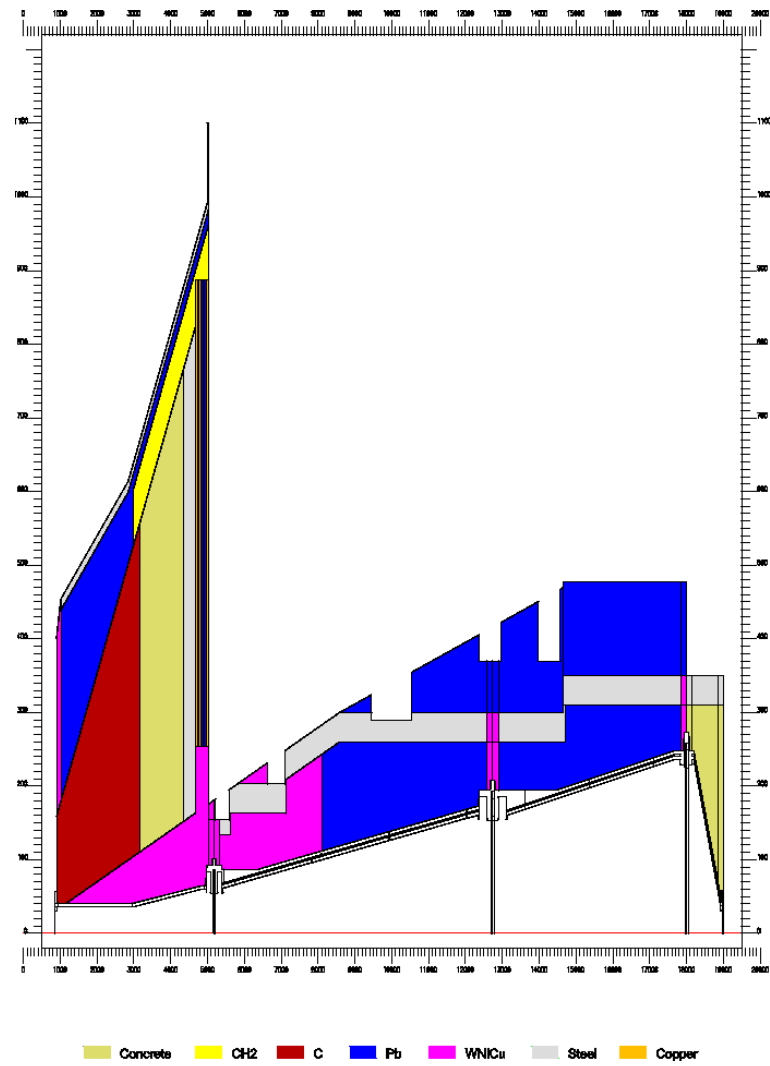
Figure 6.1: Side view of the front absorber and the beam shield.

Table 6.1: Background rate for each station with a safety factor of 2 included. The FLUKA results are at the lower and the GEANT results at the higher bound of the shown ranges. Results are compared to the FLUKA results presented in the TDR.

Station	Total hits	Max. density (10^{-2} part/cm^2)	Total hits (TDR)	Max. density (TDR) (10^{-2} part/cm^2)
1	400 ± 40	5.0	320	4.0
2	505 ± 55	2.1 ± 0.1	340	1.6
3	250 ± 20	0.7	230	0.6
4	225 ± 45	0.5 ± 0.05	380	1.0
5	265 ± 35	0.6 ± 0.05	620	1.2
6 (trigger)	40 ± 5	0.15 ± 0.3	40	0.12
7 (trigger)	50 ± 10	0.17 ± 0.2	54	0.16

Table 6.2: Background rate for each station with a safety factor of 2 included. Results have been obtained by a GEANT+C95 simulation. The contribution from neutron interactions (E_{kin}< 20 MeV) are shown separately (low-n).

Station	Total hits	Charged	Gamma	Neutrons	Low-n	Max density (10^{-2} part/cm^2)
1	480	460	20	2	14	5.2
2	500	480	22	3	24	3.1
3	310	280	29	9	61	0.56
4	340	260	60	22	100	0.56
5	380	300	56	18	100	0.40
6	45	44	3	0.06	3	0.16
7	65	62	3	0.02	2	0.14

The observed influence of the beam-pipe material distribution on the hit rate in Stations 1 and 2 suggests that misalignment of the beam pipe with respect to the front absorber or the beam with respect to the beam pipe could have a similar effect. It was verified that both misalignments increase the background rate by less than 10%.

The hit densities as a function of the radius as obtained by GEANT are shown in Fig. 6.2. For the convenience of being produced within the same simulation framework (AliRoot), we use these distributions as the input for the occupancy, hit and track reconstruction studies.

6.3 Physics results

The results presented in this chapter have been obtained using AliRoot, the ALICE object-oriented framework for simulation, reconstruction and analysis based on ROOT. Particle transport is performed by GEANT 3.21. The simulation of the muon spectrometer is as close as possible to the reality as described in the previous chapters. In particular, it contains a detailed description of the structural elements (front absorber, beam pipe and shield, dipole magnet), the exact material distribution in Stations 4-5 and a realistic segmentation layout of all the chambers. The material distributions of Stations 1 and 2 have been approximated by their averages over the chamber plane. Detector response simulation was performed using the Mathieson charge distribution as described in the TDR.

In addition to the changes described in this document, two, which are directly connected to the sim-
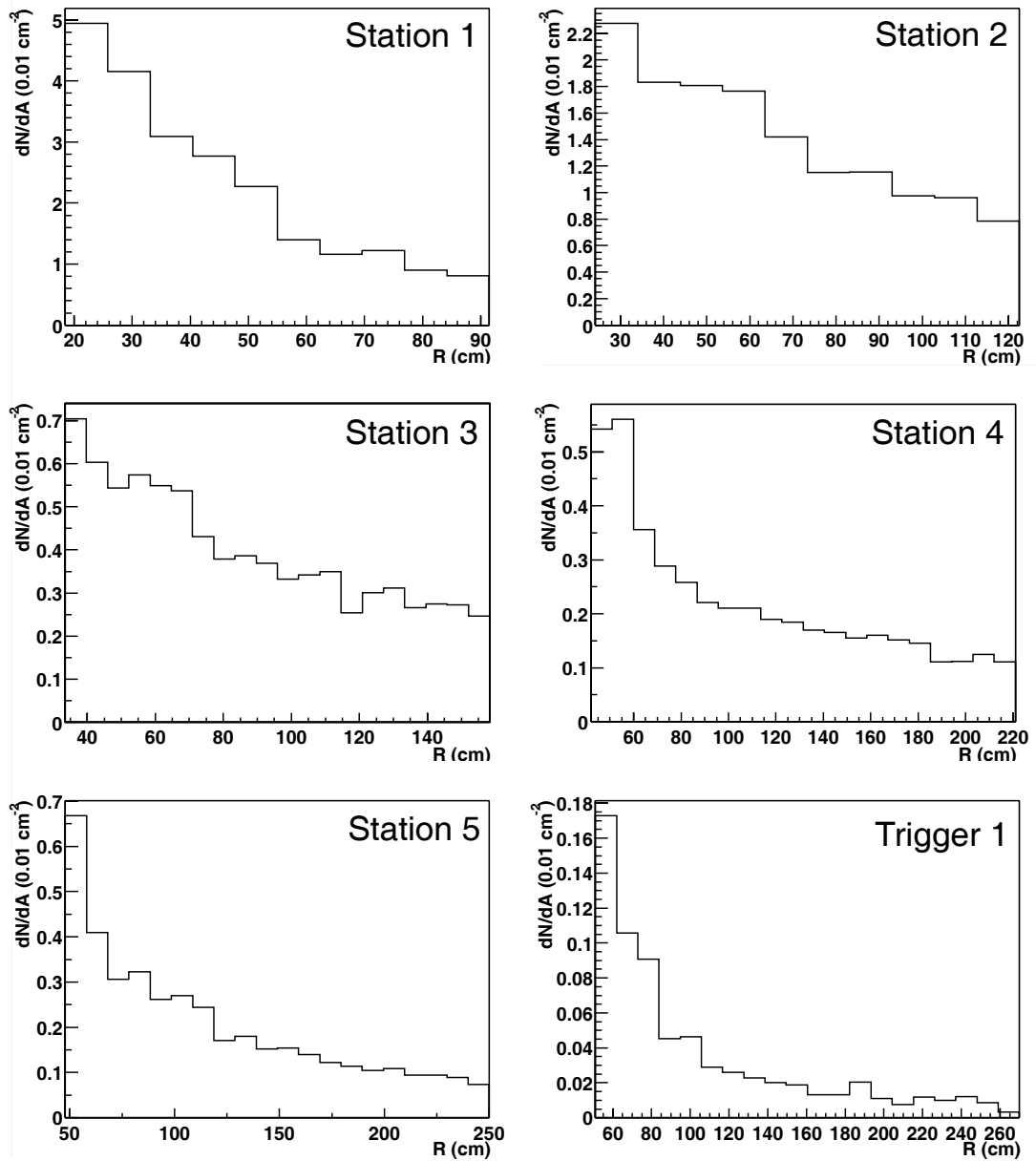
Figure 6.2: Hit density as a function of the radius for each tracking station and for the first trigger station.

ulation procedure, need to be mentioned. First, the distance between the absorber and the first tracking chamber has been increased. Radiative losses of the muons in the front absorber (bremsstrahlung and direct pair production) produce in the first chamber hits from electrons close to the muon hit. With a larger distance, muon hits of interest are better separated from electron hits, which is helpful for track reconstruction. This effect will be further quantified in the future together with an ongoing optimization of the material used for absorber layers close to the first chambers. Secondly, the cluster finding algorithm has been changed to a search for clusters in both cathode planes in parallel, which are fitted simultaneously with Mathieson distributions. This procedure leads to a better efficiency for finding the clusters, an improved multi-cluster deconvolution and a better resolution on their positions in two dimensions.

Simulations have been performed on the basis of 1000 Υ resonances, mixed with one or more among ten 'nominal' background events. As for the TDR, a nominal background event contains the uncorrelated background hits resulting from two central Pb–Pb collisions simulated with HIJING. The Υ resonances have been generated using a parametrization of the transverse momentum distribution measured by CDF.

6.3.1 Efficiency

The results for the efficiencies for Υ an muons from its decay produced in the rapidity range $2.5 < y < 4$ and for the mass resolutions under various simulation and background conditions are presented in Table 6.3. The efficiencies ε_{all} and ε are defined for reconstructing the Υ resonance without any limit on the mass and between 9.17 and 9.77 GeV ($\pm$ 300 MeV around the Υ mass), respectively.

Geometrical acceptance The geometrical acceptance is limited by the inner and outer borders of the sensitive chamber regions and by the vertical dead zone in the middle of Stations 3 to 5. For the new layout it amounts to 95%, which represents a significant improvement with respect to the TDR result (88%).

Chamber efficiency and resolution We assume a chamber efficiency of 95%. For the majority cut used for the reconstruction (1/2 for each station in front of and inside the dipole magnet and 3/4 behind the magnet) this results in a limiting tracking efficiency of 96%. The limited chamber resolution ($100\,\mu$m in the bending plane and 1.44 mm in the non-bending plane) has a much smaller influence and the combined efficiency of the two amounts to 95%.

Intrinsic tracking efficiency The intrinsic tracking efficiency of our present tracking algorithms can be obtained from an event reconstruction using GEANT hits, i.e. not smeared impact points without hit reconstruction (Table 6.3, first two rows). This efficiency lies in the range 93% to 96% depending on the width of the roads used for the track finding. The third row of Table 6.3 shows the cumulative result of chamber and limiting tracking efficiency (84%).

The corresponding value obtained with reconstructed hits is higher than this limit (88%), which indicates that we might overestimate the chamber efficiency in the response simulation. On the other hand, very loose cuts have been chosen during track finding, so that the effective chamber efficiency is higher than the value of 95% used above.

Inefficiency due to tails in the mass distribution Energy losses of muons due to radiative interactions render the dimuon mass distribution asymmetric (Figs. 6.3 and 6.4). Since the resonance peak has to be detected on top of a sizeable continuum background, the events in the tails are lost. Assuming a signal region between 9.17 and 9.77 GeV (approximately $\pm 3\sigma$) results in a 7% inefficiency due to this effect.

GH/RC	Bkg	ε	σ (MeV)	M (GeV)	χ^2/dof	ε_{all}
GH*	no	.819	84.6(3.0)	9.4760(36)	2.6	.882
GH* wider cuts	no	.843	84.5(3.0)	9.4770(35)	2.5	.908
GH	no	.782	90.8(3.3)	9.4790(38)	0.6	.840
GH	yes	.772	93.3(3.7)	9.4790(40)	1.8	
RC	no	.811	94.0(3.6)	9.4760(41)	1.8	.882
RC	yes	.750	110.9(5.4)	9.4760(62)	2.1	
RC	$\times$ 0.5	.786	101.6(4.0)	9.4690(50)	1.6	
RC	$\times$ 2	.614	136.8(8.6)	9.4760(89)	1.0	

Table 6.3: Efficiencies for reconstructing the Υ resonance without any mass limit (ε_{all}) and in the interval between 9.17 and 9.77 GeV (ε), for reconstruction from Geant hits (GH) or raw clusters (RC), with or without the nominal background (Bkg). Also shown are χ^2/dof, mean value M and standard deviation σ of the Gaussian fit to the reconstructed mass distribution between 9.3 and 9.8 GeV.

Multi-hit deconvolution   The total efficiency taking into account the contributions mentioned above amounts to 78%. This efficiency is further decreased in a realistic multi-hit environment. As can be seen from Table 6.3, the effect is mainly due to the inefficiency in deconvoluting multi-hits (row 6) and less due to confusions in the track finding, assuming ideally resolved hits (impact points, row 4). This inefficiency increases with the chamber occupancy. It amounts to 7.5% (3.1%, 24%) for 1 (0.5, 2) nominal background events.

The efficiency as a function of the background level is shown in Fig. 6.5.

6.3.2   Mass resolution

The mass resolution σ obtained from simulation is the result of the Gaussian fit to the reconstructed mass distribution between 9.30 and 9.85 GeV.

The intrinsic mass resolution of the spectrometer at the Υ mass given by multiple scattering (front absorber and chambers), (Gaussian) energy straggling and the spatial resolution of the chambers amounts to 80 MeV. Energy losses (see above) result in an asymmetric mass distribution (tail towards lower masses), leading to an effective broadening of the mass peak. The width obtained from a full simulation and applying a fit of a Gaussian to the central mass region amounts to 90 MeV.

The inclusion of background and the resulting multi-hits deteriorate the mass resolution. The resolution as a function of the background level is shown in Fig. 6.6. For one nominal background event the resolution amounts to 110 MeV.

Finally, the mass spectrum obtained with track reconstruction from raw clusters and with the nominal background can be looked at in a different way (Fig. 6.7). To take into account the tail at low mass due to radiative effects in the absorber, it has been fitted with a sum of two Gaussian distributions between 8.9 and 10 GeV. The quality of the fit is good, with a χ^2/ dof of 18.5/17 . The main component is peaked at 9.483 (8) GeV, with a standard deviation of 94.5 (8.7) MeV. The tail component is peaked at 9.341 (40) GeV, with a standard deviation of 231 (29) MeV. With such a mass response function, one should be able to unfold the contributions from the Υ' and Υ'' resonances. Compared to the TDR, this represents important progress since, with more realistic background simulations, the hit densities have increased, and since the geometrical acceptance has been increased in the regions close to the beam pipe, where tracks are most difficult to find and reconstruct accurately. It must also be emphasized that the total efficiency does not vary by a large amount between zero background and the nominal background, which will be helpful for the studies of resonance production as a function of the centrality for Pb–Pb collisions.
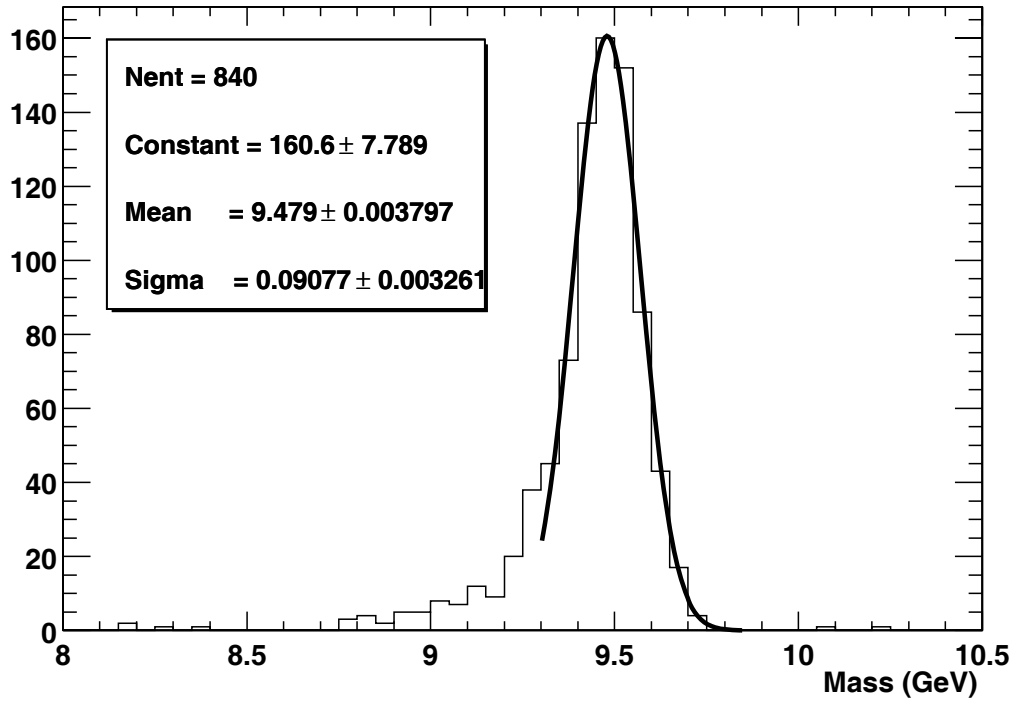
Figure 6.3: Mass spectrum for Υ resonances reconstructed from GEANT hits without background, with a smearing of 100 μm in y and 1.44 mm in x, and with a chamber efficiency of 95%.
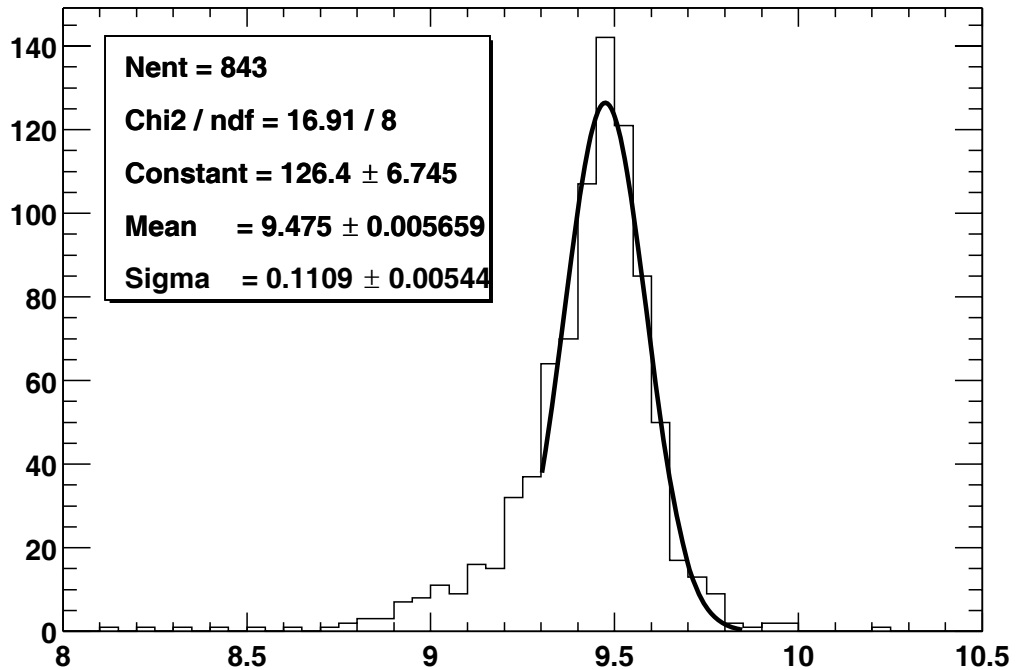
Figure 6.4: Mass spectrum for Υ resonances reconstructed from raw clusters with nominal background.
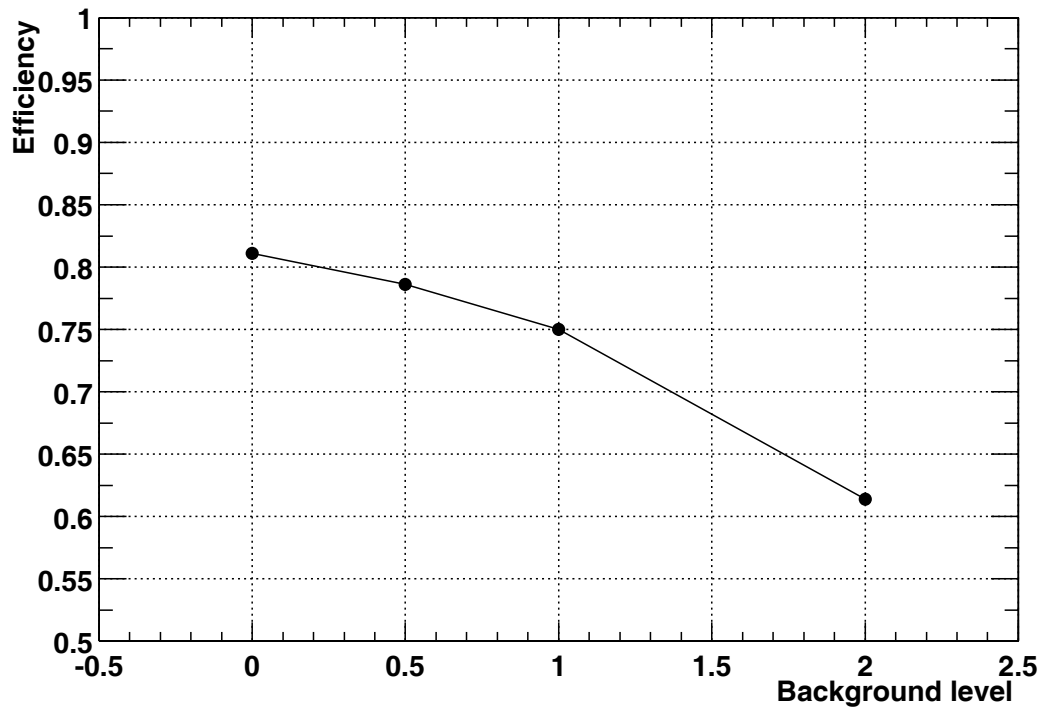
Figure 6.5: Total efficiency ε (see text for the exact definition) for reconstructing the Υ resonance from raw clusters versus the background level with respect to the nominal background.
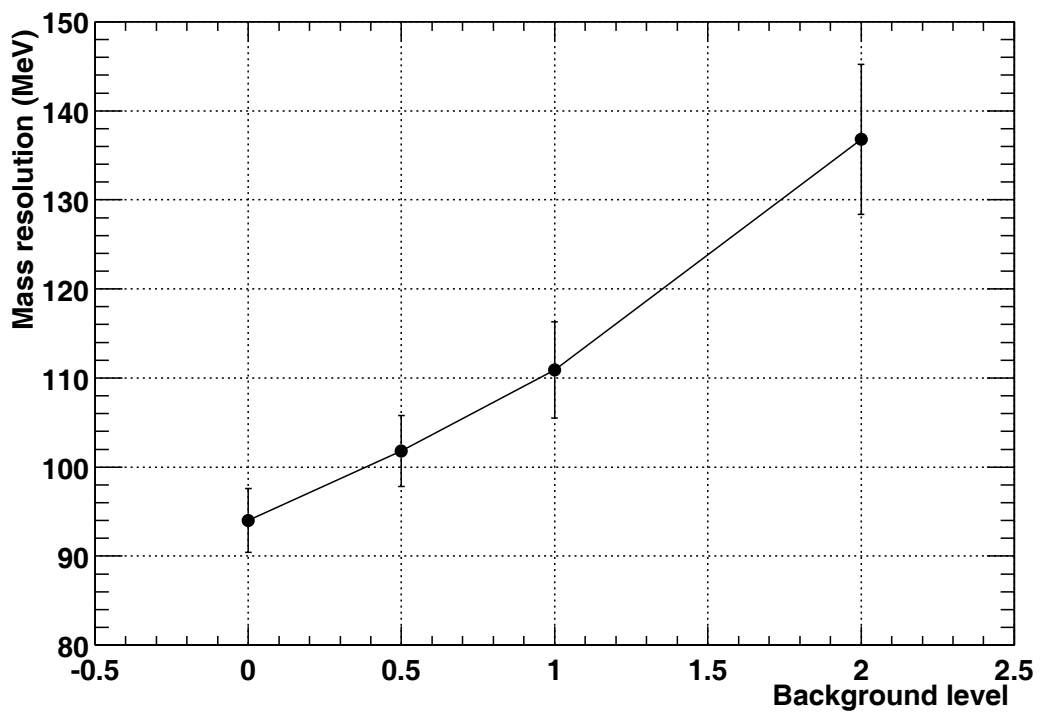
Figure 6.6: Mass resolution, from of Gaussian fit to the mass distribution between 9.30 and 9.85 GeV, for the Υ resonances reconstructed from raw clusters, versus the background level with respect to the nominal background.

Figure 6.7: Mass spectrum for Υ resonances reconstructed from raw clusters with nominal background, fitted with a sum of two Gaussian distributions.

7 Implementation and infrastructure

7.1 Introduction

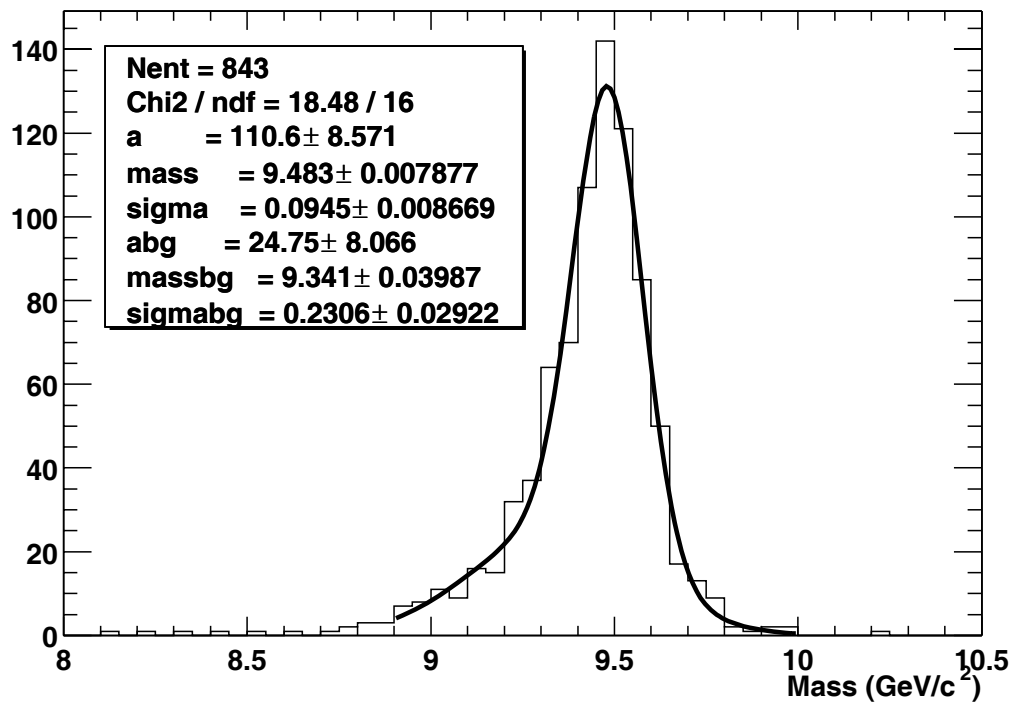The ALICE detector will be installed at Point 2 of the LHC accelerator. The experimental area and infrastructure installations for the muon spectrometer have already been described in the Technical Design Report (TDR) [1], which remains valid without any changes or additions. This chapter will, therefore, concentrate on the progress made in defining the general installation scenario for the various components of the muon spectrometer. Whenever possible references will be made to subsystem design reports.

7.2 Integration and assembly of the muon spectrometer

7.2.1 Overall layout

The muon spectrometer is placed on the RB26 side of the Point 2 intersection, limited by the L3 magnet and the concrete wall of the experimental area, which is situated 19.0 m from the intersection point. Figure 7.1 shows the general layout of the muon spectrometer.

The dipole magnet and the muon filter are placed on solid concrete support structures. Contrary to the situation in Ref. [1], the muon magnet is installed in a fixed position and can not be moved. The front absorber is supported by a dedicated mechanical structure fixed to the L3 magnet. This structure also houses and supports the first two tracking stations, while tracking station 3 is supported from the muon magnet. The first part of the small-angle absorber (beam shield) is supported by a system of cables fixed to the dipole magnet. The remaining part of the small angle absorber is supported by the muon filter and the cavern wall. Tracking stations 4 and 5 and the trigger stations are all supported by a common super-structure, integrated with the muon filter.

Once the muon spectrometer is installed, it will no longer be possible to open the L3 magnet doors (on the muon-arm side). Additional services must, therefore, be installed with the magnet door fully closed. It will still be possible to make such installations, although they will be very time consuming and the bulk of the service installations must be installed before the doors are condemned in a closed position.

The geometric layout of all the components is defined in a parameter drawing (see Fig. 7.2). This assures the compatibility between the different sub-elements and guarantees that the muon spectrometer is consistent with the central part of the ALICE detector and general infrastructure installations.

7.2.2 Pre-assembly phase

The overall ALICE work schedule foresees a pre-assembly phase for the complete muon spectrometer to take place in the SXL2 assembly hall prior to the installation in the underground area. The dipole magnet will be fully assembled together with the absorber, the muon filter and chamber hardware, as indicated in Fig. 7.3. This will allow an early preparation of the various detector services and permit the installation and access scenarios to be analysed and corrected before lowering the spectrometer into the experimental cavern.

The pre-assembly is particularly important for the muon magnet. At present we assume that temporary power cables can be routed from the power supply in the SX2 building to the muon magnet in the SXL2 building, so that a test at full power can be made.

The assembly and testing of the absorber system will be made in the SXL2 hall. A full description of this process can be found in Ref. [2].
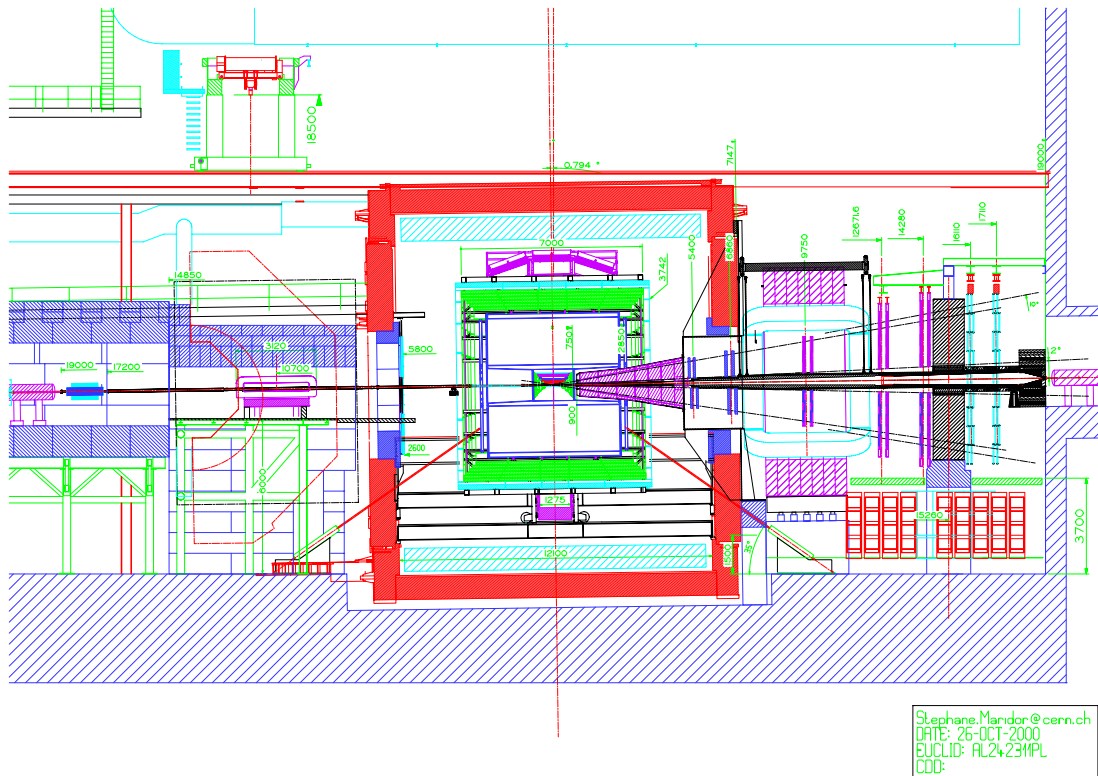
Figure 7.1: General layout view of the muon spectrometer.
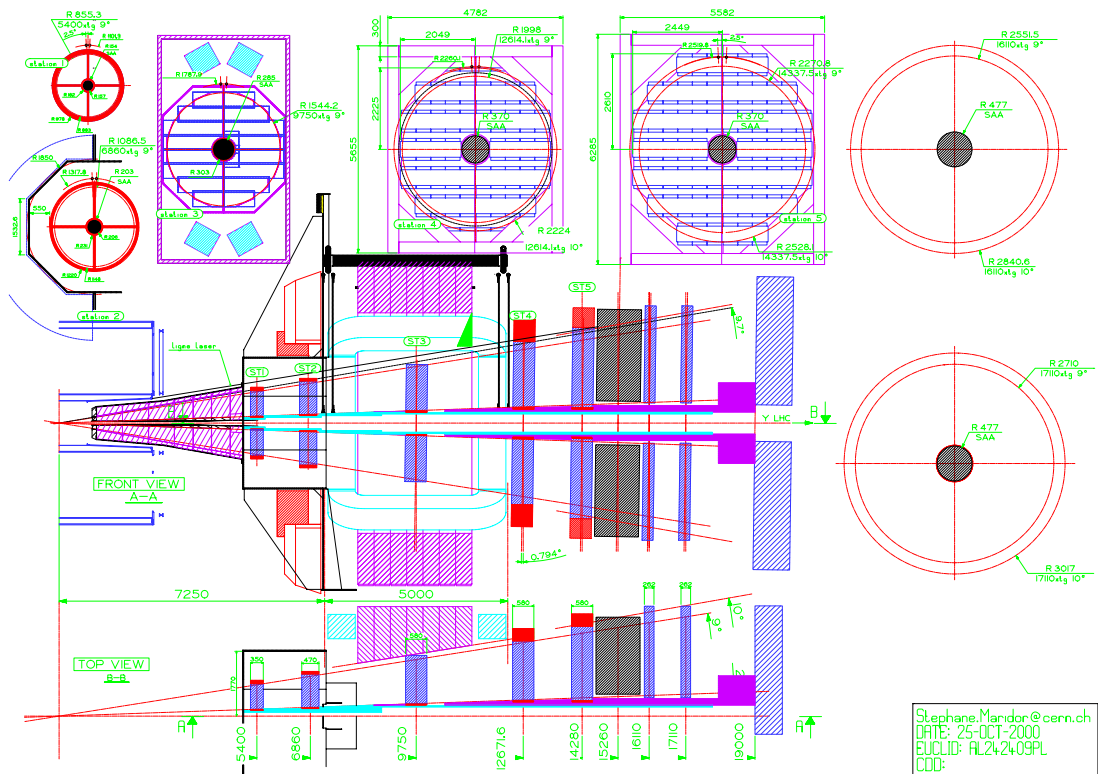
Figure 7.2: Parameter drawing for the muon spectrometer
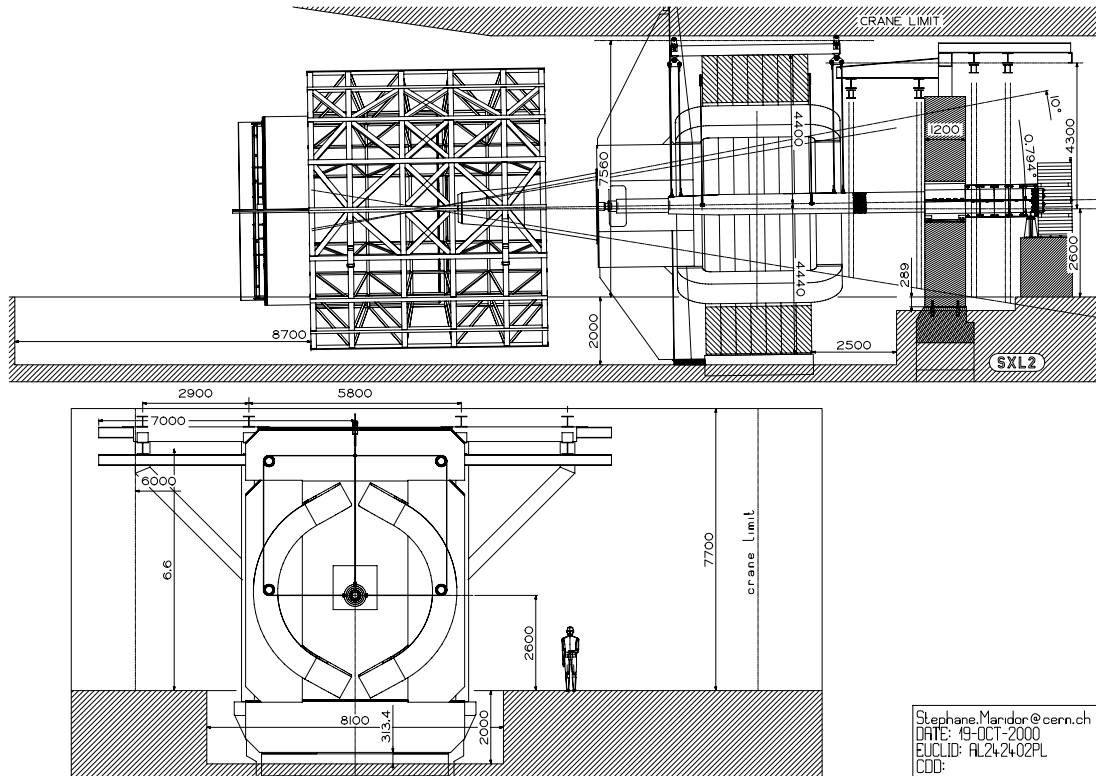
Figure 7.3: Pre-assembly of the muon spectrometer in the SXL2 hall at Point 2, together with the space-frame.

The muon filter will be constructed from iron slabs held together by arrow shaped 'catchers' as indicated in Fig. 7.4. Special care has been taken to allow a rapid removal of the top part of the muon filter, in order to access the absorber / vacuum chamber system. Figure 7.5 shows the assembly principle and the function of the catchers. The stability of the muon filter has been reinforced compared to the design presented in Ref. [1] and it now serves as a support structure for the small-angle absorber and as a base structure for the superstructure for tracking stations 4 and 5 and the trigger chambers.

7.2.3   Installation in the underground cavern

The layout of the Point 2 cavern access shaft is asymmetric, which implies that all large or heavy objects installed on the RB26 side of the L3 magnet, must be transported through or over the L3 magnet. This constraint is the basis for the overall installation schedule of the ALICE detector. Furthermore it is necessary to perform a complete field mapping of the combined L3 plus dipole magnet system. These measurements cannot be performed with any of the sub-detectors *in situ*. The installation of the muon magnet blocks the opening of the L3 doors; it is, therefore, imperative that the support for the front absorber and as many of the service installations as possible are installed before the muon magnet is erected.

 The installation procedure can be divided into the following main phases:

1. installation of the front absorber,

2. installation of the muon magnet and field measurements,

3. installation of the small angle absorber and muon filter base structure,

4. installation of the tracking and trigger chambers.

Figure 7.4: Overall design of the muon filter.

Figure 7.5: Assembly of the muon filter.
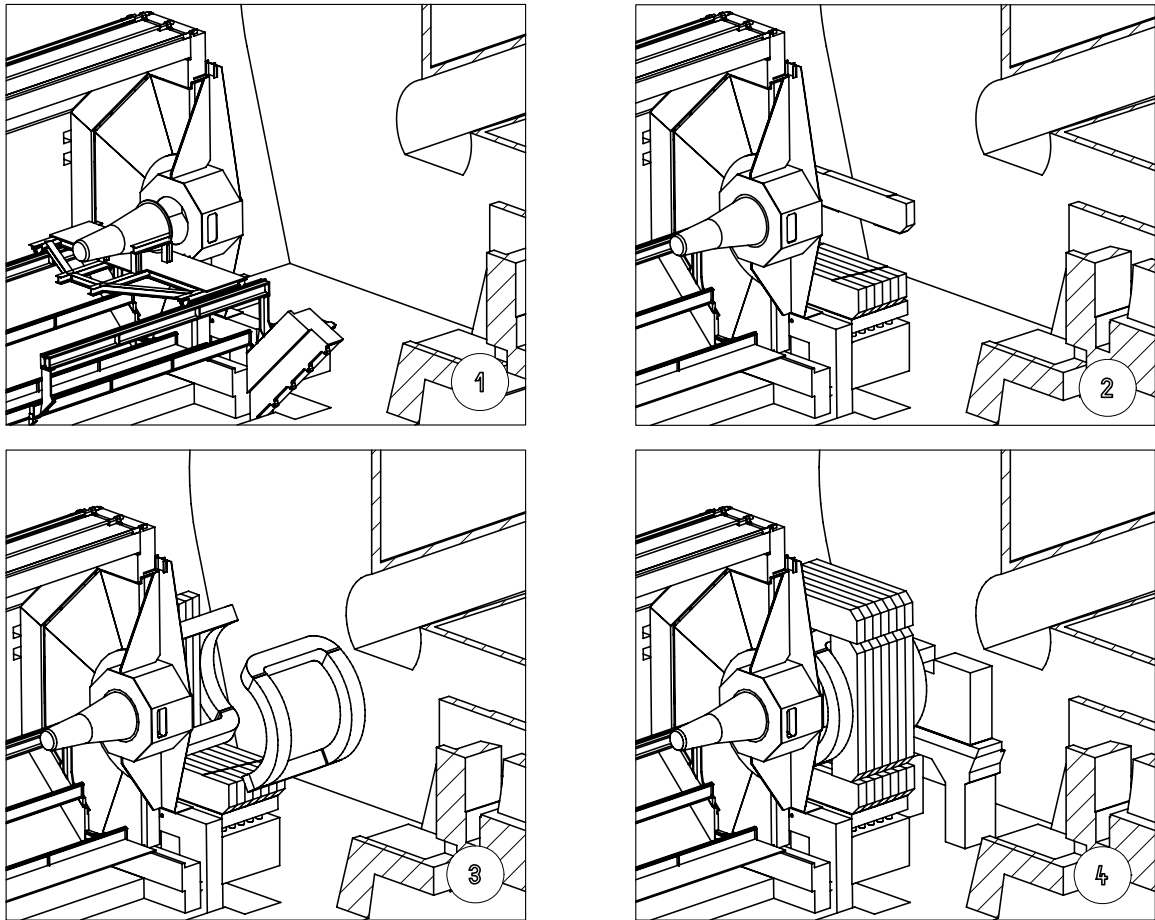
Figure 7.6: Main phases of the front absorber and dipole magnet installation.

7.2.3.1   Installation of the front absorber

The front absorber (about 30 t) will be supported by a vertical mechanical structure attached to the iron yoke of the L3 magnet. The conical part of the absorber will be installed through the L3 magnet with the help of a 'table' rolling on the rail system installed for the central detectors (see Fig. 7.6, phase 1).

7.2.3.2   Installation of the muon magnet

The 800 t of the dipole magnet will be assembled from parts having a maximum weight of about 35 t. Each part has to pass in the free space above the L3 magnet. Phases 2-4 of Fig. 7.6 show the principal steps of the installation sequence. After assembly, the magnet will be powered and magnetic measurements and field mapping will be carried out along with the L3 magnet.

7.2.3.3   Installation of small-angle absorber / vacuum chamber / muon filter

Once the muon magnet is installed the lower part of the muon filter can be constructed. The muon filter will serve as a basis for the installation of the small-angle absorber (see Fig. 7.7). The first absorber section will be rolled inside the muon magnet using a temporary assembly platform and attached to the muon magnet via vertical wires. The second section of the small-angle absorber can be installed directly onto the lower part of the muon filter.

The initial assembly of the absorber does not cover the vacuum-chamber flanges, which permits access for assembly and testing of the vacuum-chamber system. Once the flanges have been leak-tested
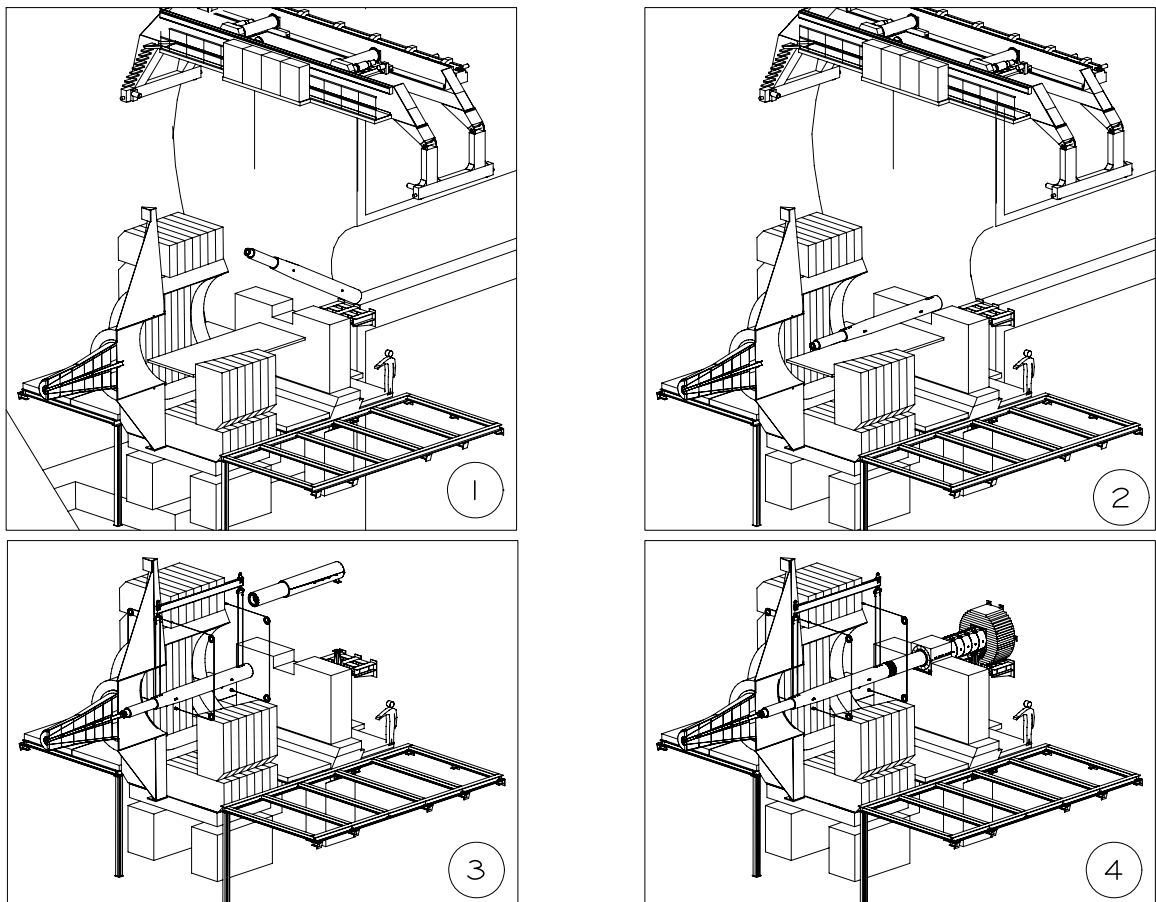
Figure 7.7: Main phases of the installation of the muon filter and small angle absorber sections.
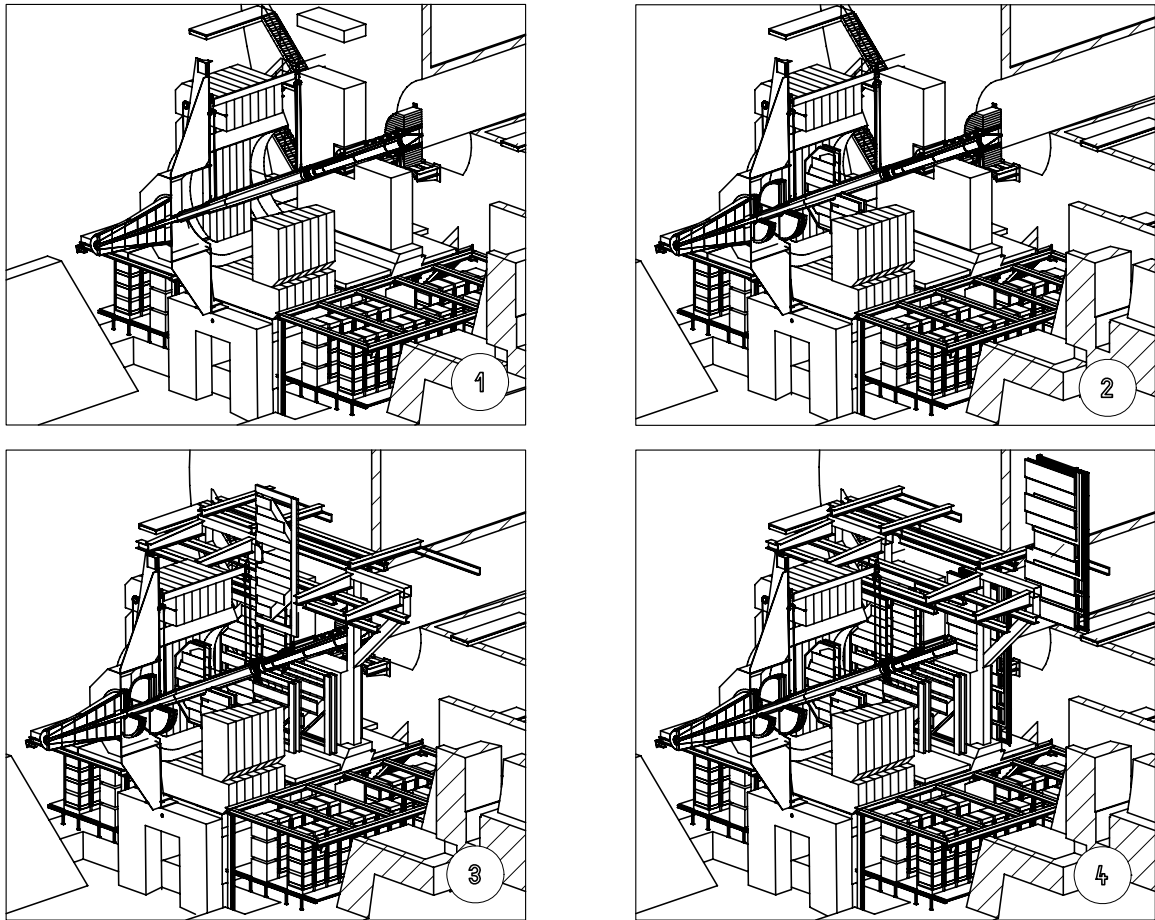
Figure 7.8: The principal phases of the installation of the tracking / trigger chambers

a special joint section is put in place. This will also allow relatively convenient and fast access to the vacuum flanges.

7.2.3.4 Installation of the tracking and trigger chambers

Stations 1, 2 and 3 will be installed through the 'back' aperture of the dipole magnet. This requires the displacement of Station 4 perpendicular to the beam line.

Stations 4 and 5 and the trigger chambers will be suspended from the muon filter support structure on a rail system, which will allow them to be displaced perpendicular to the beam direction. The principal phases of the chamber installation are described in Fig. 7.8.

7.3 Access for maintenance and repair

Access for maintenance to the various parts of the muon spectrometer is relatively straightforward. The dipole magnet, Stations 4 and 5 and the trigger stations are directly accessible from the concrete platform. Stations 1, 2 and 3 can be accessed via a staircase situated between the muon magnet and the L3 magnet, as indicated in Fig. 7.9. An opening in the support for the front absorber will also allow access from the L3 magnet to Stations 1, 2 and 3. Therefore two independent accesses to the closed volume surrounding Station 1, 2 and 3 are provided. Figure 7.10 shows the available access at the side of Station 1. Removing Station 1, 2 or 3 would require the displacement of Station 4.

Figure 7.9: Access to Stations 1, 2 and 3.

Figure 7.10: Access to Stations 1 and 2.

Figure 7.11: Layout showing the vacuum chamber integrated with the absorber.

7.4 Vacuum system

The ALICE vacuum chamber has been extensively described in Ref. [3]. The principal difficulty is to integrate the vacuum chamber and associated equipment (bake-out jackets, instrumentation) into the small-angle absorber. The major difficulty has been to provide access to the vacuum flanges. Figure 7.11 shows the overall integration of the vacuum chamber together with the detailed design of the vacuum flange sections.

The complete length of the cone-shaped vacuum chamber inside the absorber (18,060 mm) will be equipped with NEG pumps and permanent heating and thermal insulation equipment. The wall thickness of the beam pipe has been determined solely from the calculation of the mechanical stability including the additional weight of bake-out equipment, with no major considerations of material optimization. The wall thickness in the cone will vary from 1.5 to 4 mm.

The beam pipe will have to be heated up for vacuum conditioning and getter re-activation reasons. The heating jackets will consist of a thin heating tape, about 0.5 mm. Thermal insulation is provided by a layer of 5 mm thick zirconium. This will result in a heat load to surrounding elements of around 1300 W/m^2 when heated to 300 $^{\circ}$C.

7.5 Assembly and installation schedule

The overall ALICE work schedule foresees a pre-assembly phase of the muon spectrometer, which will take place in the assembly hall SXL2 at Point 2 starting with the dipole magnet assembly in April 2003. This will allow an early preparation of the different support structures and services, and permit the installation procedure to be analysed and corrected before integrating the detectors into the experimental area. Table **??** gives the milestones for the various sub-assemblies of the muon spectrometer.

References

Chapter 1

[1] ALICE Collaboration, Dimuon forward spectrometer: technical design report, CERN/LHCC 99–22 (1999).

Chapter 2

[1] ALICE Collaboration, Dimuon forward spectrometer: technical design report, CERN/LHCC 99–22 (1999).

[2] J. Peyré and E. Rindel, Mechanical study of 1st and 2nd tracking chamber stations of the ALICE dimuon spectrometer. IPN Orsay, Internal Report.

Chapter 3

[1] ALICE Collaboration, Dimuon forward spectrometer: technical design report, CERN/LHCC 99–22 (1999).

[2] R. Arnaldi et al., Nucl. Instrum. Methods **A451** (2000) 462.

[3] I. Crotty et al., Nucl. Instrum. Methods **A360** (1995) 512.

[4] R. Arnaldi et al., Nucl. Instrum. Methods **A**, in press.

[5] L. Royer et al., Proc. 6th Workshop on Electronics for LHC Experiments - LEB 2000, CERN/LHCC 2000–041 (2000).

[6] B. Cheynis et al., For a V0 detector dedicated to the pp$\rightarrow$2μ+X physics in ALICE, Internal note ALICE/00–30, 13 September 2000.

[7] ALICE technical proposal, CERN/LHCC 95–71 (1995).

[8] V.A. Grigoriev et al., ALICE T0 start detector based on Cherenkov radiators and fine-mesh photo-tubes, Internal note ALICE/99–43, 20 September 1999.

[9] F. Ariztizabal et al., Construction and performance of an iron-scintillator hadron calorimeter with longitudinal tile configuration, Nucl. Instrum. Methods **A349** (1994) 384.

[10] S. Filippov et al., Experimental performance of SPD/PS detector prototypes, Internal note LHCb 2000–31 CALO, 24 June 2000.

[11] M.M. Aggarwal et al. Nucl. Instr. Meth. in Phys. Res A372(1996) 143.

[12] M.M. Aggarwal et al. Nucl. Instr. Meth. in Phys. Res A421(1999)558.

Chapter 4

[1] ALICE Collaboration, Dimuon forward spectrometer: technical design report, CERN/LHCC 99–22 (1999).

[2] The forward muon spectrometer, CERN/LHCC 96-32, LHCC/P3-Addendum 1, 15 October 1996.

[3] ALICE experiment, CERN/LHCC 95-71, LHCC/P3, 15 December 1995.

[4] A.A. Grigoryan and A. Teymurazyan, Light ray displacements due to air temperature gradient, ALICE/2000-13 Internal Note/DIM, May 12, 2000.

[5] V.D. Danielyan, V.H. Kakoyan, V.H. Mamyan, Yu.L. Margaryan, Reflected Light Monitor For Multi-point Position measurements, ALICE/99-27 Internal Note/DIM, May 28, 1999.

Chapter 5

[1] ALICE Collaboration, Dimuon forward spectrometer: technical design report, CERN/LHCC 99–22 (1999).

[2] Manufacturing design contract K640/EP, November 1999.

[3] ALICE dipole magnet PRR, 17/18 July 2000.

[4] Engeneering Design and Manufacturing Specifications for the Dipole Magnet of the ALICE Muon Spectrometer, ALICE.05100.006.00TZ, JINR Dubna, August 2000.

[5] Invitation to tender for the resistive coils of the LHCb dipole magnet, IT–2739/EP/LHCb.

[6] Thermo cycle tests of the ALICE dipole magnet prototype, Dubna 2000.

[7] Mechanical tests of winding prototypes of the ALICE dipole magnet, Dubna 2000.

[8] Results of model pancake prototype II manufacturing and tests, 2254.00.000.R1, JINR, 14 June 2000.

[9] Bending tests of conductors for ALICE and LHCb dipole magnets, INT–00–08 ALICE/LHCb, April 2000.

Chapter 6

[1] ALICE Collaboration, Dimuon forward spectrometer: technical design report, CERN/LHCC 99–22 (1999).

Chapter 7

[1] ALICE Collaboration, Dimuon forward spectrometer: technical design report, CERN/LHCC 99–22 (1999).

[2] V.F. Basmanov et al., Development of an Open-Geometry Muon Absorber for the ALICE Experiment, Internal Note ALICE/99-38, November 1999.

[3] I.R. Collins et al., The ALICE Beam Vacuum System, Internal Note ALICE/ 99-35.